EXPERIMENTAL STUDY OF THE EFFECT OF PERMEABILITY ON THE GENERATION OF NOISE

A Thesis

by

RODOLFO ALFONSO SANTOS

Submitted to the Office of Graduate and Professional Studies of
Texas A&M University
in partial fulfillment of the requirements for the degree of

MASTER OF SCIENCE

Chair of Committee,	Alfred Daniel Hill
Co-Chair of Committee,	Scott Miller
Committee Member,	Ding Zhu
Head of Department,	Jeff Spath

December 2018

Major Subject: Petroleum Engineering

ABSTRACT

Recent developments in fiber sensing systems have led to their application in the field of petroleum engineering, particularly production monitoring, and stimulation operation diagnosis. The spatially distributed and temporally continuous monitoring which fiber optic sensing technologies offers allows for a wealth of information to be ascertained including acoustic, strain, temperature, and microseismic data. However, there are challenges, in particular data handling, interpretation, and data quality assurance have been issues facing the wide spread adoption and implementation of fiber optic sensing technologies.

Many fiber optic service companies have developed analysis, and interpretation methods for fracture fluid distribution during stimulation operations, as well as production allocation methods while other companies have struggled with interpretation of flow through various subsurface structures and fixtures used during stimulation operations. Understanding of the effects of porous media on the generated acoustic signal is paramount to the development of interpretation and analysis methods for production monitoring, and stimulation diagnosis.

The purpose of this work was to build upon previous studies done on flow through a parallel plate fracture cell into a simulated wellbore. In particular, the work performed was to investigate the effect which proppant pack permeability has on the generated acoustic signal through the simulated fracture and further refine the empirical correlation put forth by Chen (2015). Results from this study showed that there is a dependence on

the permeability of the proppant pack. The A correction value in the correlation put forth by Chen increases as the proppant pack permeability decreases, and isn't influenced by the Reynolds number pointing to a dependence on the pore structure of the proppant pack.

CONTRIBUTORS AND FUNDING SOURCES

Contributors

This work was supported by a thesis committee consisting of Professor Alfred Daniel Hill and Professor Ding Zhu of the Department of Petroleum Engineering and Professor Scott Miller of the Department of Electrical Engineering.

All work conducted for the thesis was completed by the student independently.

Funding

Graduate study was supported by a fellowship from Texas A&M University and a thesis research fellowship from the Crisman Institute for Petroleum Research.

TABLE OF CONTENTS

LIST OF FIGURES

LIST OF TABLES

1. INTRODUCTION

1.1 Acoustics

Sound is a molecular oscillation of a media that can be characterized by a pressure amplitude which is time variant, (Kinsler 2000). A simple sinusoidal oscillation of pressure within the media can be characterized by a frequency (f), expressed in Hertz (Hz) which is the number of cycles the sinusoidal oscillating waves goes through per second. As time propagates the pressure perturbance radiates from the source of the molecular oscillation at the speed of sound (C) of the media. C, in the case of non-dispersive, media is not dependent on the frequency of the oscillations. More complex wave forms such as square waves or multiple superimposed sinusoids can be decomposed into a series of simple sinusoid using Fourier analysis by

$$g(\omega) = \frac{1}{2\pi}\int_{-\infty}^{\infty} f(t)e^{-j\omega t}dt$$

for a continuous signal in the time domain. This function will transform a continuous function in the time domain into a function of angular frequency in the frequency domain. In practice, Fourier transforms done in finite element analysis software, like MATLAB, are done using a recursive algorithm which takes small sections of the input pressure data and generates a two-sided spectrum which must then be reconciled into a single sided spectrum of only positive-real values (Strang 2007).

Sound pressure level (SPL) is the measure of the logarithm of the ratio of an acoustic pressure against a reference pressure typically taken to be $2x10^{-5}$ Pa which is the threshold of sensitivity of human hearing at 1000 Hz.

1.2 Acoustic Logging

Use of noise logging for leak detection and production logging was made commercially viable by the work done by McKinley et al. (1973). The work measured acoustic events at different depths within a well to give fluid movement within the wellbore, across channels, and through orifices. The work relates peak to peak amplitudes of various frequencies as a function of pressure drops and volumetric flows within a leak simulator. The dissipation of energy within the fluid in these pressure drops and throttling of the fluid across various subsurface structures is believed to be released as an acoustic event.

Spectra of the measured acoustic signal of flow across an orifice is shown in the study in Figure 1, and Figure 2.

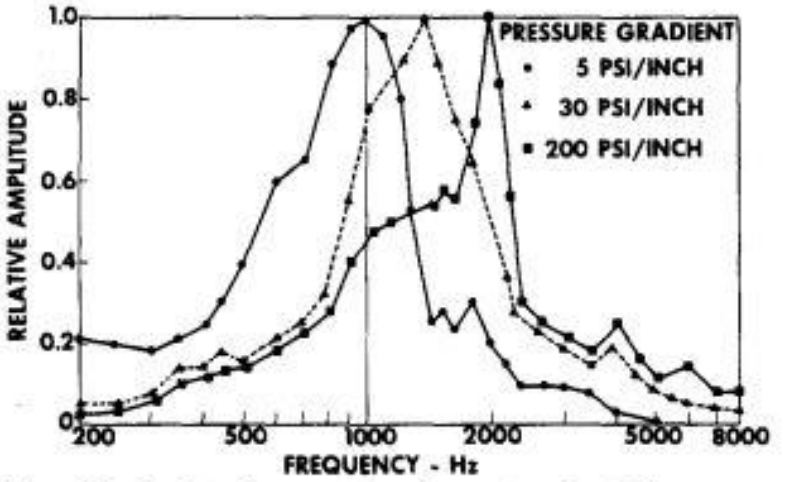

Fig. 3A—Leak-noise spectra for water throttling across various pressure gradients.

Figure 1: Spectra for Fluid Throttled Across an Orifice. Reprinted from McKinley, R. M., Bower, F. M., and Rumble, R. C. 1973. The Structure and Interpretation of Noise from Flow behind Cemented Casing.

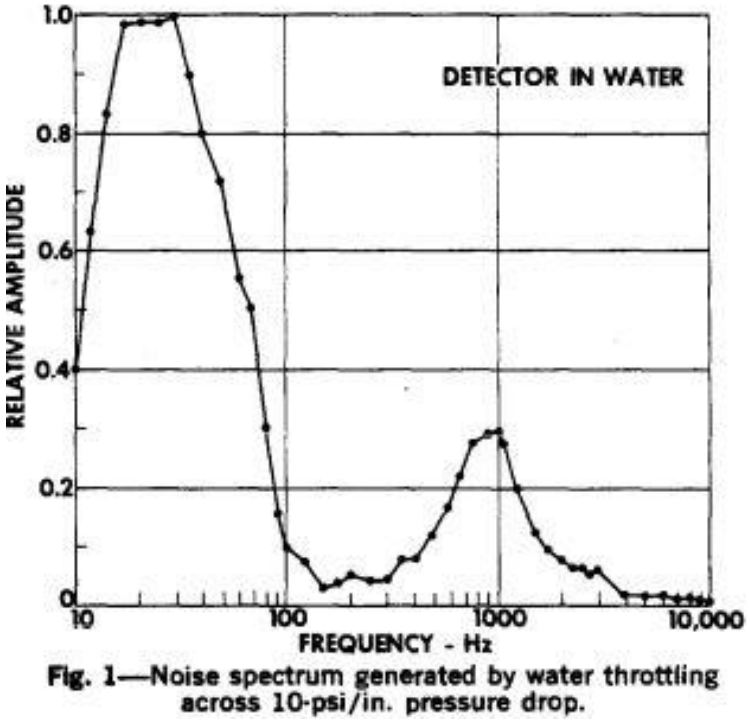

Figure 2: Spectra of Water Throttled Across an Orifice. Reprinted from McKinley, R. M., Bower, F. M., and Rumble, R. C. 1973. The Structure and Interpretation of Noise from Flow behind Cemented Casing.

1.3 Fiber Sensing

Fiber optic sensing systems consist of a fiber optic cable and interrogator. The interrogator pulses a coherent beam of light through the fiber and receives backscattered signal through the fiber. Small imperfections created in the fiber during fabrication cause a backscatter event to occur within the fiber. Elastic backscatter events which do not modulate the frequency of the coherent light are read as Rayleigh backscatter events (Figure 3), which are related to strain along the fiber, and are used to create distributed acoustic sensing (DAS) measurements. Other components such as Brillouin and Raman

scattering are used for seismic and temperature measurements respectively. The backscatter events are measured at the interrogator using a photo amplifier and photosensor within the interrogator. The fiber is not sensitive to force normal to the side of the fiber but is highly sensitive to strain along the length of the fiber which cause deformations within the fiber. These deformations change the size and spatial placement of the aforementioned imperfections in the fiber which cause the elastic backscatter to change in amplitude and travel time back to the interrogator. Acquisition of information related to the change in backscatter amplitude and travel time based on the timing of the pulsed light signal create a spatially distributed, temporally continuous measurement along the fiber. The number of times the length of the fiber can be interrogated per second gives the upper frequency limit which the interrogator is able to resolve for events which induce strain along the fiber. This is dependent on the length of fiber which is being interrogated. Speed of propagation of light within the fiber is defined by:

$$C_{fiber} = C_{Vacuum/\eta_{eff}}$$

where C_{vacuum} is the speed of light within vacuum and η_{eff} is the refractive index of the material. The upper frequency limit for detectable strain events on the fiber is then defined by

$$F_{upper} = \frac{C_{fiber}}{2 * L_{fiber}}$$

Where L_{fiber} is the length of the fiber being interrogated and F_{upper} is the upper limit frequency which can be detected for a particular length of fiber.

A cross sectional diagram of a fiber (Figure 4), shows the internal dimensions of single and multi-mode fibers respectively as well as the proposed light propagation within the fiber. Single mode fiber is used for DAS sensing while multi-mode fibers are typically used for DTS and DSS sensing.

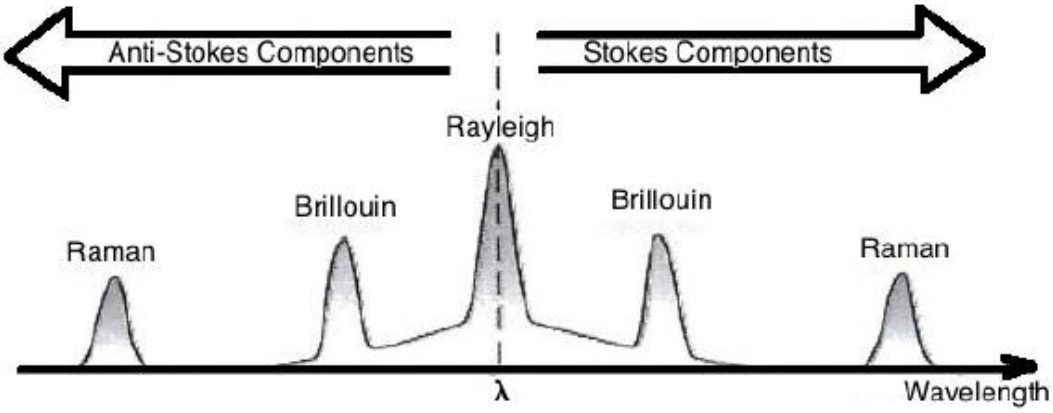

Figure 3: Backscatter Components Used in Fiber Optic Sensing. Reprinted from Martinez, M., Bussières, J., Debruyne, D.,Lava, P. 2013. Load monitoring using a Rayleigh backscattering fibre optic system.

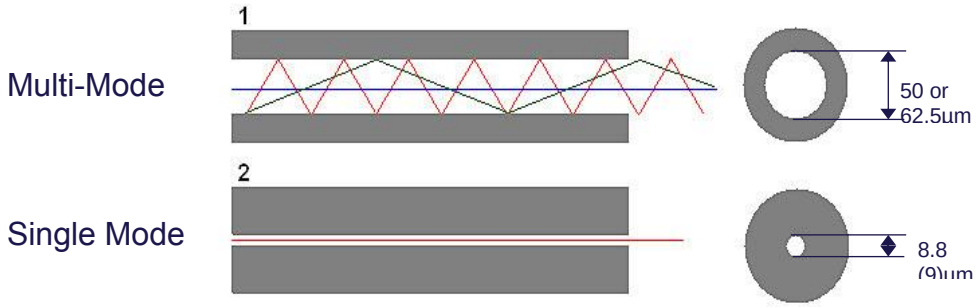

Figure 4: Fiber Optic Cable

1.4 Pore Radius Study

Using the work of Ouyang (2013), which was a numerical and theoretical study of the flow of non-Newtonian flow through propped fractures, it is possible to extract an effective pore radius and pore area for various packing schemes of spherical proppant particles (Figure 5). The packing schemes depicted are side-centered (SC), body-centered (BCC), and face-centered (FCC). In his dissertation Ouyang put forth sets of equations for effective pore radius based various correlations observed in numerical studies using FLUENT.

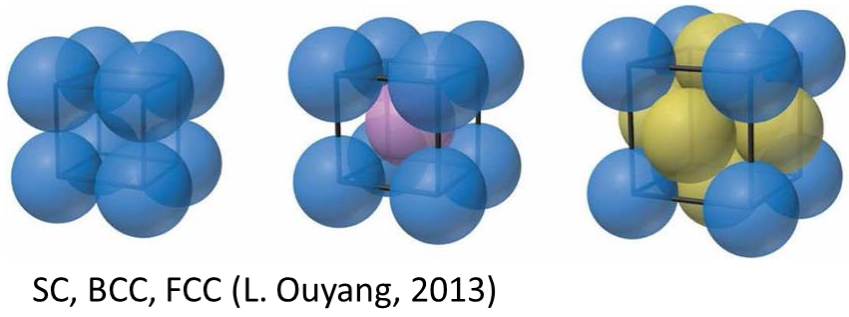

Figure 5: Depiction of Proppant Packing. Reprinted from Ouyang, L. 2013. Theoretical and Numerical Simulations of Non-Newtonian Fluid.

1.5 Sound Propagation in Porous Media

Work done by Biot (1956) pointed to a frequency dependence in the mode of sound propagation within a fluid saturated porous media relating dissipation, attenuation, and propagation of higher frequency and lower frequencies to mechanisms of interaction within the porous media. Viscous dissipation is the main mode of acoustic power loss in the case of higher frequencies, and thermal interactions with the rigid porous media in

the case of lower frequencies. The frequency cutoff between the dissipation modes occurs when the frequency corresponding wavelength is equal to the pore diameter, and the breakdown of Poiseuille flow within the porous media occurs.

Johnson et al. (1987) then related frequency dependent attenuation based on the dynamic permeability and dynamic tortuosity of the porous media relating that attenuation of lower frequencies occurs with the viscous dominated dissipation and inertial dissipation dominated higher frequency dissipation. Champoux, and Allard (1991) built upon this and performed an experimental study to verify the frequency dependence of attenuation by the dynamic tortuosity and dynamic permeability of the media, eventually relating dynamic permeability to bulk modulus of the fluid saturating the porous media the results of which are show in Figure 6. This experimentally points to a frequency dependence of these two physical parameters.

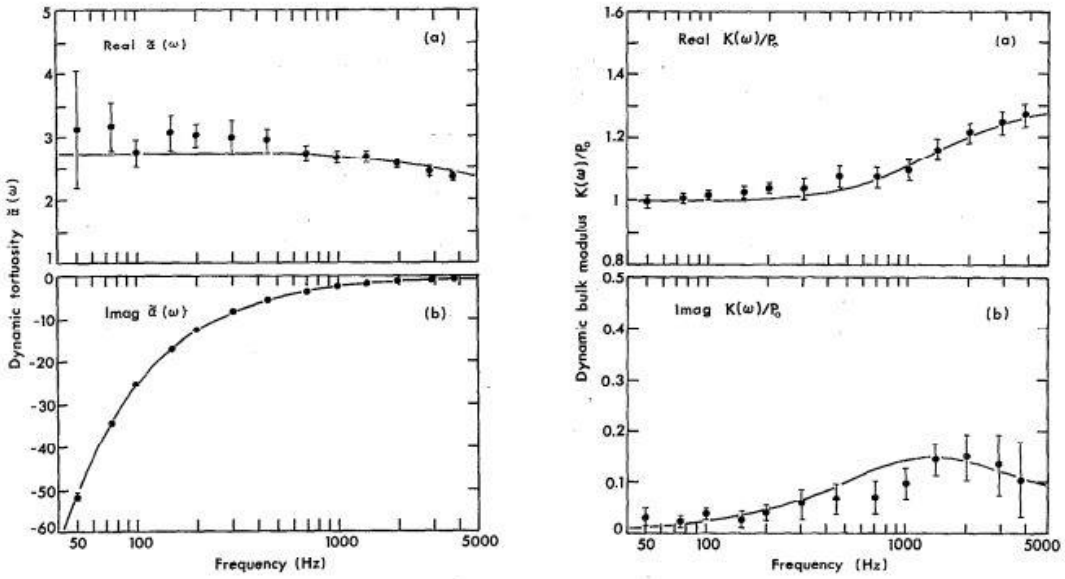

Figure 6: Results of Experimental Dynamic Tortuosity and Bulk Modulus Study. Reprinted from Champoux Y., Allard J. F. 1991. Dynamic Tortuosity and Bulk Modulus in Air-Saturated Porous Media.

1.6 Research Objectives

The objective of this research is further refine the understanding of the effect which permeability of porous media has on the observed acoustic signal of flow for a simulated unconventional completion using the same apparatus and techniques used by Chen (2015) while informing work performed by Martinez (2014). The refinement of the techniques of data acquisition, data processing, and quantitative characterization of the signal from the produced fluid will lead to enhancement of DAS interpretation techniques for production monitoring and allocation, and stimulation operation diagnosis.

2. EXPERIMENTAL SETUP

2.1 Set-up Overview

The experimental apparatus consists of a parallel plate fracture cell filled with various sizes of proppant particles to simulate the near wellbore conditions of a hydraulic fracture. The parallel plate cell is mated to an 8' horizontal length of 5 ½" OD steel casing (consisting of two pieces of steel pipe), which contains a centralized, distributed system of 3 GRAS sound and vibration 40PH microphones, and a Bruel and Kjaer 8103 hydrophone, via a 2" long 3/8" NPT. The 8' section of horizontal pipe is then connected to a 4' section of vertical pipe composed of similar 5 ½" OD steel casing through which the instrumentation cabling is fed as shown in Figure 7. Nitrogen gas is fed from a source tank to the fracture cell and produced into the horizontal length of pipe. The microphones and hydrophone record the acoustic signal of the flow experiment for 10 seconds at a sample rate of 25.6 kHz at 24 bit resolution as a comma-separated value (CSV) file. The acoustic data is calibrated as a pressure measurement, the .CSV file then undergoes post processing using MATLAB code (published in Appendix A, and detailed further in this work) to analyze the spectrum of the acoustic signal, generate band power data, and extract the sound pressure level of the range of interest.

Figure 7: Simulated Wellbore

2.2 Fracture Cell

The parallel plate fracture cell consists of three pieces of machined aluminum: a base place, a central plate with inlet and outlet face ports which attaches to the base plate by machine screws, and a top plate which fits over the assembled base and central plate once the cell is filled with proppant (Figure 8). There is a main O-ring within the cell on the central plate to seal the cell from leaks. The top plate is mated to the assembled base and central plate by a nut and bolt system which equally compresses the O-ring (Figure 9). The cell also features O-rings at inlet and outlet ports to assure there are no leaks

through the ports of the cell. Outer dimensions of the cell are 18”x 10”x 1.7” inner dimensions are 16”x8”x.2”. The inlet face port is fed using a check valve to assure there is no proppant being flowed back through the inlet. The outlet port contains a mesh screen to prevent proppant from being produced through the outlet port (Figure 10).

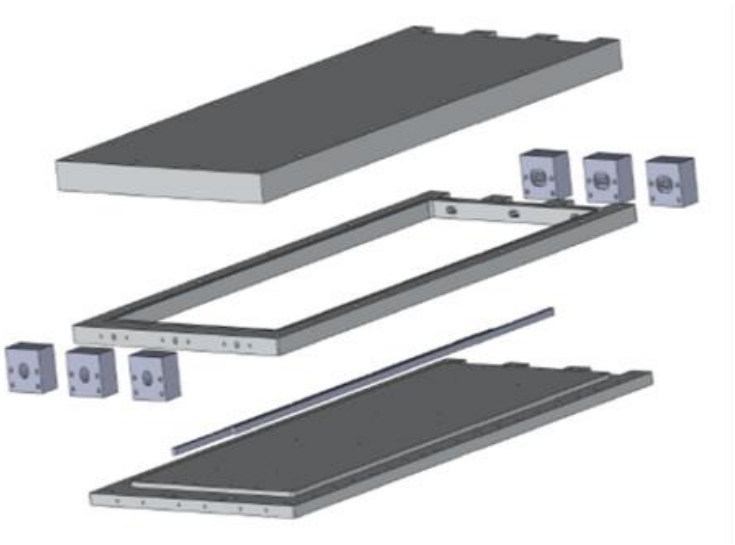

Figure 8: Exploded View of Fracture Cell

Figure 9: Unassembled Fracture Cell

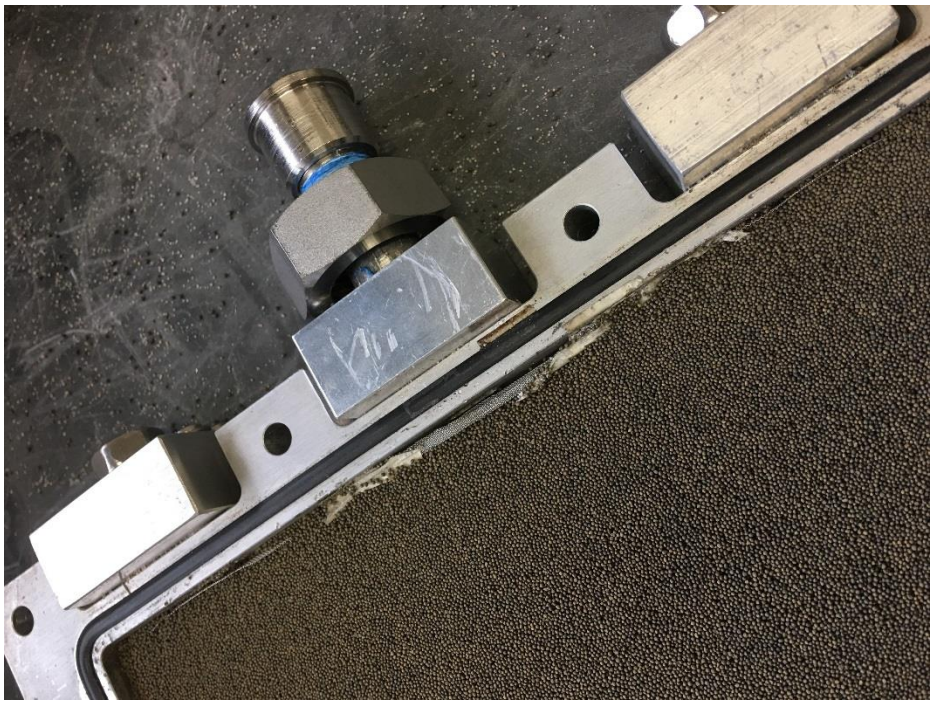

Figure 10: Detail of Outlet Port and Mesh Screen

2.3 Wellbore Setup

The simulated wellbore consists of three pieces: two horizontal steel pipe 5 ½" OD sections each approximately 4' in length with threaded taps to mate the perforation tunnel to wellbore and attach the fracture cell, and a vertical section of steel pipe 5 ½" OD approximately 3.9" in length. There is a flange in the central section of the horizontal wellbore as seen in Figure 7 with a rubber gasket to join and seal the horizontal section of pipe. There is a right angle joint which joins the assembled horizontal section of the simulated wellbore to the vertical section, this is also gasketed at the flanges to assure there are no leaks. The instrumentation is distributed such that the hydrophone is located at the toe of the wellbore, and there are microphones located at each of two threaded taps on the horizontal section and a third microphone is located equidistant between the two threaded taps. The instrumentation is centralized and secured in the wellbore using a PVC tubing with rubber feet to secure and dampen sympathetic vibration within the assembly (Figure 11). High density foam is used to prevent reverberation and directionalize the sensing direction of the microphones (Figure 12, Figure 13). The hydrophone is also secured and directionalized using high density foam. Instrumentation cabling is fed through the heel end of the wellbore to the vertical section of pipe and fed to the data acquisition assembly.

Figure 11: Distributed Sensing Array and PVC Centralizer

Figure 12: Detail of Microphone and Foam

Figure 13: Distributed Sensing Array Toe

2.4 Data Acquisition Assembly

Data acquisition is performed using a Bruel and Kjaer type 8103 hydrophone (Figure 14), and 3 GRAS sound and vibration 40PH microphones (Figure 16). The hydrophone is a piezo-electric device which senses pressure disturbances and generates a voltage when a pressure is applied to the piezo-electric element. The useable range of the hydrophone is .1 Hz to 180 kHz, well within the range of interest for experiments performed. The hydrophone voltage signal is then fed to a Bruel and Kjaer Nexus single channel charge amplifier (Figure 15) via a shielded single conductor BNC cable. The amplifier amplifies the incoming voltage signal and converts the pressure reading from the hydrophone to volts. The output of the charge amplifier is then fed to one channel of the National Instruments 9234 4-channel data acquisition module for vibration and

sound (Figure 17). The NIDAQ records voltages for all instrumentation, has a sampling capability of 51.2 k samples/sec/channel and a ±5 V range for data for recording with the data acquisition software. The distributed microphones record pressure by outputting a voltage which is fed by BNC to the NIDAQ to the remaining 3 channels. The sensing range of the microphones is between 10 Hz and 20 kHz, with a dynamic range upper limit of 135dB. The NIDAQ is then connected to the data acquisition PC via a USB cable. A block diagram of the data acquisition assembly can be seen in Figure 18.

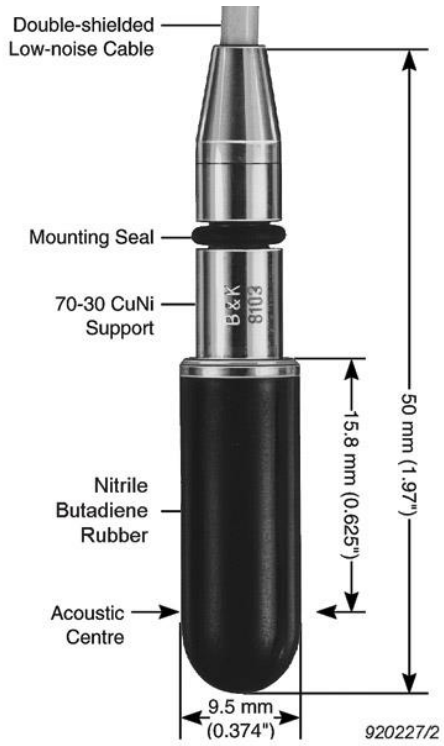

Figure 14: Hydrophone

Figure 15: Bruel and Kjaer Charge Amplifier

Figure 16: Microphone

Figure 17: National Instruments 9234

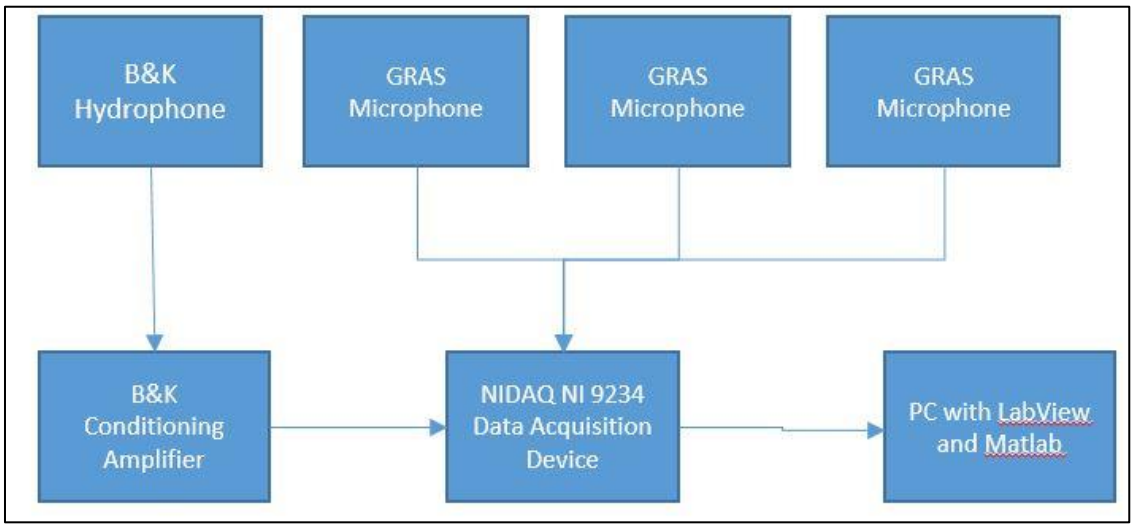

Figure 18: Data Acquisition Assembly Block Diagram

2.5 Data Acquisition Software

A data acquisition application developed in LabVIEW (block diagram is visible in Appendix C) is used to acquire data and control the NIDAQ. The application's front

panel (Figure 19) and main interface has space to define a target location for the acquired data. The application interface also displays amplitude, spectral power, and phase data as a form of confirmation of data acquisition (analysis is performed in post processing using MATLAB), and data quality assurance. The application block diagram allows for deeper access to features to change sampling rate of the data acquisition devices, bit-rate, and calibration of instrumentation.

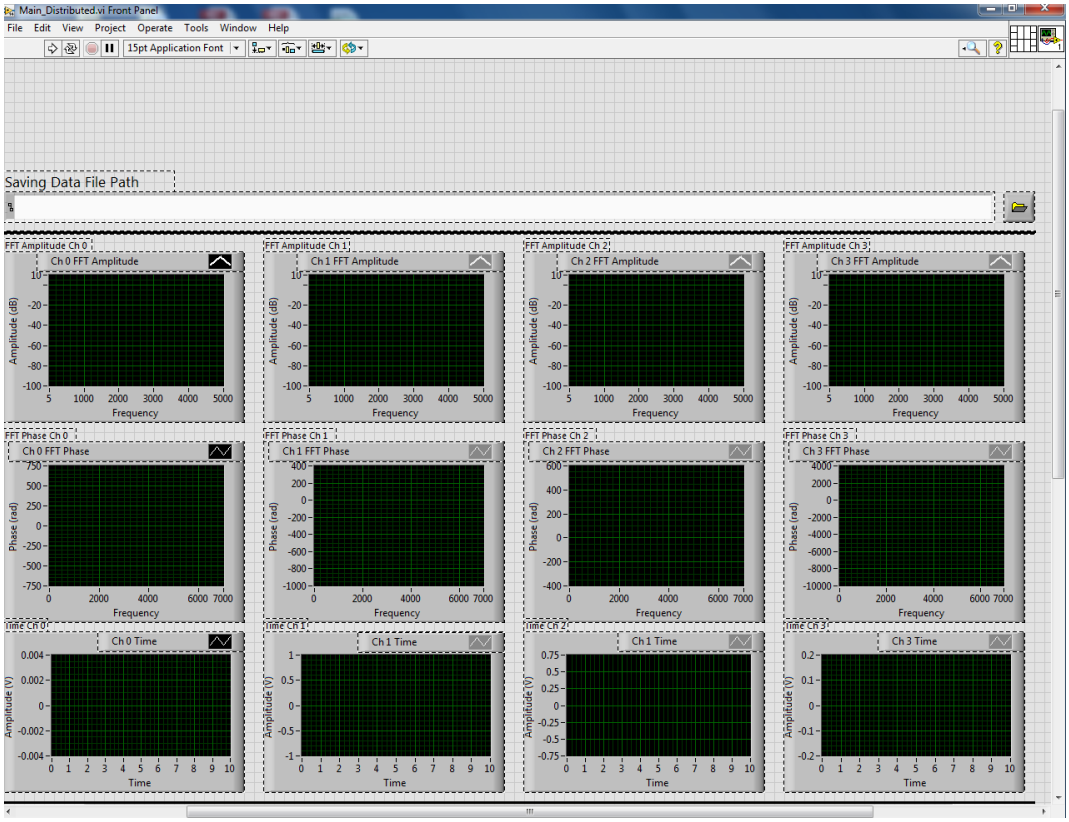

Figure 19: Data Acquisition Application Front Panel

2.6 Set-up and Assembly Procedures

Experiments are performed in a run format incrementing injection pressure from the source tank in 10 PSIG increments, and rerun the desired number of times for each experimental setup. Cell filling, assembly, and installation procedures are as follows:

1. Begin by setting the emptied cell bottom on a flat benchtop surface and partially fill the cell with the desired proppant size allowing space for the lid to sit in place as there is a lip on the cell where the two cell halves are joined. Partially filled fracture cell shown in Figure 20.
2. Install the nuts and bolts to secure the cell halves together and finger tighten.
3. As all the bolts are installed tightening of the bolts may begin. Begin by tightening one of the bolts at the center of the cell by holding the nut in place with a 3/16" crescent wrench and tightening the bolt head using the corresponding sized socket wrench attachment and socket wrench.
4. Work in an "X" pattern starting from the center of the cell tightening the bolt on the opposite diagonal side of the cell to equally compress the O-ring internally mounted in the cell.
5. When all bolts on the long edges of the cell are secured the bolts on the short edges are tightened in the same manner working in an "X" pattern to the bolt on the opposite diagonal from the bolt which was last secured, again to ensure the O-ring is compressed equally during the installation. Fully assembled fracture cell shown in Figure 21.

6. Uninstall the inlet face port, and use masking tape to cover the screw holes for the inlet face port.
7. Rest the cell vertically on the outlet port and continue filling the cell by gravity feeding proppant through the open inlet port.
8. When cell is filled or begins to overflow remove masking tape, reinstall inlet face port, attach via hose to an air pressure source and use the air pressure source to pressure pack the proppant within the cell. Repeat 6-8 a total of three times to properly pack the fracture cell.
9. Couple the fracture cell to the horizontal section of pipe using the attached pipe union at the outlet face plate using a large adjustable crescent wrench being mindful of the angle of attachment.
10. Connect the outlet of the nitrogen gas source tank regulator to the inlet faceplate check valve, using a 3/16” wrench to tighten collar fitting. Fully installed fracture cell shown in Figure 22.

Figure 20: Partially Filled Fracture Cell

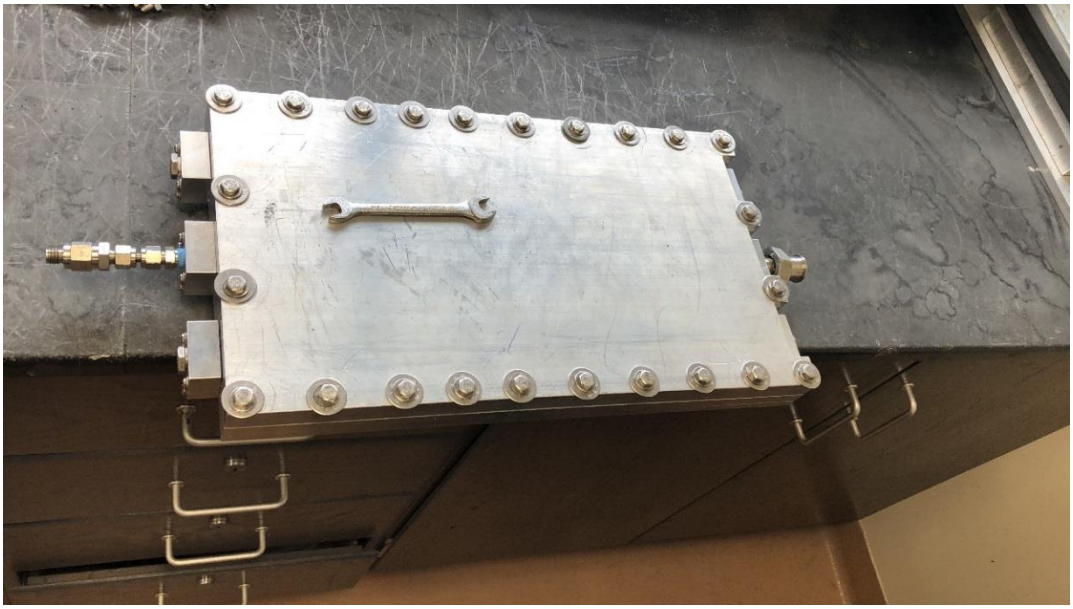

Figure 21: Fully Assembled Fracture Cell

Figure 22: Fracture Cell Coupled to Wellbore

2.7 Measurement and Data Acquisition Procedure

Once the cell is properly assembled and mated to the casing data collection can be performed.

1. Initialize Labview based data acquisition software and generate a target folder and an initial target excel file within the first run sub-folder.
2. Turn on charge amplifier for hydrophone and confirm amplifier setting for conversion of V/Pa.

3. Use filename browser in the Labview application to select the target excel file within the first run sub-folder to capture the target folder name, and edit the target name to reflect the run information for the experiment
4. Set injection pressure at the regulator of the nitrogen tank to the initial run value.
5. Run data acquisition software and allow for acquisition to occur, confirm data is written to target folder, and stop application to stop acquisition (if application is not stopped it will continue to run and overwrite the target file after acquisition time interval has passed again).
6. Change injection pressure for next experiment and edit target file name to reflect new injection pressure. Repeat acquisition run and stop procedures. Complete all experimental injection pressures
7. Once a run is complete edit the target folder name to reflect the new run. Repeat injection pressure incrementation and data acquisition procedures outlined in previous steps.
8. After all runs are completed with the proppant pack detach fracture cell from the horizontal pipe and rest the fracture on the bottom plate.
9. Couple the rotameter to the fracture cell using the pipe union attachment
10. Adjust inlet pressure until rotameter reads a flowrate at one of the demarcated graduations, record the inlet pressure and flowrate. Repeat through the useable range of the rotameter (limited by inlet pressure). Experiments run for this study are detailed in Table 1.

Experiment	Proppant Size	Injection Pressure Range (PSIG)	Injection Pressure Increment (PSI)
1	Empty cell	10-100	10
2	16/30 mesh	10-100	10
3	20/40 mesh	10-100	10
4	30/50 mesh	10-100	10
5	16/30-30/50 mixed	10-100	10
6	20/40-30/50 mixed	10-100	10
7	40/70 mesh	10-100	10
8	100 mesh	10-100	10

Table 1: Experimental Runs

2.8 Signal Processing Procedure

Processing of the generated pressure data was performed with custom MATLAB script and functions (published in Appendix A). The processing procedure can be carried out using the following methodology

1. Open MATLAB script entitled “run.m” be sure the “evalueationbeta.m” function is within the same directory.

2. Change target file name to the folder directory of the target raw data. Be sure that the target run numbers are represented within the script as well as the target inlet pressure files.
3. Update the run length information, and sample rate information in the script if these have changed from default (10 seconds, and 25.6 kHz respectively).
4. Adjust low and high pass filter parameters to extract target segment of the spectrum (set to 1 kHz and 7 kHz as default).
5. Within the "run.m" script set target excel .xls files to write the final analyzed data.
6. Run script, spectrograms using a Welch Power (Pwelch) function are generated showing the spectrum within frequencies of interest and output as image files within the source directory, octave band power and 1/3 band power functions are generated and appended to the output excel sheet.
7. SPL data is calculated by first filtering the time domain pressure data using a high and low pass filter (the order of which can be set) using the cutoff frequencies set in the "run.m" script, then a Fast Fourier Transform (FFT) is taken of the resultant filtered pressure data.
8. A root-mean square function is then performed on the resultant spectrum and the SPL is calculated using the following formula:

$$SPL = 10Log_{10}(\frac{P_{rms}^2}{P_{ref}^2})$$

SPL is then appended to the output excel sheet. P_{ref} can be set within the "evaluation.m" function. In the case of these experiments a P_{ref} of .00002 Pa was used.

3. EXPERIMENTAL RESULTS

3.1 Acoustic Effect of Pack Permeability

Proppant packs of various particle sizes are loaded into the fracture cell to vary pack permeability and their effect on generated acoustic signal are compared. Changes in flow rate, N_{re}, pore radius, pore area, and pack permeability are calculated after data processing for comparison of the proppant packs and the observed acoustic signal.

3.2 Example of Workflow

Beginning with a 16/30 mesh proppant size, measurements are taken and raw acoustic pressure data is processed and filtered using MATLAB code. Recorded raw acoustic signal, Figure 23, is treated with high and low pass filters to remove lab noise and extract the SPL of the target section of the spectrum between 1 kHz and 7 kHz.

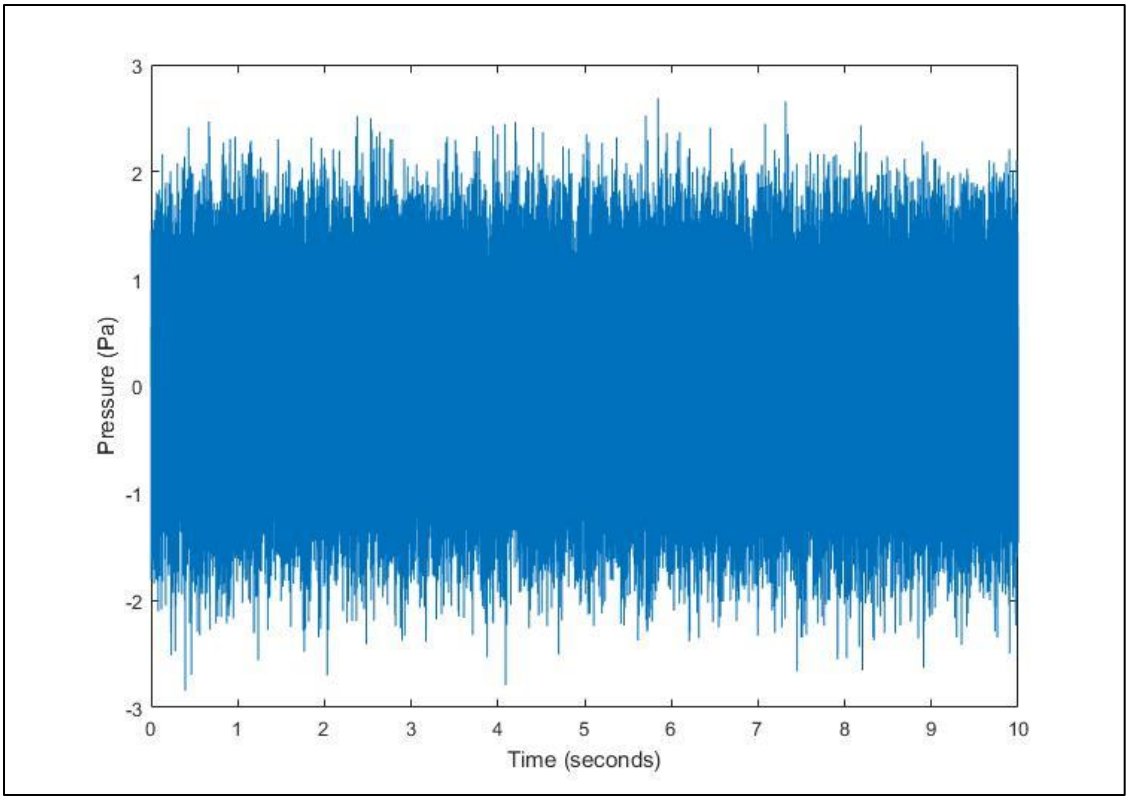

Figure 23: Recorded Acoustic Signal

Spectrograms are produced from the Welch Power Function from the raw pressure data for comparison and observation of spectral phenomena. Comparing the spectrogram at 10 PSIG injection pressure, Figure 24, to 100 PSIG injection pressure, Figure 25, it can be observed that the spectral content of the signal shifts from a broad and noisy signal with a peak centered at 5.5 kHz at low injection pressure and flow rate to a more concentrated signal centered around 1.5 kHz at higher injection pressure and flow rate. The spectral trend holds through all other experiments, and proppant pack permeabilities. As the SPL calculation is performed on the root mean square of the

spectrum across the range of interest concentration of spectral power may have an effect on the calculated sound pressure level.

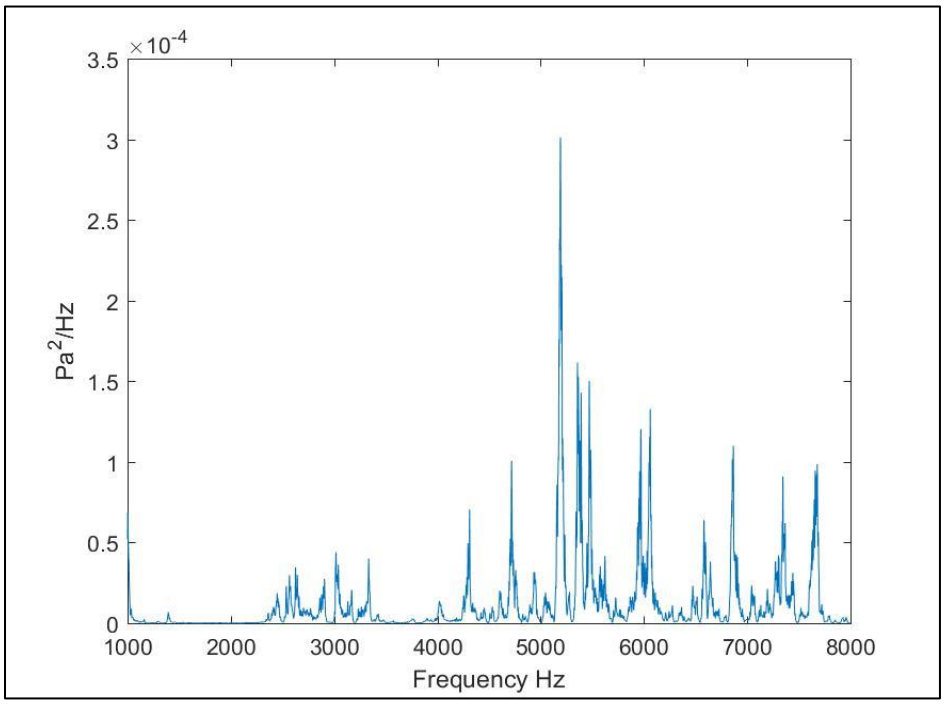

Figure 24: Spectrogram 16/30 Mesh 10 PSIG Injection

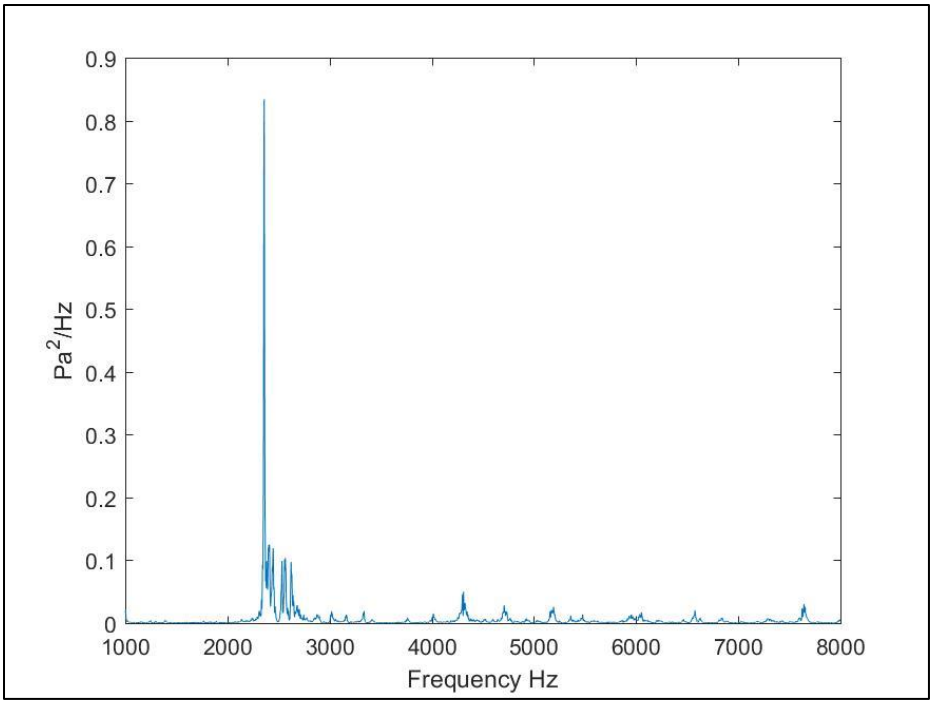

Figure 25: Spectrogram 16/30 Mesh 100 PSIG Injection

After acoustic data is collected flow rate data is collected using a rotameter across the injection pressures used within the experiment, and an injection pressure versus flowrate profile is generated as shown in Figure 26.

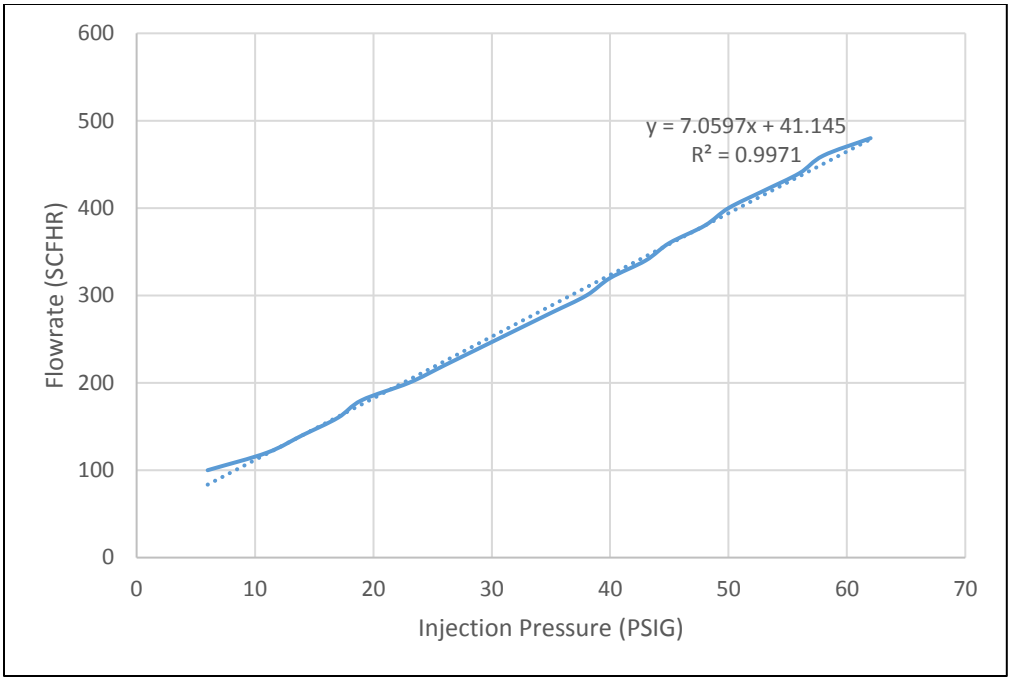

Figure 26: Injection Pressure Profile 16/30 Mesh

Using the linear relation of injection pressure to flowrate it is then possible to calculate flowrate for experiments and compare the SPL of a particular experiment to its corresponding flowrate, compare the SPL to N_{re}, and find the fit of the data using the $Log_{10}(Q^3)$=A*SPL+B correlation put forth by Chen (2015). Figure 27 displays the comparison of the generated flowrate curve to the calculated SPL from the averaged runs of 16/30 mesh. The form of the line shows a saturation of signal as the flowrate increases.

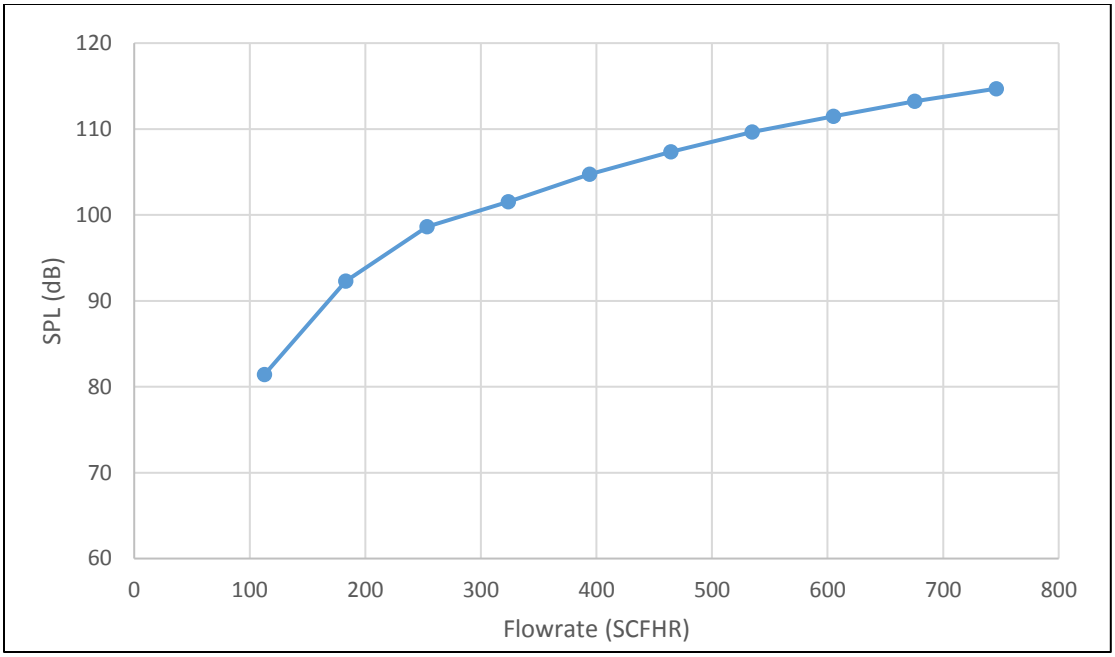

Figure 27: Flowrate and SPL Comparison for 16/30 Mesh

Figure 28 shows the comparison of N_{re} and SPL, N_{re} is calculated at the exit of the perforation tunnel and reflects a highly turbulent regime through the experimental

run. The equation used to calculate the Reynolds number at the perforation tunnel is as follows:

$$N_{re} = \frac{4q\rho}{\pi D\mu}$$

Again, the signal begins to saturate at the higher N_{re} corresponding to the higher injection rates and concentration of signal within the narrow 1.5 kHz band.

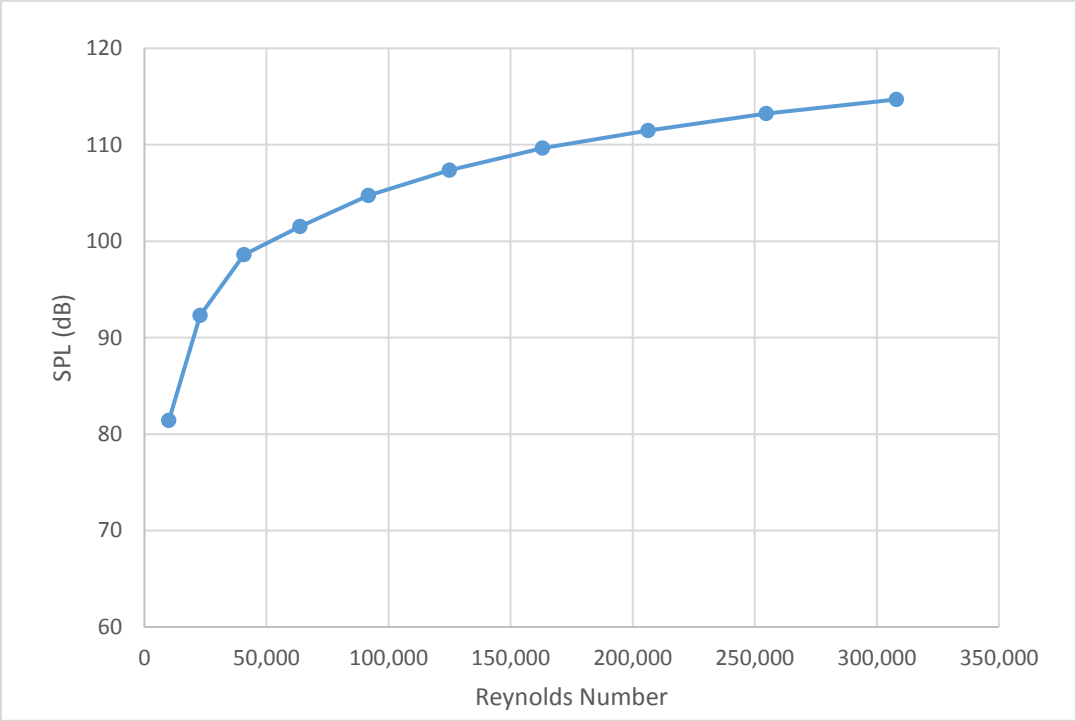

Figure 28: Reynolds Number and SPL Comparison for 16//30 Mesh

SPL versus $Log_{10}(Q^3)$ can then be plotted and correlation constants A and B can be extracted from the slope and intercept of the linear fit of the data as shown in Figure 29 respectively.

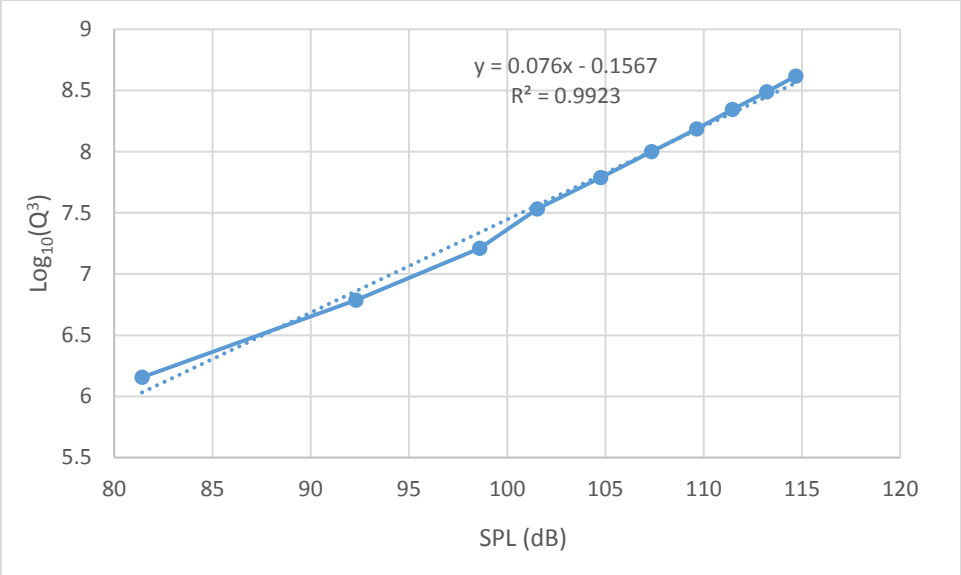

Figure 29: $Log_{10}(Q^3)$ and SPL Comparison for 16/30 Mesh

Using Ouyang's (2013) work on effective pore radius correlations it is possible to calculate the pore radius and pore area for the proppant pack, Figure 30, using various geometry correlations developed in that work. From this point forward side-centered geometry will be used for pure proppant experiments.

16/30 Mesh	SC Pore Radius (m)	9.21E-05
	SC Pore Area (m^2)	2.66E-08
	BCC Pore Radius (m)	8.79E-05
	BCC Pore Area (m^2)	2.43E-08
	BCC2 Pore Radius (m)	7.57E-05

	BCC2 Pore Area (m^2)	1.80E-08
	FCC Pore Radius (m)	7.28E-05
	FCC Pore Area (m^2)	1.66E-08

Figure 30: Pore Radius and Area for 16/30 Mesh

Using the non-Darcy flow equation:

$$\frac{M_w(P_1^2 - P_2^2)}{2zRT\mu L(\frac{W}{A})} = \frac{W}{A}\frac{\mathrm{B}}{\mu} + \frac{1}{k}$$

it is possible to calculate the absolute permeability and turbulence factor of the proppant pack from injection pressure and outlet flowrate data for the experiment by plotting $\frac{M_w(P_1^2-P_2^2)}{2zRT\mu L(\frac{W}{A})}$ versus $\frac{W}{A}\mu$ and extracting the intercept and slope respectively as show in Figure 31. The reciprocal of the intercept giving the absolute permeability of the porous media while the slope gives the turbulence factor.

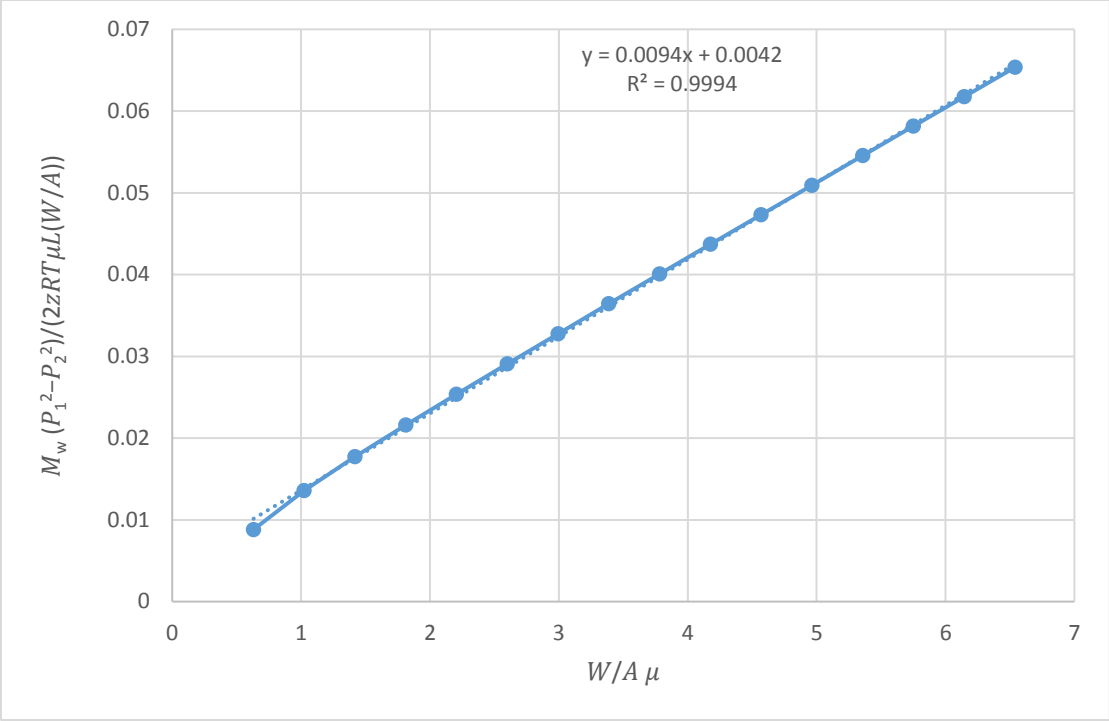

Figure 31: Non-Darcy Flow Permeability Extraction

3.3 Compiled Results

Following the workflow set forth in the previous section it is then possible to generate flowrate versus SPL, Figure 32, N_{re} versus SPL, Figure 34, and $Log_{10}(Q^3)$ versus SPL, Figure 37 for all proppant packs. Comparison of only pure mesh sizes and the empty cell can be seen in Figure 33, Figure 35, and Figure 38.

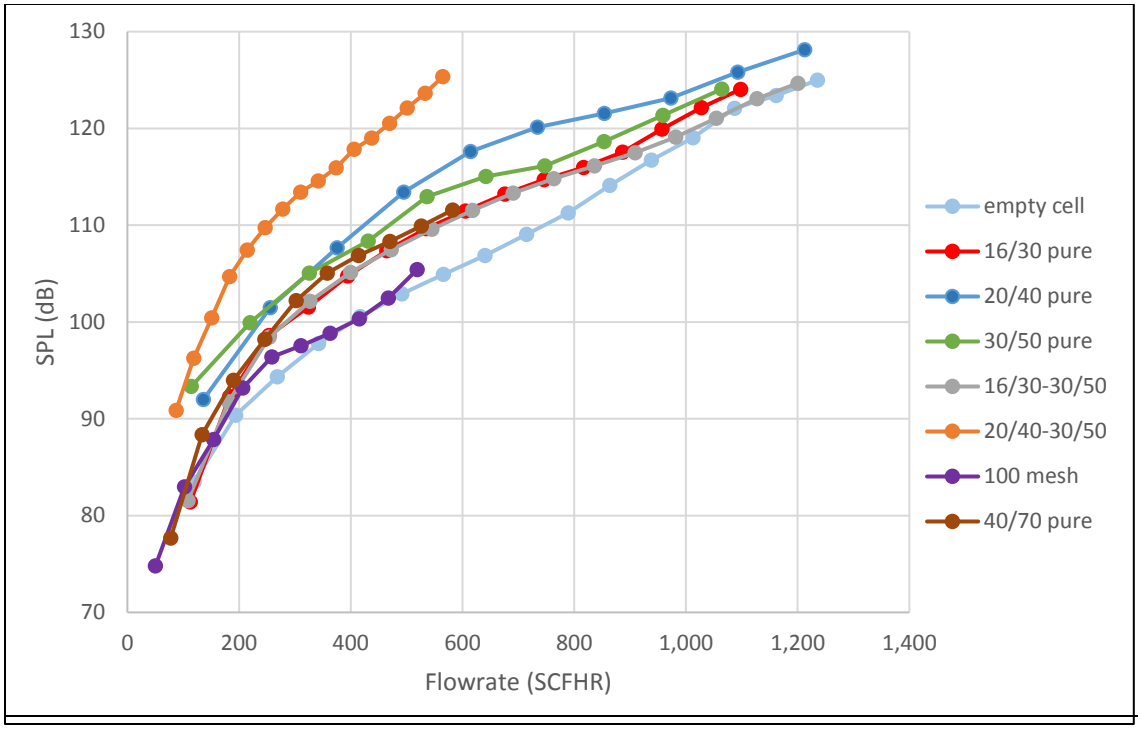

Figure 32: Flowrate Comparison All Cell Experiments

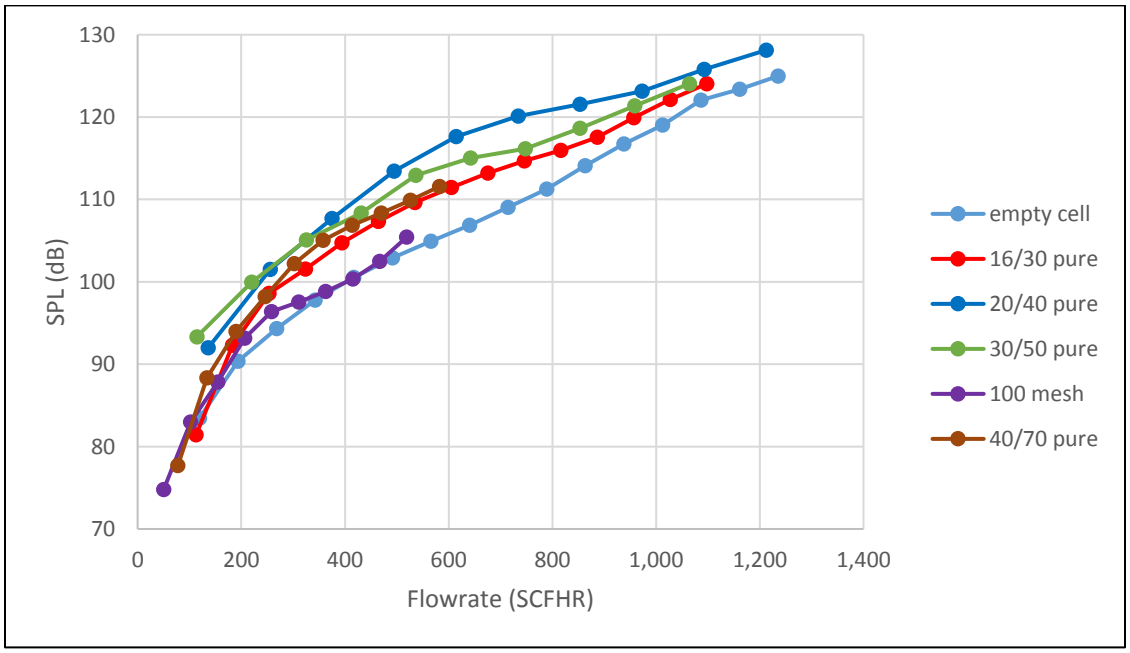

Figure 33: Flowrate Comparison Pure Mesh Sizes

Empty cell experiments show the lowest SPL compared to proppant filled cell experiments with similar flowrates, as confirmed by Chen (2015). Unlike experiments by Martinez (2014) done using a proppant filled pipe, changes in proppant size and permeability for the fracture cell experiment do affect the sound pressure level, while not drastically affecting the location of peak frequencies within the signal. Experiments using the fracture cell also saturate and are not linear past a certain flowrate. This may be due to increasing the flowrate significantly over the experiments performed by Martinez (2014), Martinez does mention a bend at the upper end of his flowrate range but states that proppant size does not affect noise generation as SPL varies linearly with flowrate. Experiments at the higher end of the flowrate curve do begin to converge and saturate above 120 dB this may be due to the location of the microphone in the direct path of the mean flow. Some contribution in this range of flowrates would be generated through the proppant pack as filled cells have higher SPL measurements than the empty cell.

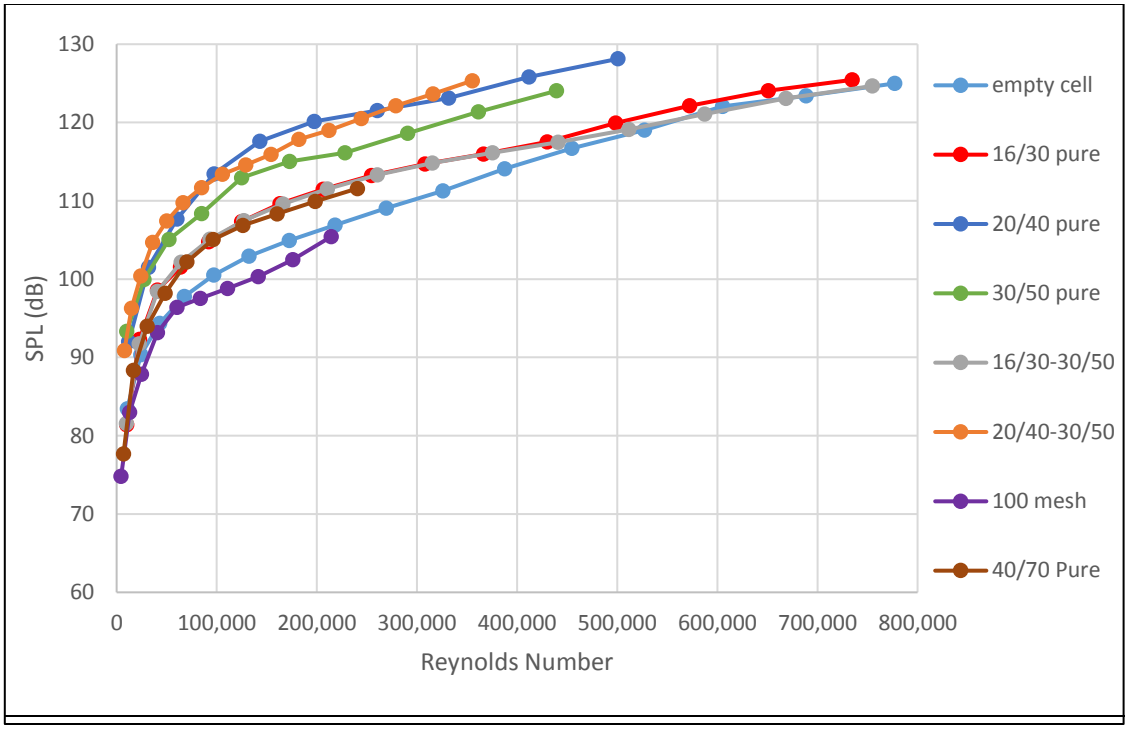

Figure 34: Reynolds Number Comparison All Cell Experiments

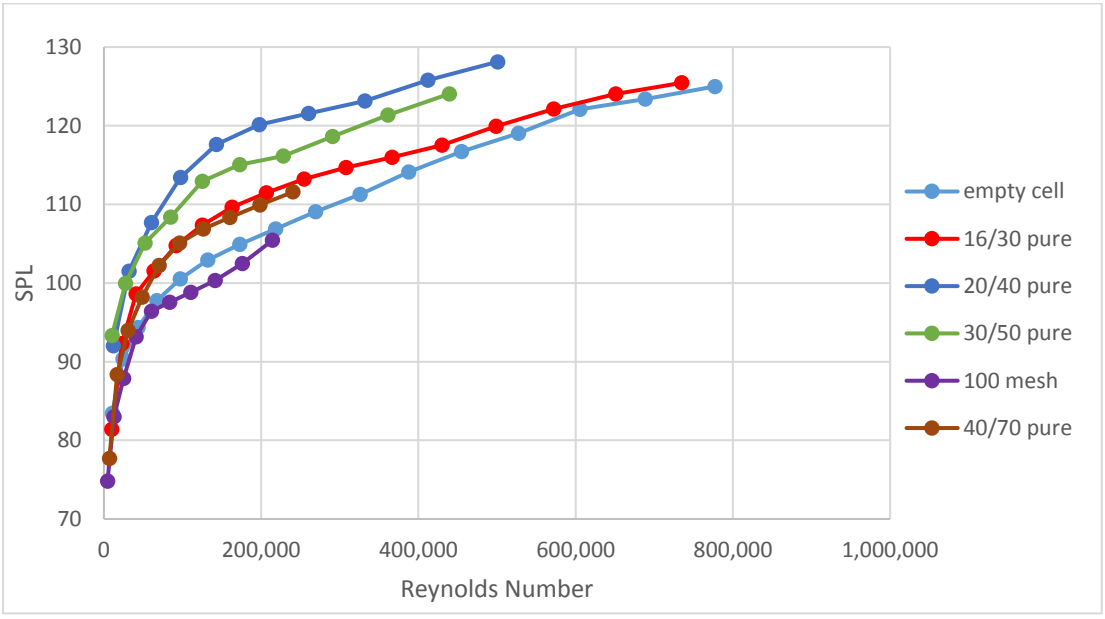

Figure 35: Reynolds Number Comparison Pure Mesh Sizes

All measured N_{re} are above 4000, thus all experiments are turbulent flow. Comparison of N_{re} and SPL of acoustic signal also shows a saturating effect at the higher end of experimental range but distinct SPL curves for the various proppant packs. Comparison of the measured permeability of the experiments in Figure 32, and Figure 34 shows changes in the permeability of the proppant pack and N_{re} of the produced fluid have a combined effect on the SPL of the observed signal. For example, 20/40-30/50 mixed and 1630 proppant packs have the same measured permeability but show different SPL measurements for similar N_{re} which would point to pore size distribution and effective pore radius being factors in the generation of noise. As the 20/40-30/50 mixed proppant experiment would lead to random packing it was not possible to calculate a pore radius or pore area using Ouyang's work, but it would be assumed that pore size would be smaller than a similarly packed 16/30 mesh proppant pack. A similar occurrence is observed between 20/40 and 16/30-30/50, measured permeability is similar but flow through the 20/40 pack produces a higher SPL at similar N_{re}. Because of the diminutive dimensions of the fracture cell and the high permeability of the proppant packs pressure drop across the fracture cell varies between 1.67 Psi, and 11.05 Psi for 1630 proppant and .73 Psi, and 7.6 Psi for 100 mesh. Relatively small pressure drops across the fracture cell, similar N_{re}, but changes in the SPL and A correlation value with variances in pore area and permeability point to a dependence of the acoustic signal on not only the permeability of the proppant back but the effective pore radius of the pack as well. Correlation values in Figure 36 are derived from the linear fit of the plotted data in Figure 37. Figure 38, depicts the SPL and $Log_{10}(Q^3)$ plot for only pure proppant

experiments. Changes in the absolute permeability of the proppant pack show a negative correlation with the A correlation value, Figure 39 and Figure 39Figure 40. Extracted correlation values are plotted against the absolute permeability in Figure 39, Figure 40, Figure 41, and Figure 42.

Proppant Pack	**A Correlation Value**	**B Correlation Value**	**Permeability (Darcy)**	**SC Pore Radius (m)**	**SC Pore Area (m^2)**
Empty Cell	.0711	.60908			
16/30	.07362	.88331	238	9.21E-05	2.66E-08
20/40	.07879	-.81657	197	5.25E-05	8.67E-09
30/50	.09443	-2.45911	96	3.71E-05	4.32E-09
40/70	.077797	-.46597	137	2.27E-.05	1.62E-09
100	.10137	-2.42252	67	1.31E-05	5.39E-10
16/30-30/50 Mixed	.07709	-.26091	198		
20/40-30/50 Mixed	.07285	-.79443	239		

Figure 36: Proppant Pack Permeabilities and Correlation Values

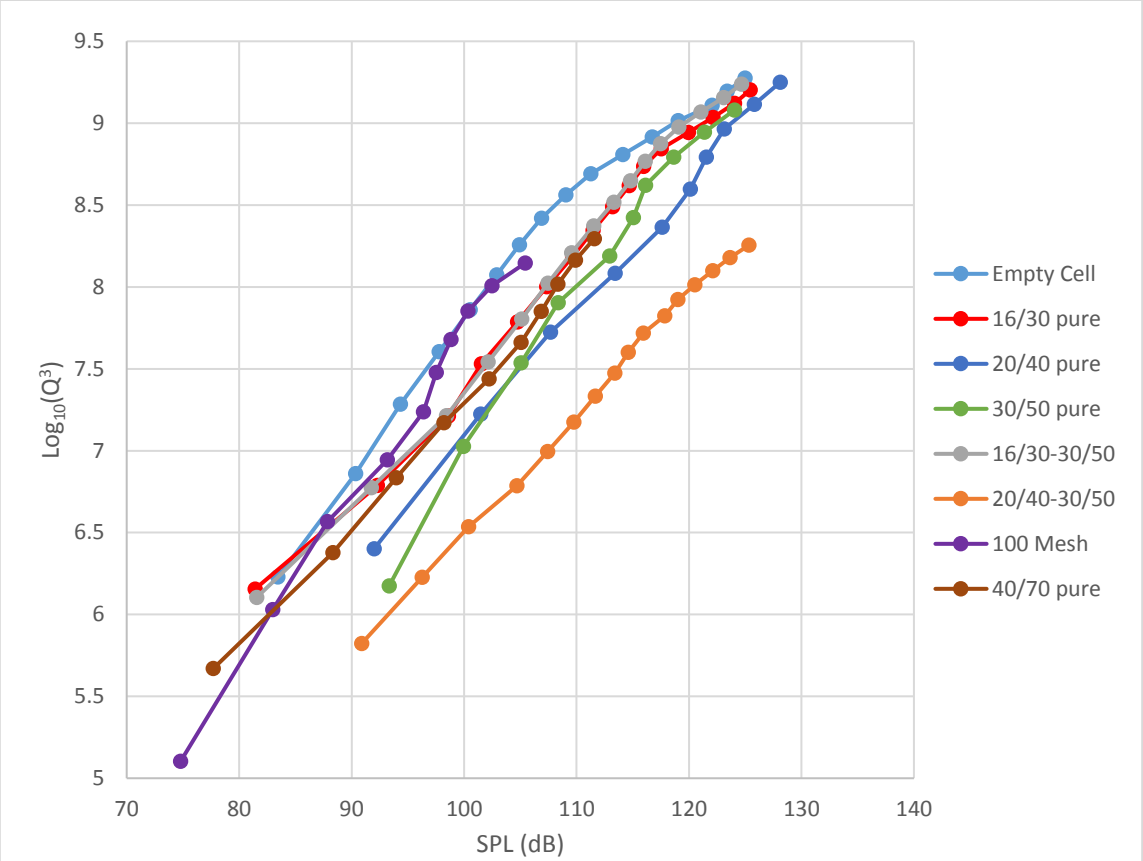

Figure 37:Log_{10} (Q^3) Comparison All Cell Experiments

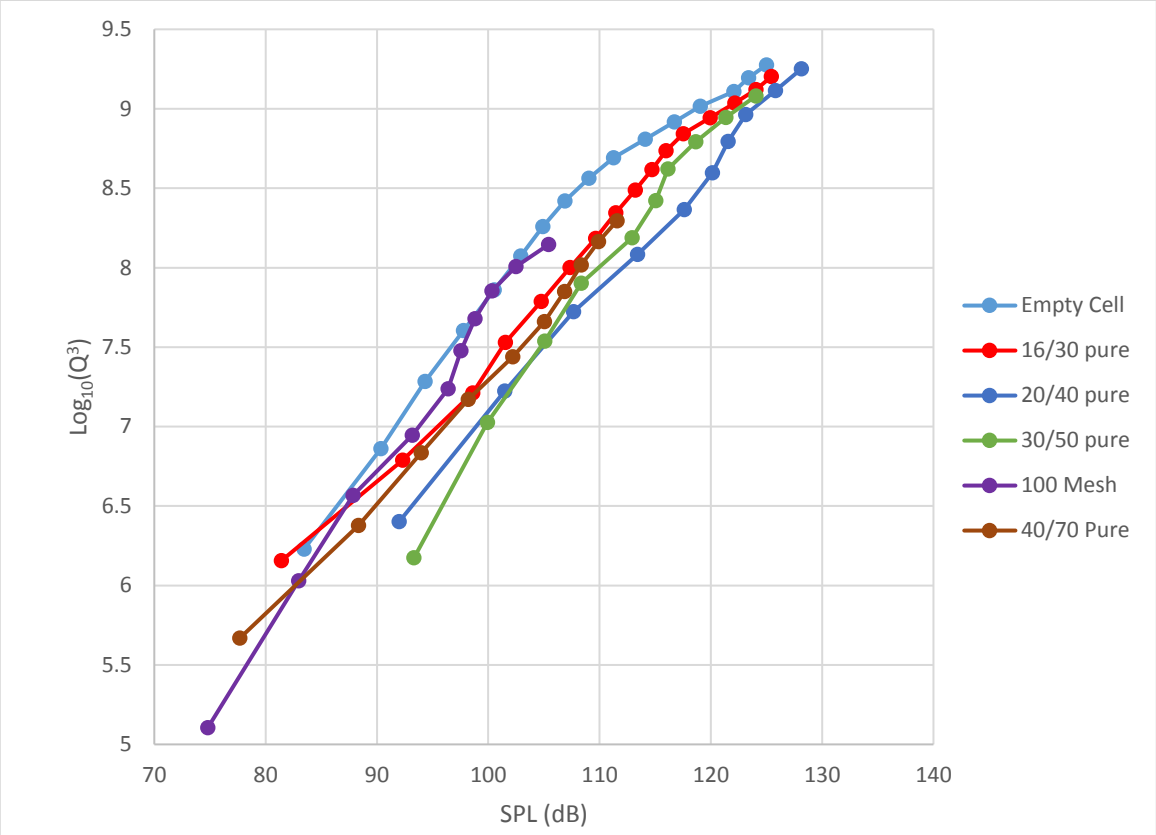

Figure 38:Log$_{10}$ (Q^3) Comparison Pure Mesh

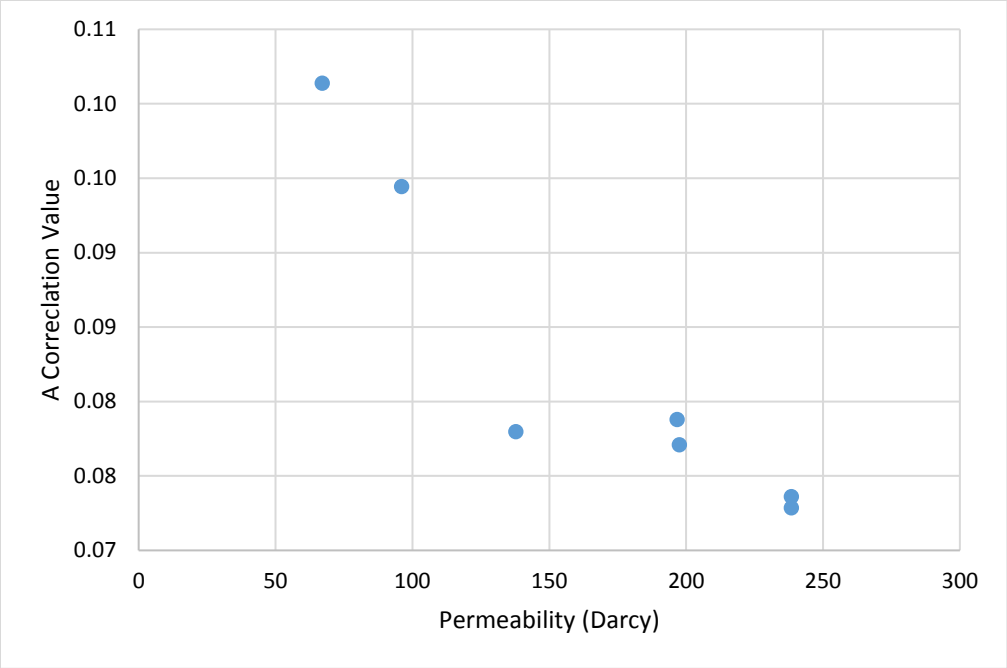

Figure 39: A Correlation Values for All Cell Experiments

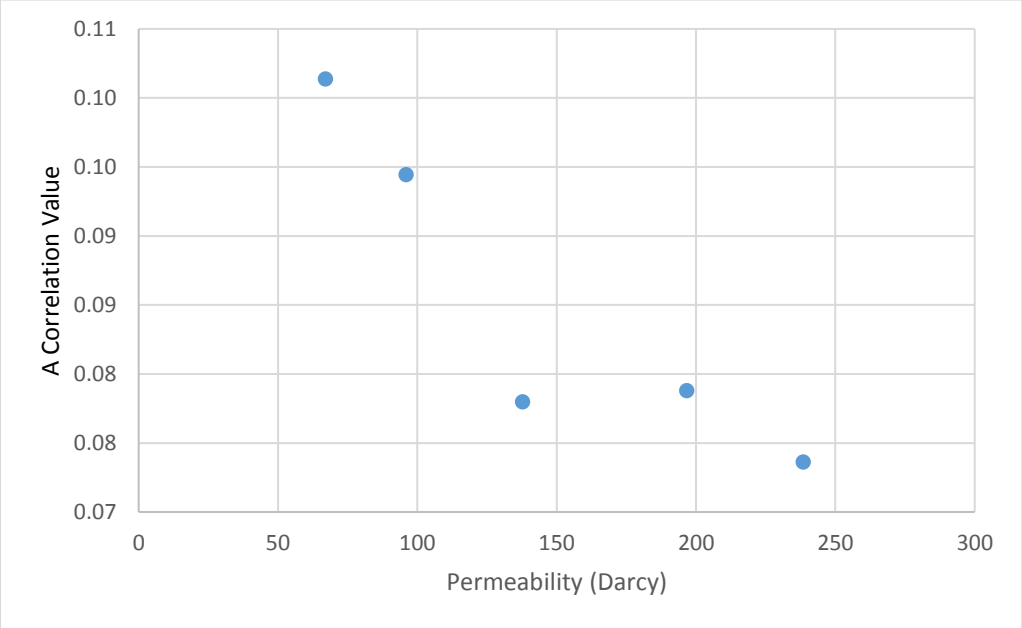

Figure 40: A Correlation Values for Pure Mesh Experiments

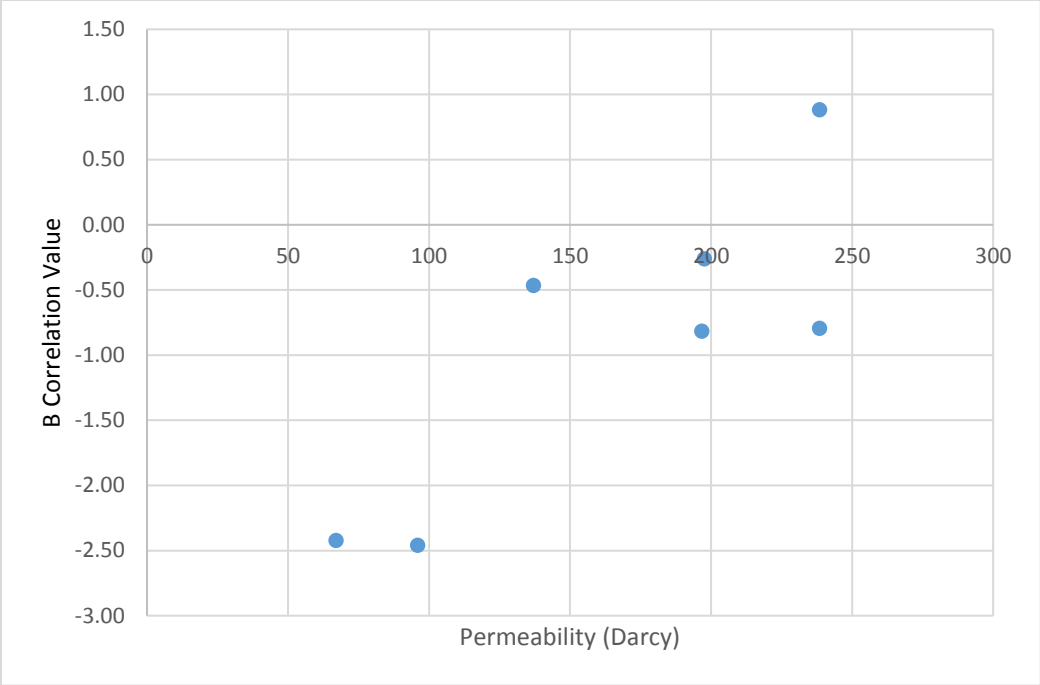

Figure 41: B Correlation Values for All Cell Experiments

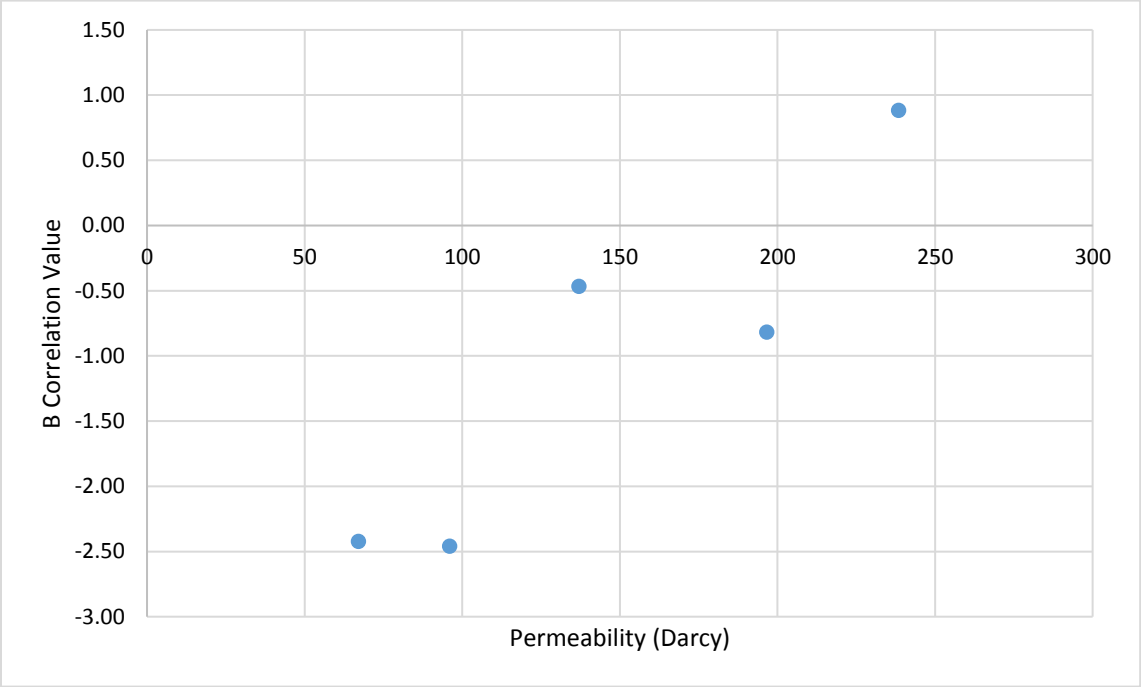

Figure 42: B Correlation Values for Pure Mesh Experiments

4. SUMMARY AND CONCLUSIONS

A general trend of increase of A correlation value with decrease in permeability points to the need of an increased level of flow power within a lower permeability pack to achieve the same SPL as a pack of higher permeability. This was alluded to in the work published by Martinez. The lack of dependence on N_{re}, for SPL of similar permeability proppant packs shows that the flowrate of the produced fluid at the exit orifice is not solely responsible for the sound generated by flow through the simulated fracture. For this study it is shown that attenuation and dissipation within the porous media, and pore radius has an effect on the SPL trend across the flowrates investigated. Further investigation into these trends can be performed using computational fluid dynamic (CFD) simulations of flow through various porous media configurations. The ability to vary the porosity and pore radius of porous media to generate fracture cells with the same permeability but differing pore radii would allow for confirmation of the observations of this study.

For experiments performed within this study pore size falls well below the threshold for consideration of dynamic tortuosity and thus only attenuation and dissipation using Champoux and Allard's model could be used to determine the attenuation of frequencies within the porous media (the lowest cutoff frequency calculated for this value was at 16/30 mesh with a cutoff frequency of 2.633 MHz). Correlation between the dynamic permeability, and attenuation of band power of certain frequency bands and subsequent changes to SPL may be a way to determine the effect

which pore radius has on SPL and the create a way to characterize the expected signal from production after a stimulation operation for comparison to the recorded signal.

Use of a gas with a z-factor of 1 and an idealized fracture geometry with a perfectly cylindrical perforation tunnel create limitations for characterization for direct application of experimental results in a field case. Flow through a more realistic configuration or modeling of a more accurate completion would further inform future implementation of findings and exploration of correlation. Compressibility and change in the bulk modulus, which in turn causes changes in the phase velocity within the produced fluid, should have an effect on the frequencies of interest and the propagation of sound within the fluid.

REFERENCES

Biot M. A. 1956. Theory of Propagation of Elastic Waves in a Fluid-Saturated Porous Solid. I. Low-Frequency Range. The Journal of the Acoustical Society of America 1956 28:2, 168-178

Biot M. A. 1956. Theory of Propagation of Elastic Waves in a Fluid-Saturated Porous Solid. II. High-Frequency Range. The Journal of the Acoustical Society of America 1956 28:2, 179-191

Champoux Y., Allard J. F. 1991. Dynamic Tortuosity and Bulk Modulus in Air-Saturated Porous Media. Journal of Applied Physics 1991 70:4, 1975-1979

Chen, K. 2015. Acoustic Behavior of Flow from Fracture to Wellbore. Masters thesis. Texas A&M University

Hill, A. D. 1990. Noise Logging. In Production Logging: theoretical and interpretive elements, Vol. 14, Chap. 10, 112-120. Society of Petroleum Engineers: Henry L. Doherty Series

Johnson, D., Koplik, J., & Dashen, R. 1987. Theory of dynamic permeability and tortuosity in fluid-saturated porous media. Journal of Fluid Mechanics, 176, 379-402

Kinsler, L., Frey, A., Coppens, A., and Sanders, J. 2000. Fundamentals of Vibration, In Fundamentals of Acoustics, fourth Edition, New York: Wiley

Martinez, M., Bussières, J., Debruyne, D.,Lava, P. 2013. Load monitoring using a Rayleigh backscattering fibre optic system. International Conference of Adaptive Structure and Technologies, At Aruba

Martinez, R. 2014. Diagnosis of Fracture Flow Conditions with Acoustic Sensing. Masters thesis. Texas A&M University

Martinez, R., Chen, K., Santos, R., Hill, A. D., and Zhu, D. 2014a. Laboratory Investigation Acoustic Behavior for Flow from Fracture to a Wellbore. Presented at the SPE Annual Technical Conference and Exhibition, Amsterdam, Netherlands, 27-29 October. SPE-170788-MS

Martinez, R., Hill, A. D., and Zhu, D. 2014b. Diagnosis of Fracture Flow Condition with Acoustic Sensing. Presented at the SPE Hydraulic Fracturing Technology Conference, Woodlands, Texas, 4-6 February. SPE-168601-MS

McKinley, R. M. and Bower, F. M. 1977. Specialized Applications of Noise Logging. Presented at the SPE AIME 52nd Annual Fall Meeting, Denver, Colorado, 9-12 October. SPE-6784

McKinley, R. M., Bower, F. M., and Rumble, R. C. 1973. The Structure and Interpretation of Noise from Flow behind Cemented Casing. Presented at the SPE AIME 47th Annual Fall Meeting, San Antonio, Texas, 8-11 October. SPE-3999.

Molenaar, M. M. and Cox, B. E. 2013. Field Cases of Hydraulic Fracture Stimulation Diagnostics Using Fiber Optic Distributed Acoustic Sensing (DAS) Measurements and Analyses. Presented at the SPE Middle East Unconventional Gas Conference and Exhibition, Muscat, Oman, 28-30 January. SPE-164030-MS. 107

Molenaar, M. M., Hill, D. J., Webster, P., Fidan, E., and Birch, B. 2011. First Downhole Application of Distributed Acoustic Sensing (DAS) for Hydraulic Monitoring and Diagnostics. Presented at the SPE Hydraulic Fracturing Technology Conference and Exhibition, Woodlands, Texas, 24-26 January. SPE-140561-MS

Ouyang, L. 2013. Theoretical and Numerical Simulations of Non-Newtonian Fluid. Phd dissertation. Texas A&M University

Strang, G. 2007. Computational Science and Engineering. Wellesley, Ma. Wellesley-Cambridge Press

APPENDIX A

MATLAB ANALYSIS PACKET

Matlab Script and Functions Script “run.m” contains file name formatting to pull the desired sensor data, run an evaluation function on the desired data set to output SPL, spectral data, peak information, a spectrogram, and band powers, then write all aforementioned date to an excel sheet for report creation. “Eval.m” contains scripts to calculate band powers for various frequency bands (in this case octaves and 1/3 octaves starting from 1 KHz), SPL from FFT, SPL from a pwelch function, spectrum outputs from either FFT or welch power function:

Run.m script:

```
clear all;
runnumber=({'01','02','03','04','05','06'});
filename='f:\distributed_run_data\nov_15_17\&\&nov152017_%psi_ch1.csv';
h=1;
filename=strrep(filename,'&',runnumber(h,:));
runnumberfigureoutput=char(runnumber');
filenameiteration=1;
pressurevalues=char({'010'; '020'; '030'; '040'; '050'; '060'; '070'; '080'; '090'; '100'});
peak_value_matrix=zeros(length(pressurevalues),5,length(runnumber));
while filenameiteration<=length(filename)
```

```
a=10:10:length(pressurevalues*10);
lowcutoff=1000; %in Hz
highcutoff=7000; %in Hz
n=1;
r=1;
z=2;
za=zeros(24,length(a)+1);
b=zeros(10,length(a)+1);
c=zeros(length(a),2);
c(:,1)=a';
d=zeros(length(a),2);
d(:,1)=a';
exceloutput=runnumber(1,filenameiteration);

while n<=length(pressurevalues)

   s=strrep(filename(1,filenameiteration),'%',pressurevalues(n,:));
   s=num2str(cell2mat(s));
   [thirdoctavepowerband, octavepowerband, spl, f, pxx,
spl_fft]=evaluationbeta(s,lowcutoff,highcutoff);
   if n<2
```

```
        za(:,1)=thirdoctavepowerband(:,1);
        b(:,1)=octavepowerband(:,1);
    end


    c(r,2)=spl;
    d(r,2)=spl_fft;
    r=r+1;


    za(:,z)=thirdoctavepowerband(:,2);
    b(:,z)=octavepowerband(:,2);
    z=z+1;
%       figure('Visible','off');
%       plot(f,pxx);
%       xlabel('Frequency Hz')
%       ylabel('Pa^2/Hz')
%
saveas(gcf,sprintf('FIG%s%s.jpg',runnumberfigureoutput(filenameiteration,:),pressureva
lues(n,:)),'jpeg');


%     [p,locs,w,prom]=findpeaks(pxx,f);
%     p=p';
%     locs=locs';
```

```
%     w=w';
%     prom=prom';
%     frequenciestranspose=f';
%     welchoutputtranspose=pxx';
%     [p,index]=max(p);
%     location=locs(index,1);
%     width=w(index,1);
%     prominence=prom(index,1);
%     sound_pressure_level_peak=10*log10(p/(2*10^-5)^2);
%     peak_value_matrix(n,2,filenameiteration)=p;
%     peak_value_matrix(n,1,filenameiteration)=location;
%     peak_value_matrix(n,3,filenameiteration)=width;
%     peak_value_matrix(n,4,filenameiteration)=prominence;
%     peak_value_matrix(n,5,filenameiteration)=sound_pressure_level_peak;
%     frequencies(1,n)=num2cell(frequenciestranspose);
%     welchoutput(1,n)=num2cell(welchoutputtranspose);
%     peakvalue{1,n}=num2cell(p);
%     locations{1,n}=num2cell(locs);
%     widths{1,n}=num2cell(w);
%     prominence{1,n}=num2cell(prom);
   n=n+1 ;
end
```

```
outputfilename=strrep('e:\evaluationsheetbeta\4070_new_screen_nov15_outputsheet&.x
lsx','&',exceloutput);
outputfilename=num2str(cell2mat(outputfilename));
% outputmatlab=strrep('J:/evaluationsheetbeta/4070/outputsheet&.mat','&',exceloutput);
% outputmatlab=num2str(cell2mat(outputmatlab));

% save(outputmatlab,'peakvalue','locations','widths','prominence')
% xlswrite(outputfilename, za, 'thirdoctavebandpower', 'a1');
% xlswrite(outputfilename, b, 'octavebandpower', 'a1');
xlswrite(outputfilename, c, 'spl', 'a1');
xlswrite(outputfilename,d,'spl_fft','a1');
% xlswrite(outputfilename,peak_value_matrix,'peaks','a1');
filenameiteration=filenameiteration+1;
end
```

evaluationbeta.m function:

```
function [thirdoctavepowerband, octavepowerband, spl, f, pxx, spl_fft ] =
evaluationbeta( filename,lowfilter, highfilter )
%UNTITLED Summary of this function goes here
%   Detailed explanation goes here
filename=csvread(filename);
pressure=filename;
```

```
sampletime=10; %sec
fs=length(pressure)/sampletime;

% 1/3 octave band calculation%
centerfrequencyvalue=62.5;
n=1;
numberofiterations=round((-(log(centerfrequencyvalue/11314)/log(2)-(1/6))*3), 0);
thirdoctavepowerband=zeros(24,2);
while (n<24)
if (n<24)
   leftfrequencyvalue=centerfrequencyvalue/2^(1/6);
   rightfrequencyvalue=centerfrequencyvalue*2^(1/6);
   b=bandpower(pressure,fs,[leftfrequencyvalue rightfrequencyvalue]);
   thirdoctavepowerband(n,1)=centerfrequencyvalue;
   thirdoctavepowerband(n,2)=b;
   centerfrequencyvalue=centerfrequencyvalue*2^((1/3));
 n=n+1;
end
end
thirdoctavepowerband(n,1)=12;
leftfrequencytotalpowerband=(thirdoctavepowerband(1,1)*.5^(1/6));
rightfrequencytotalpowerband=thirdoctavepowerband(n-1,1)*2^(1/6);
```

```
c=bandpower(pressure,fs,[leftfrequencytotalpowerband rightfrequencytotalpowerband]);
thirdoctavepowerband(n,2)=c;
indexthirdoctave=24;
% octave band calculation%
centerfrequencyvalue=31.25;
numberofiterations=round(-(log(centerfrequencyvalue/11314)/log(2)-(1/2))+1, 0);
m=1;
octavepowerband=zeros(10,2);
while (m<10)
if (m<10)
   leftfrequencyvalue=centerfrequencyvalue/2^(1/2);
   rightfrequencyvalue=centerfrequencyvalue*2^(1/2);
   b=bandpower(pressure,fs,[leftfrequencyvalue rightfrequencyvalue]);
   octavepowerband(m,1)=centerfrequencyvalue;
   octavepowerband(m,2)=b;
   centerfrequencyvalue=centerfrequencyvalue*2;
m=m+1;
end
end
octavepowerband(m,1)=12;
leftfrequencytotalpowerband=octavepowerband(1,1)*.5^(1/2);
rightfrequencytotalpowerband=octavepowerband(m-1,1)*2^(1/2);
```

```
d=bandpower(pressure,fs,[leftfrequencytotalpowerband rightfrequencytotalpowerband]);
octavepowerband(m,2)=d;
indexoctave=10;



%increased HPF passes
y=length(pressure);
y=2^nextpow2(y);
nx=max(size(pressure));
na=16; %avging factor for pwelch
w=hanning(floor(nx/na));
[pxx,f]=pwelch(pressure,w,0,[lowfilter:highfilter],44100);
% spl=10*log10(rms(pxx)/(.00002)^2);
%
% fs=length(pressure)/10;
% time=(0:(1/fs):10-1/fs);%ASSUME 10 SECOND SAMPLE RUN
% time=time';
% y=length(pressure);
% y=2^nextpow2(y);
% low_frequency=1000*2/fs;
% high_frequency=7000*2/fs;
% %%%%%FILTER SECTION STILL WORKING ON THIS%%%%%%%%
```

```
% [B,A]=butter(2,[low_frequency high_frequency],'bandpass'); %this will work for
25.6khz sampling and 10 sec run time change accordingly
% [B,A]=butter(2,[0.1 .7],'bandpass');
% filteredpressure=filter(B,A, pressure);
% % % % [B,A]=butter(10,.7, 'low');
% % % % d=filter(B,A, d);
%
%
% pprime=fft(filteredpressure,y);
%
% frequency_incremenet=fs/y;
% f=fs*(0:(y/2))/y;
% f=fs/2*linspace(0,1,y/2+1);
% figure (3)
% plot(time,pressure, 'b')
% hold;
% plot(time, filteredpressure, 'g')
%
% NFFT=2^nextpow2(fs);
% H=fft(pressure, NFFT)/fs;
% f=fs/2*linspace(0,1,NFFT/2+1);
%
```

```
% p2=abs(pprime/y);
% p1= p2(1:y/2+1);
% p1(2:end-1) = 2*p1(2:end-1);
%
% db=pprime.*conj(pprime)/y;
%
% db=pprime;
% % figure(1)
% % % plot(f(1000:10000), dbunfiltered(1000:10000), 'b')
% % % hold;
%
%
% % % % % % % % % %
% figure(2)
% plot(f, p1);
% % % % % % % % % %
%
% plot(f(500:5000), -20*log(abs(pprime(500:5000))./(2*10^-5));
%
% rmsnumb=rms(db);
% spl_fft= 10 * log10(rmsnumb/(.00002)^2);
spl=1;
```

```
spl_fft=1;
end
```

APPENDIX B

EXPERIMENT SPECTRAL POWER DENSITY PLOTS

To retain clarity in the results section a sample work flow was performed and all of spectral data was withheld. This appendix contains the spectrums extracted by Power Welch function of the different proppant pack flow experiments. Spectrograms are appended in order of run (10 PSIG increments starting from 10 PSIG).

Empty Cell

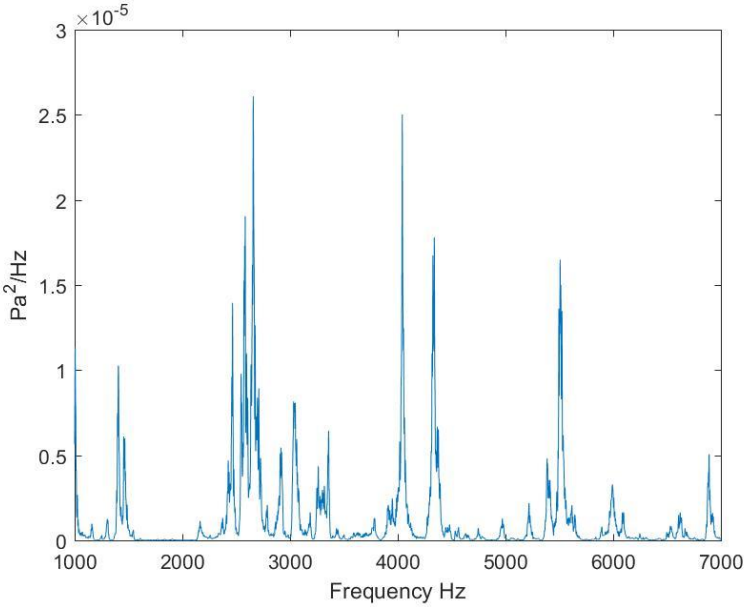

Figure 43: Empty Cell 10 PSIG

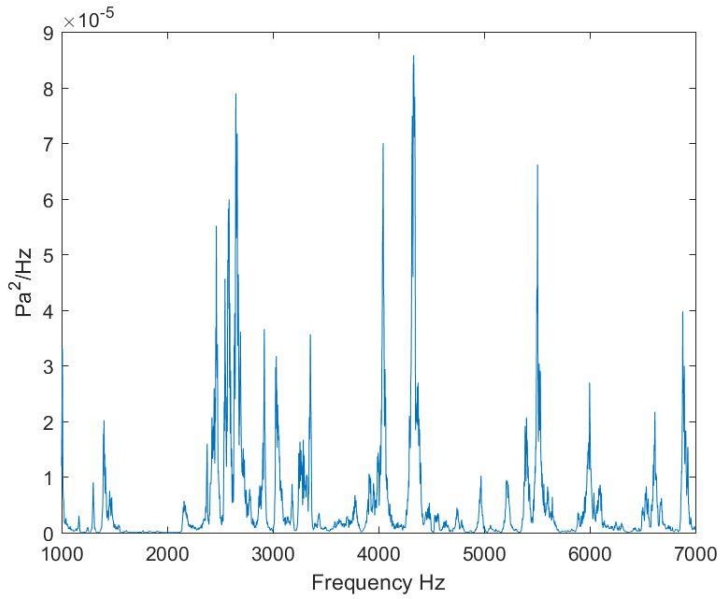

Figure 44: Empty Cell 20 PSIG

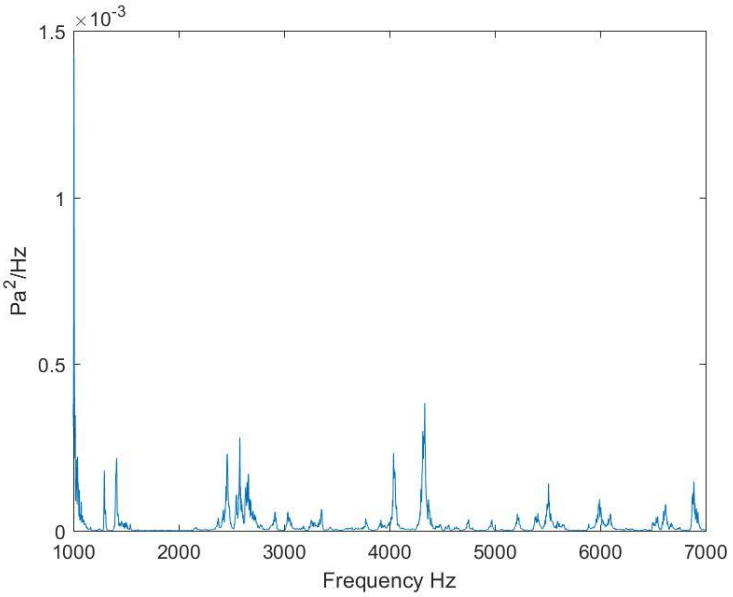

Figure 45: Empty Cell 30 PSIG

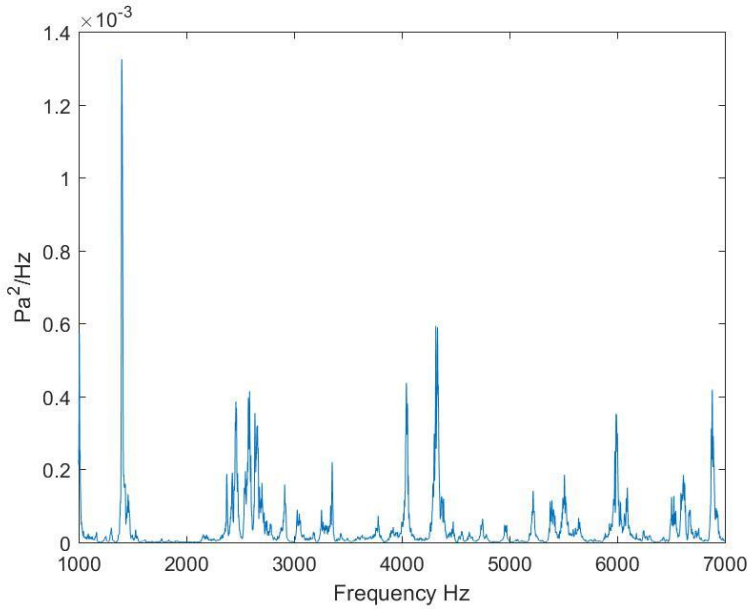

Figure 46: Empty Cell 40 PSIG

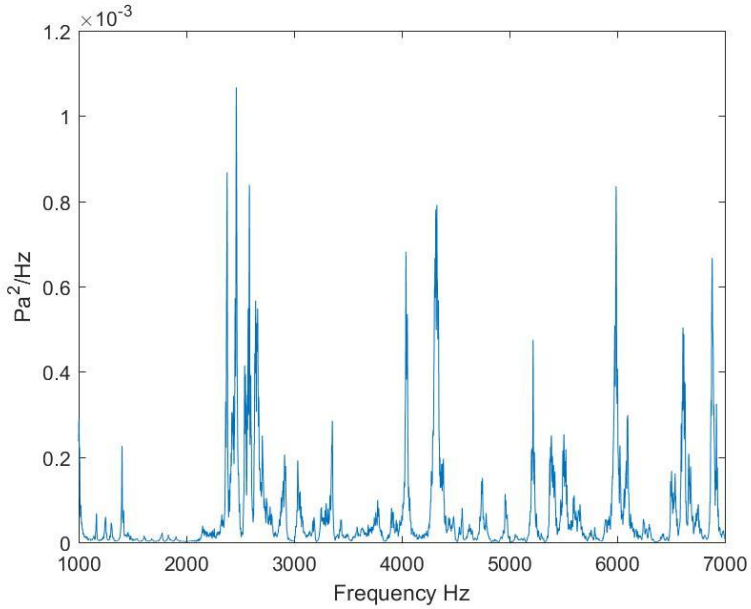

Figure 47: Empty Cell 50 PSIG

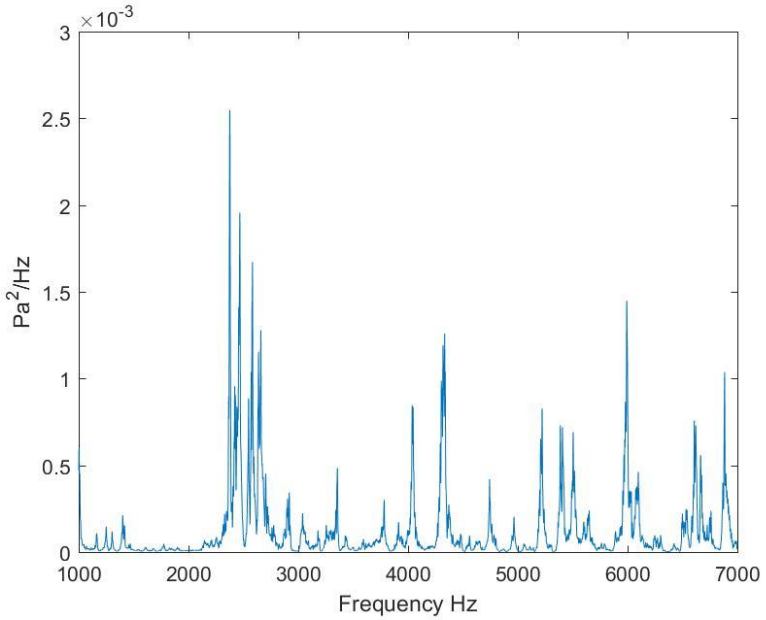

Figure 48: Empty Cell 60 PSIG

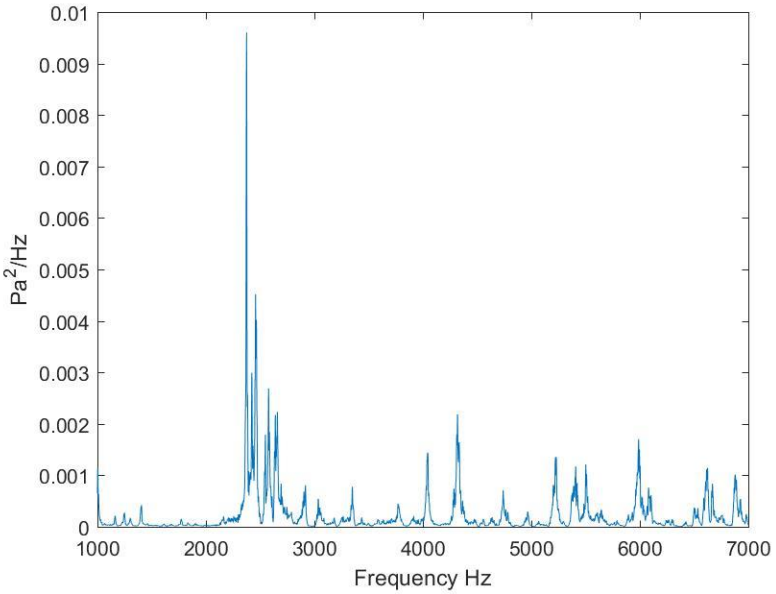

Figure 49: Empty Cell 70 PSIG

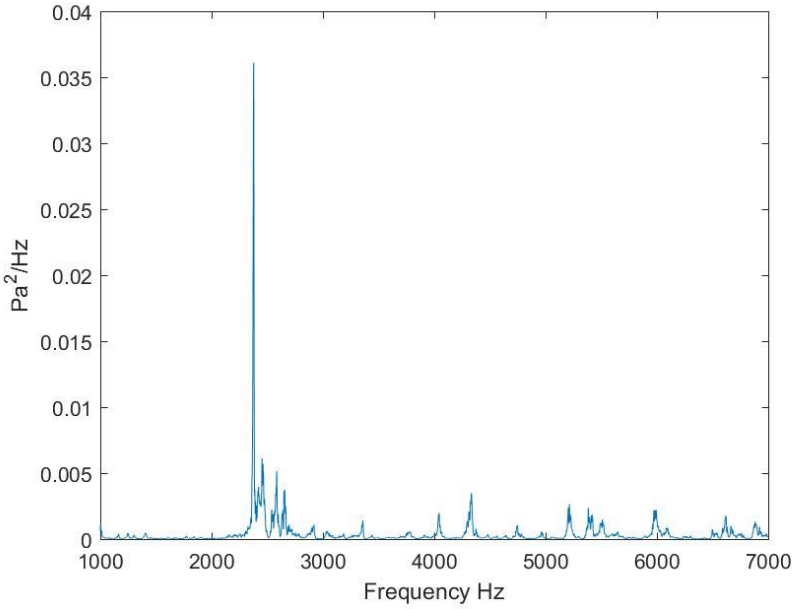

Figure 50: Empty Cell 80 PSIG

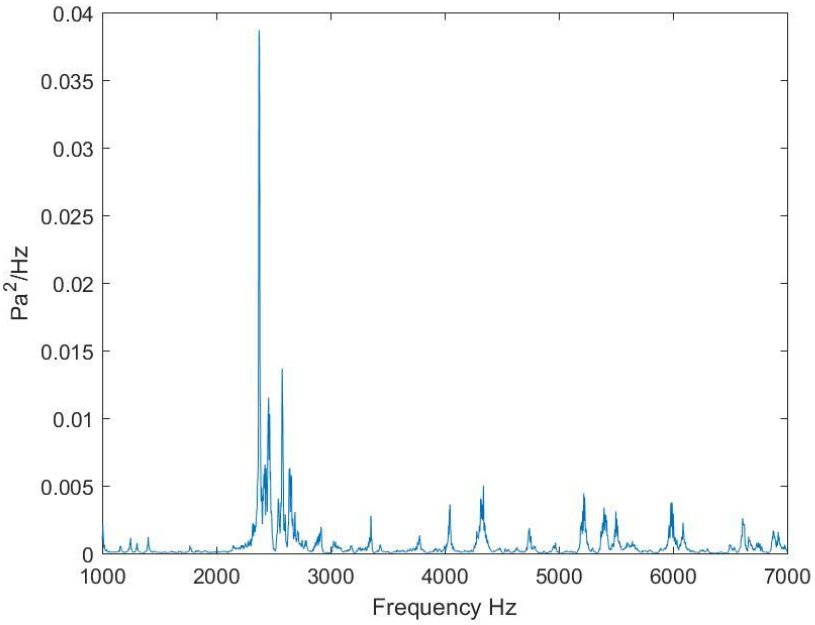

Figure 51: Empty Cell 90 PSIG

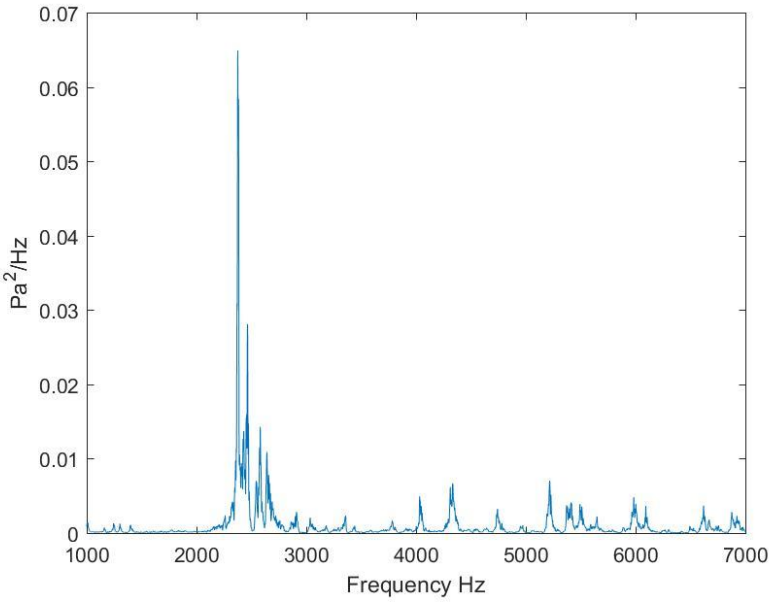

Figure 52: Empty Cell 100 PSIG

16/30 Mesh

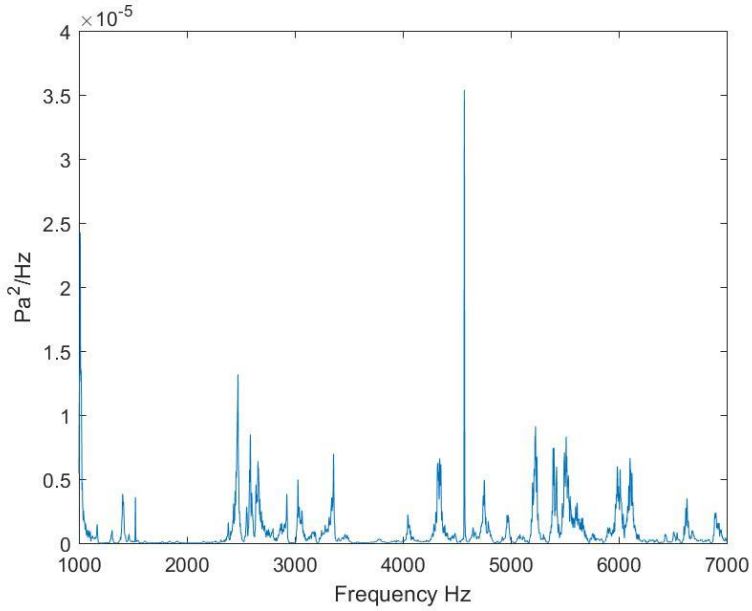

Figure 53: 16/30 Mesh 10 PSIG

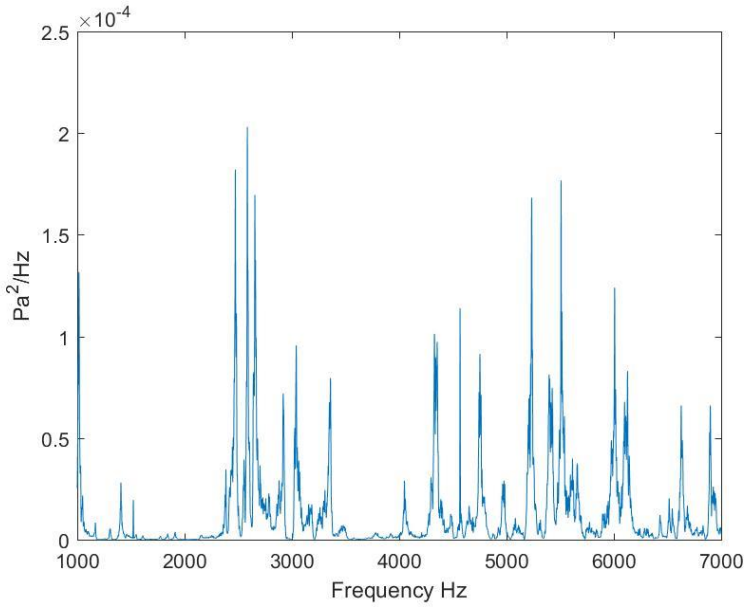

Figure 54: 16/30 Mesh 20 PSIG

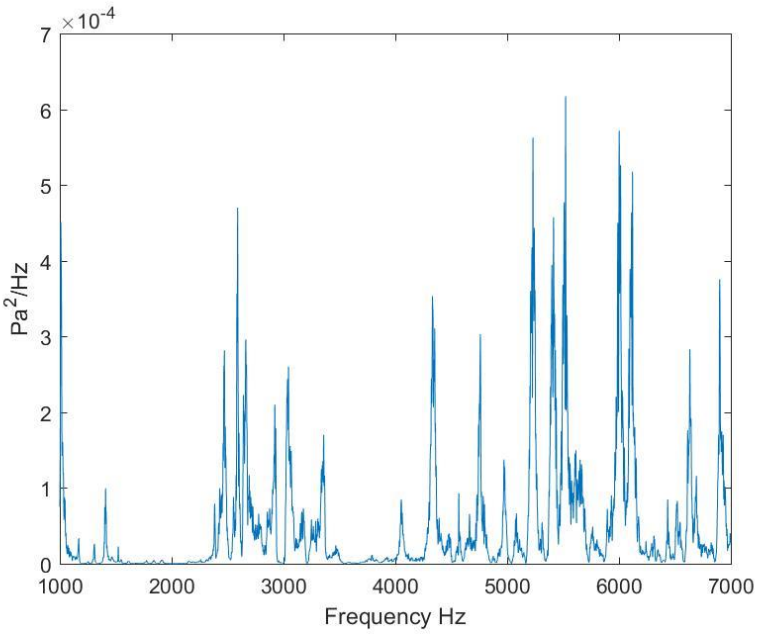

Figure 55: 16/30 Mesh 30 PSIG

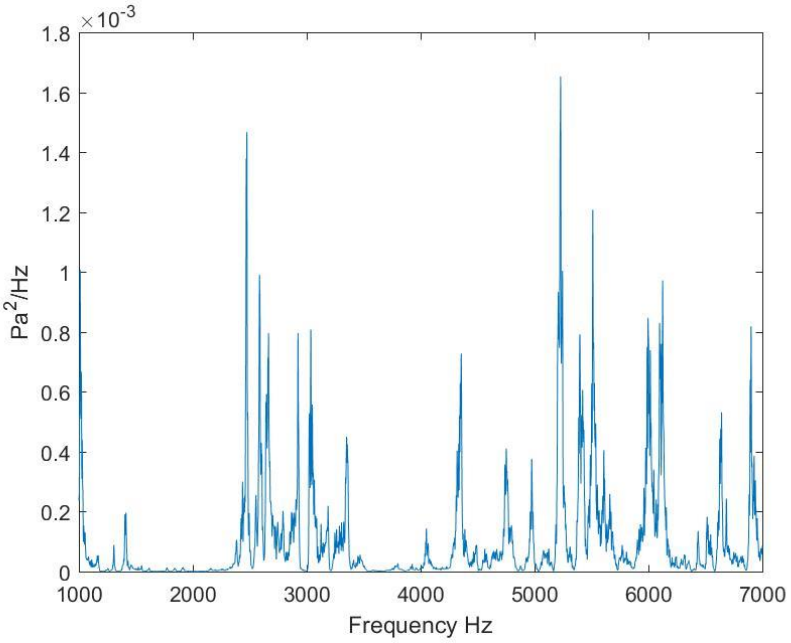

Figure 56: 16/30 Mesh 40 PSIG

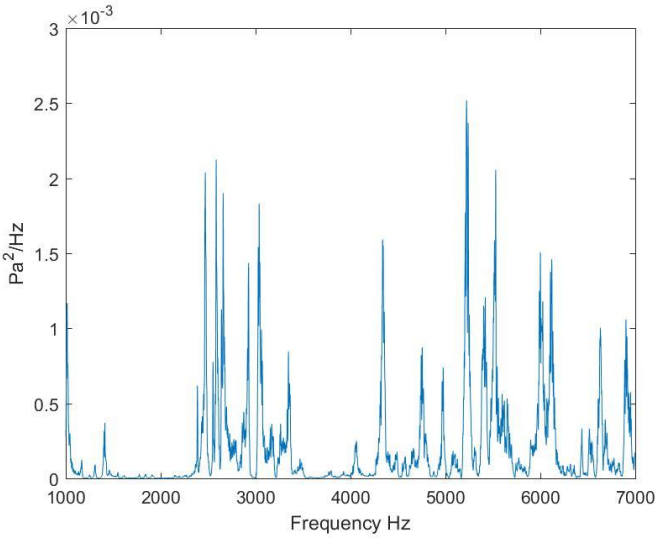

Figure 57: 16/30 Mesh 50 PSIG

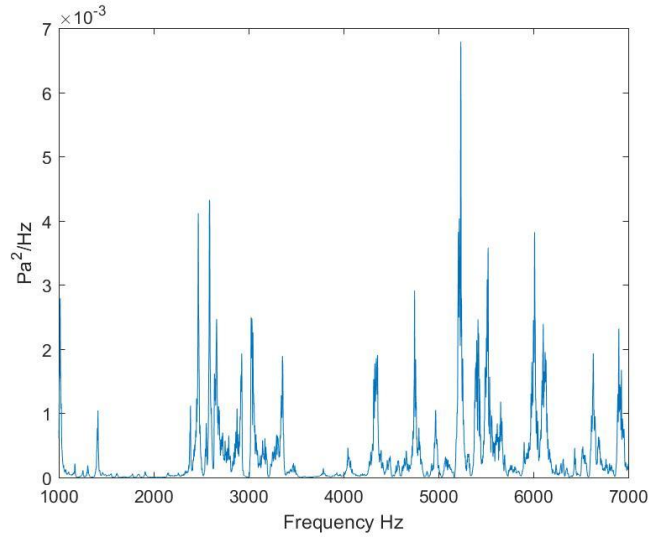

Figure 58: 16/30 Mesh 60 PSIG

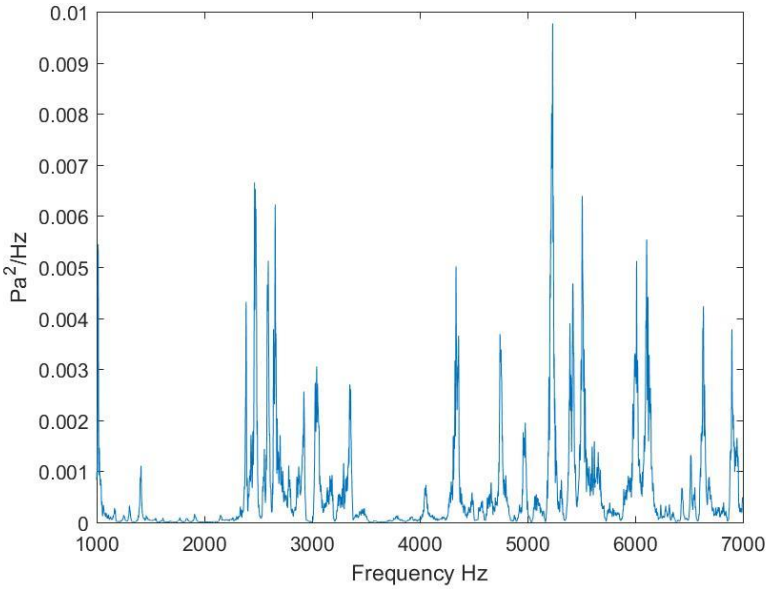

Figure 59: 16/30 Mesh 70 PSIG

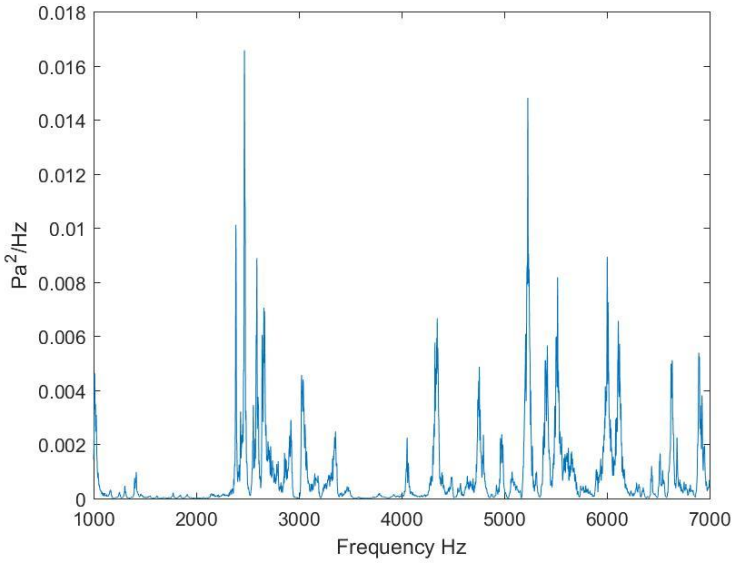

Figure 60: 16/30 Mesh 80 PSIG

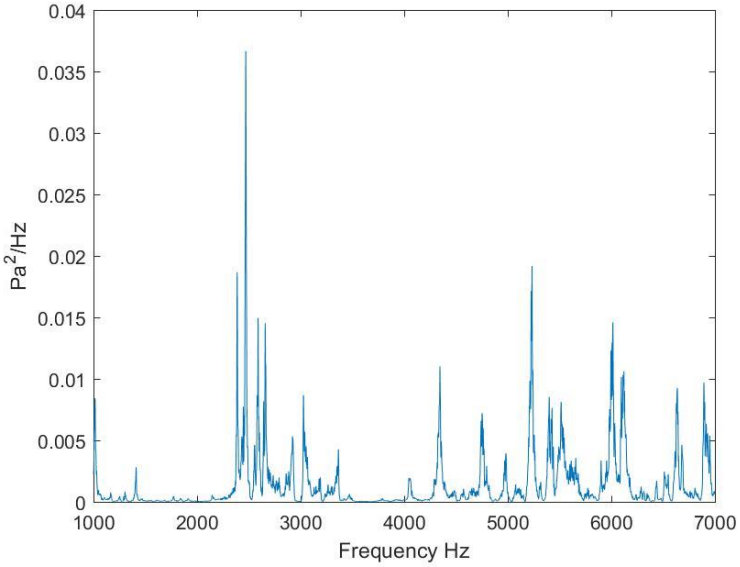

Figure 61: 16/30 Mesh 90 PSIG

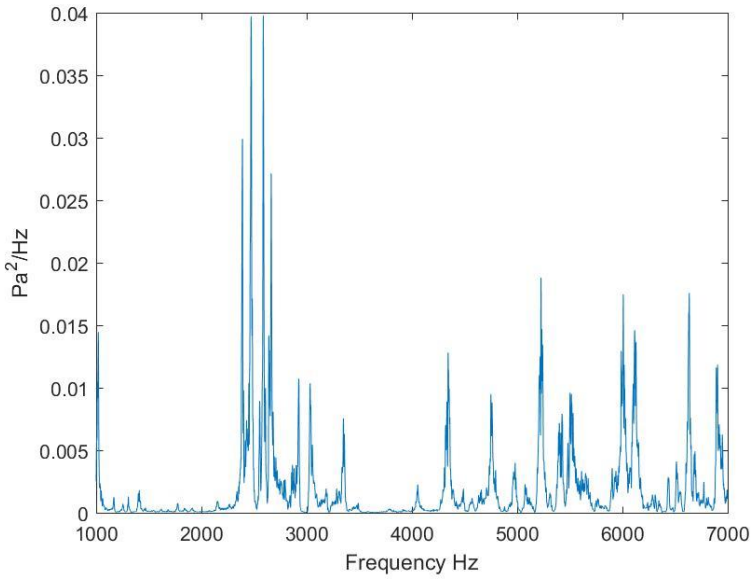

Figure 62:16/30 Mesh 100 PSIG

20/40 Mesh

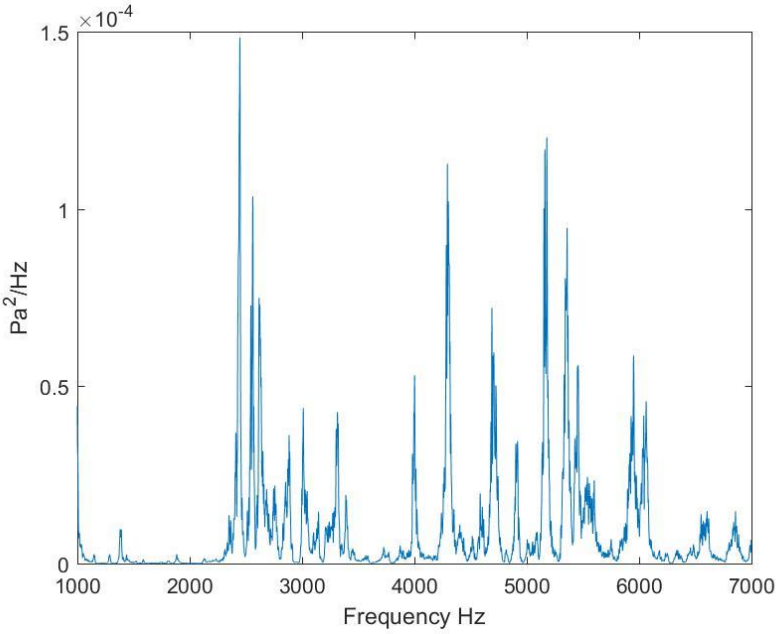

Figure 63: 20/40 Mesh 10 PSIG

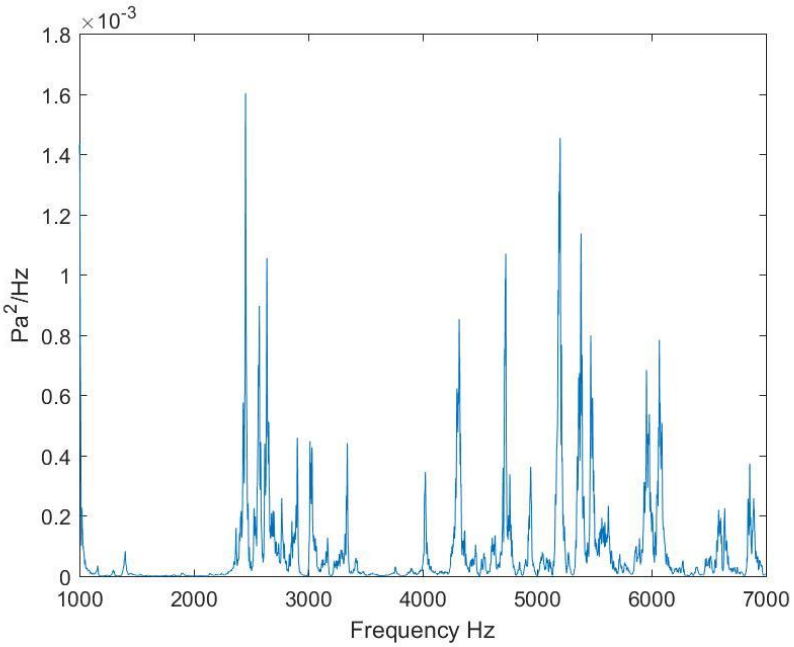

Figure 64: 20/40 Mesh 20 PSIG

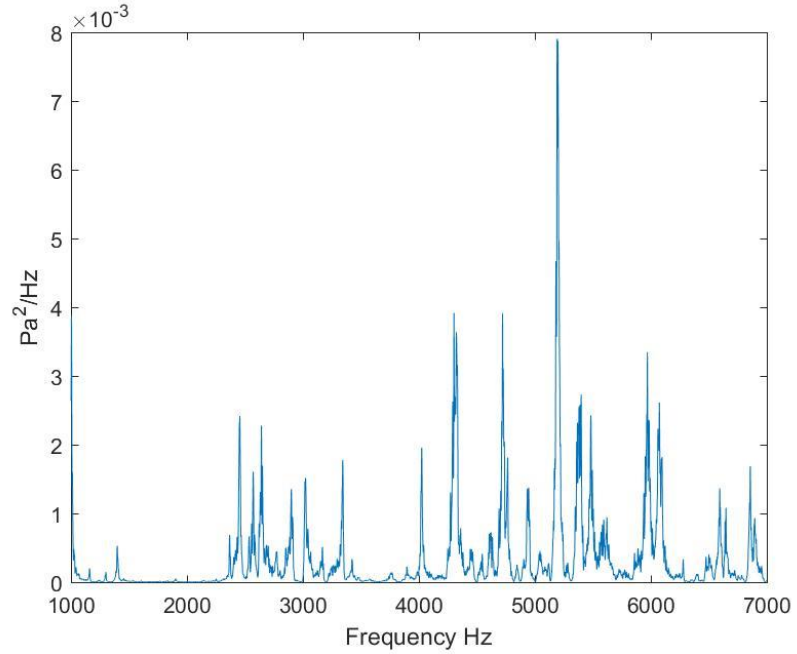

Figure 65: 20/40 Mesh 30 PSIG

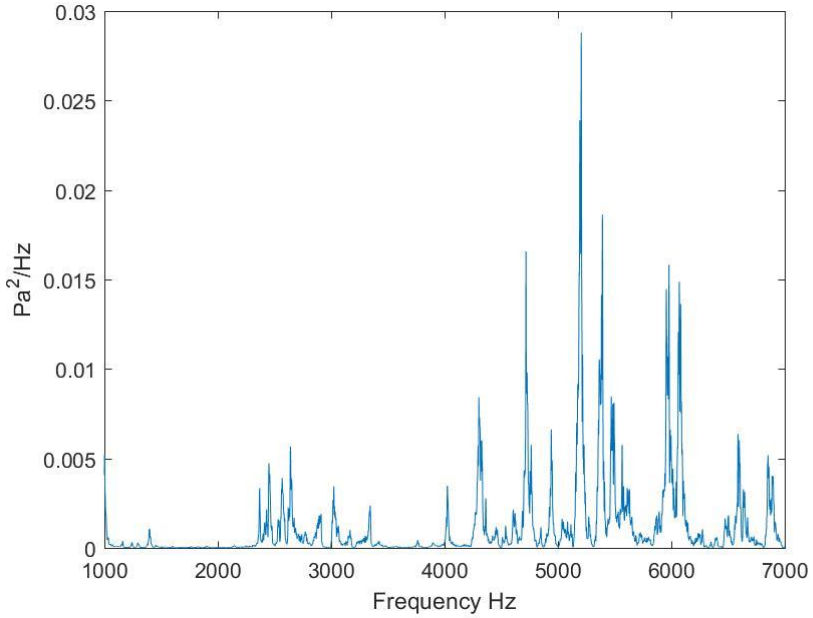

Figure 66: 20/40 Mesh 40 PSIG

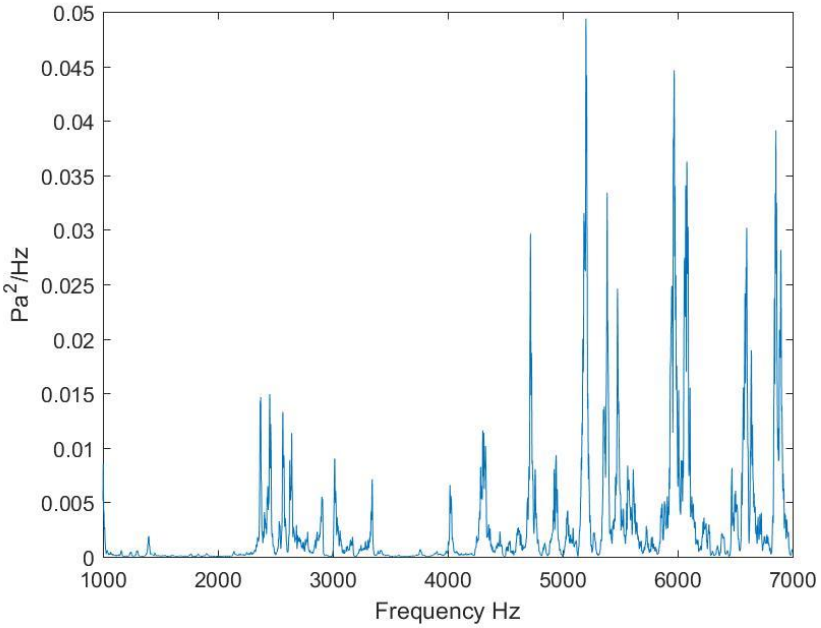

Figure 67: 20/40 Mesh 50 PSIG

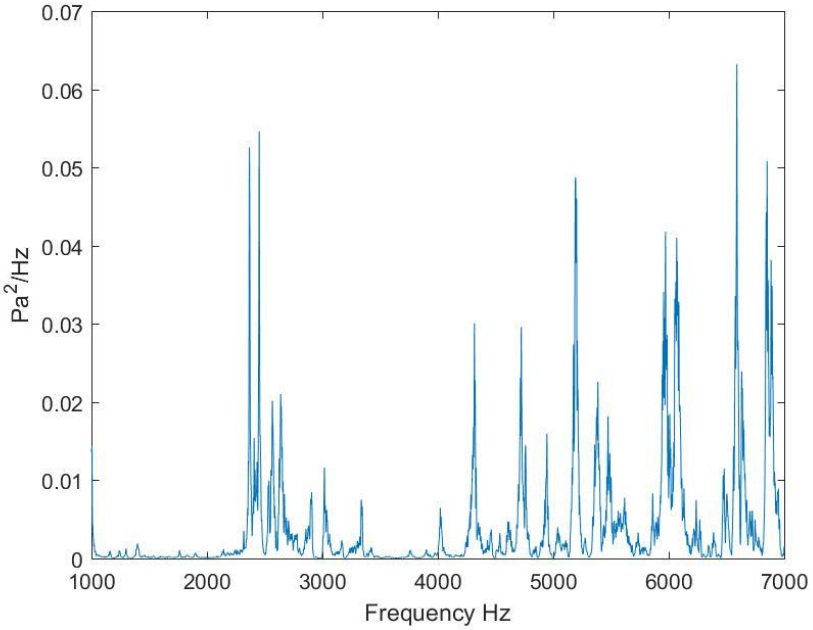

Figure 68:20/40 Mesh 60 PSIG

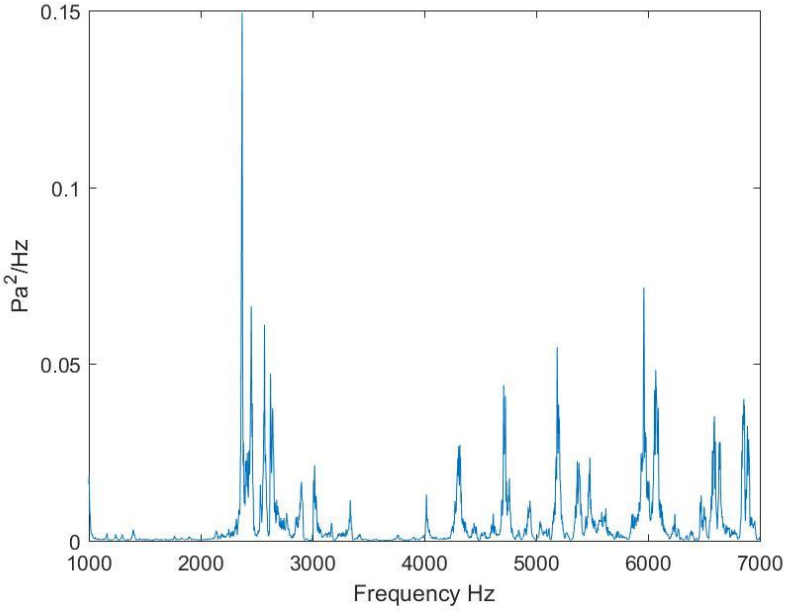

Figure 69: 20/40 Mesh 70 PSIG

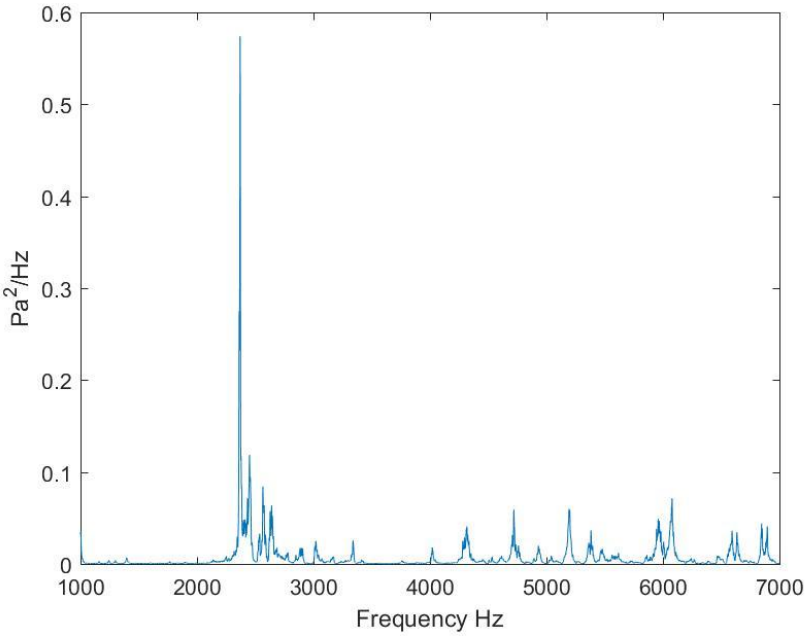

Figure 70: 20/40 Mesh 80 PSIG

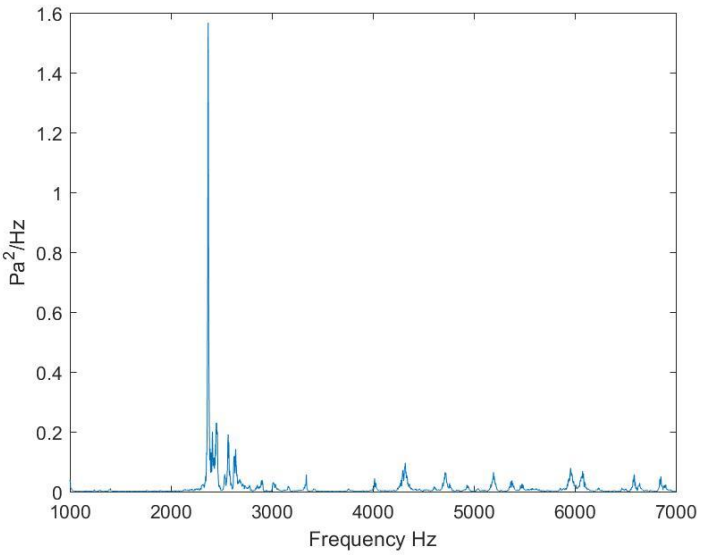

Figure 71: 20/40 Mesh 90 PSIG

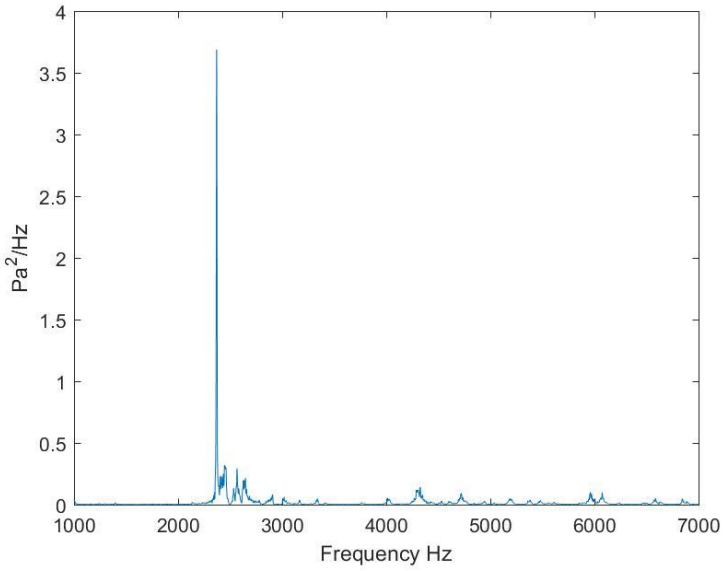

Figure 72: 20/40 Mesh 100 PSIG

30/50 Mesh

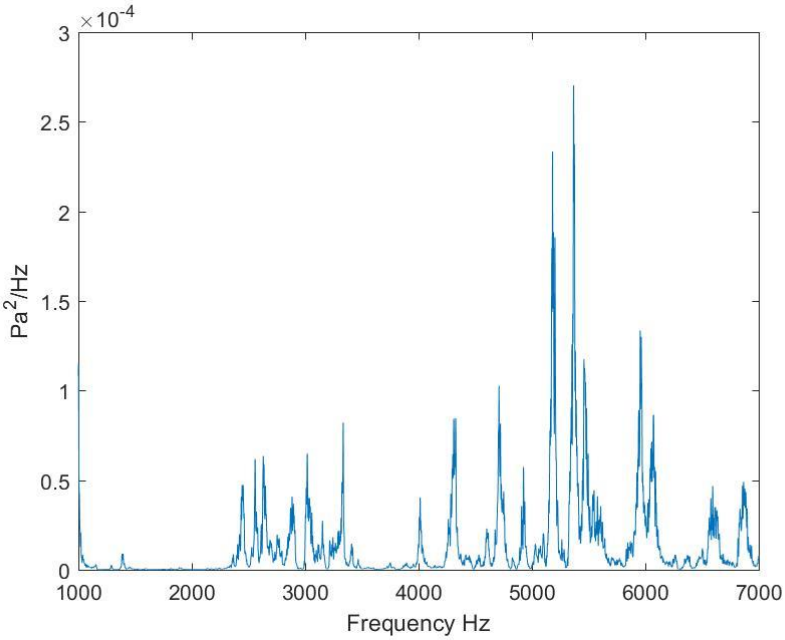

Figure 73: 30/50 Mesh 10 PSIG

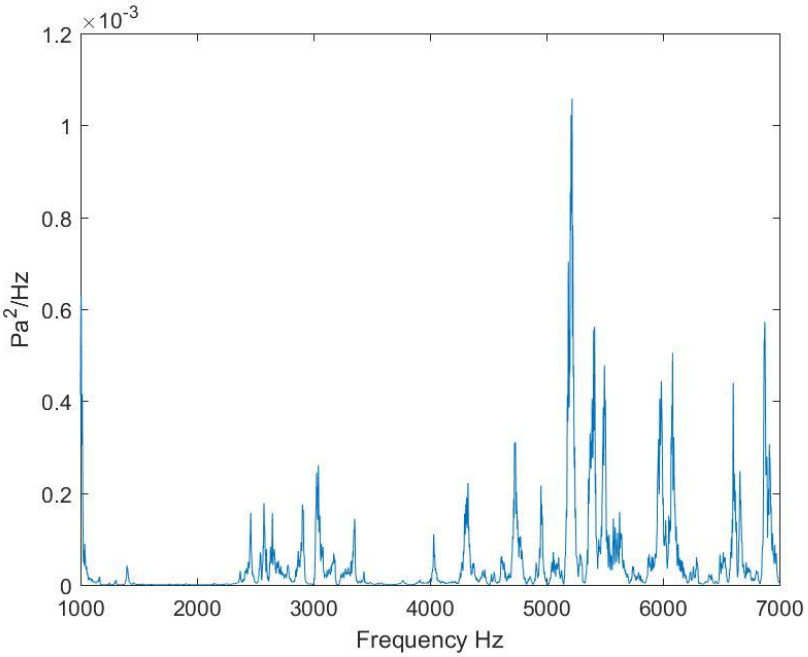

Figure 74: 30/50 Mesh 20 PSIG

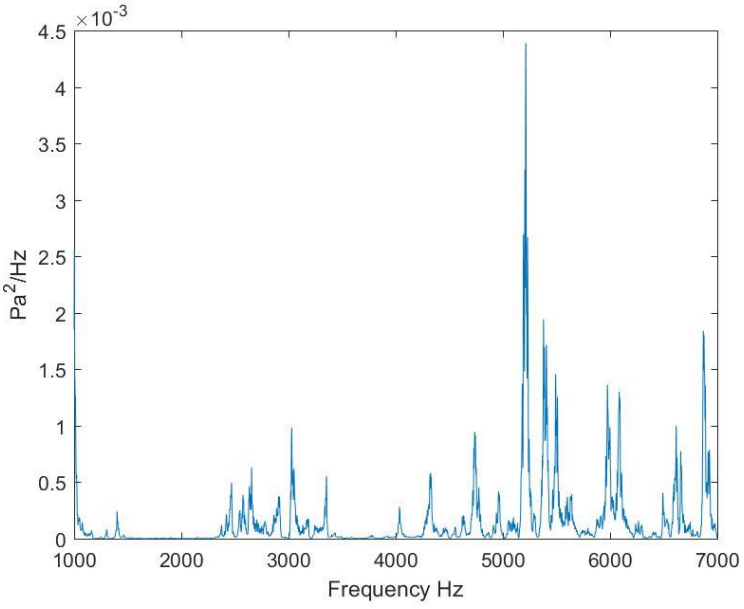

Figure 75: 30/50 Mesh 30 PSIG

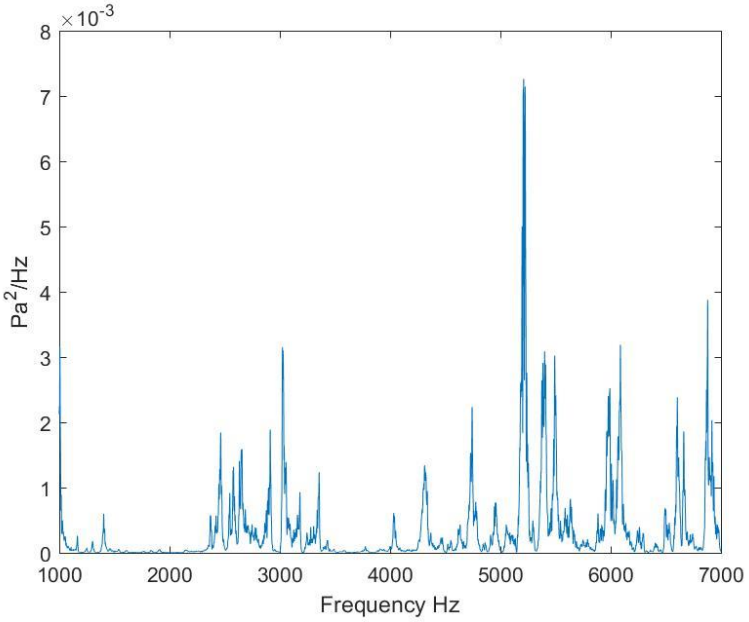

Figure 76: 30/50 Mesh 40 PSIG

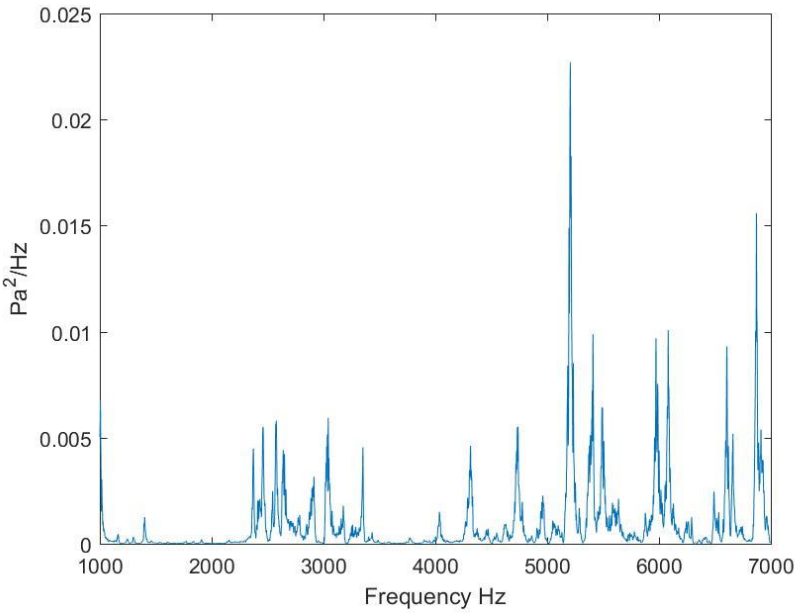

Figure 77: 30/50 Mesh 50 PSIG

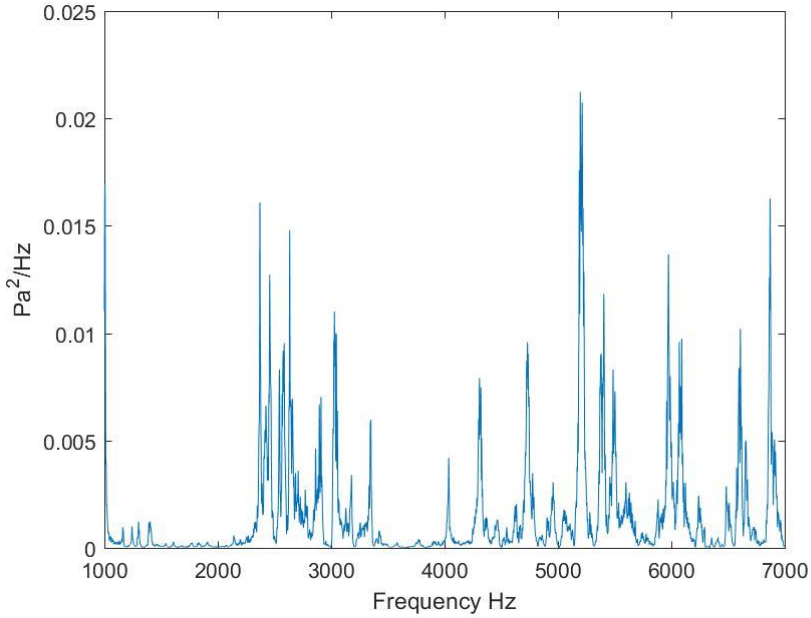

Figure 78: 30/50 Mesh 60 PSIG

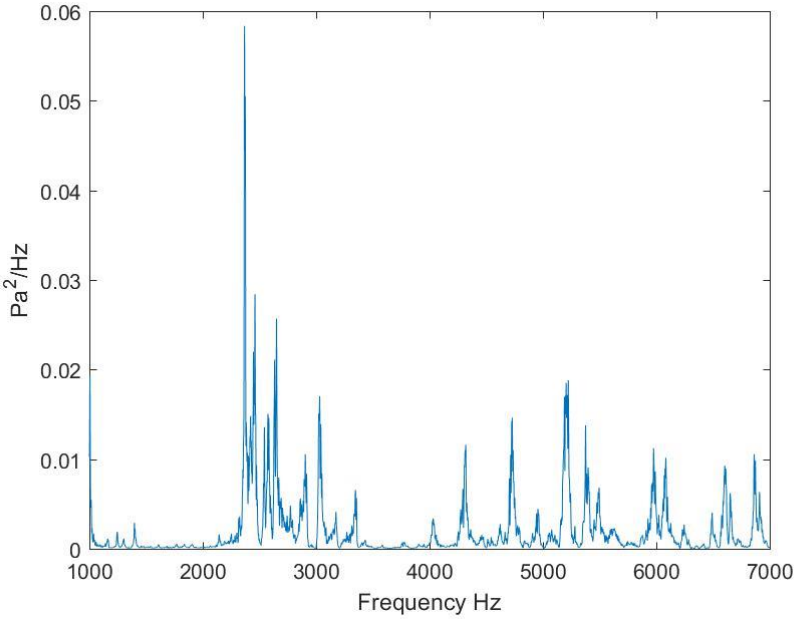

Figure 79: 30/50 Mesh 70 PSIG

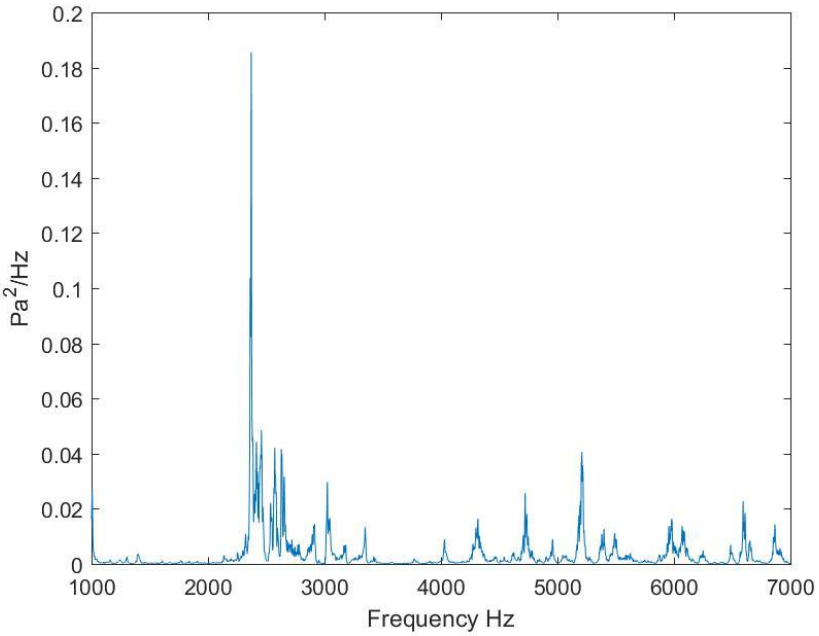

Figure 80:30/50 Mesh 80 PSIG

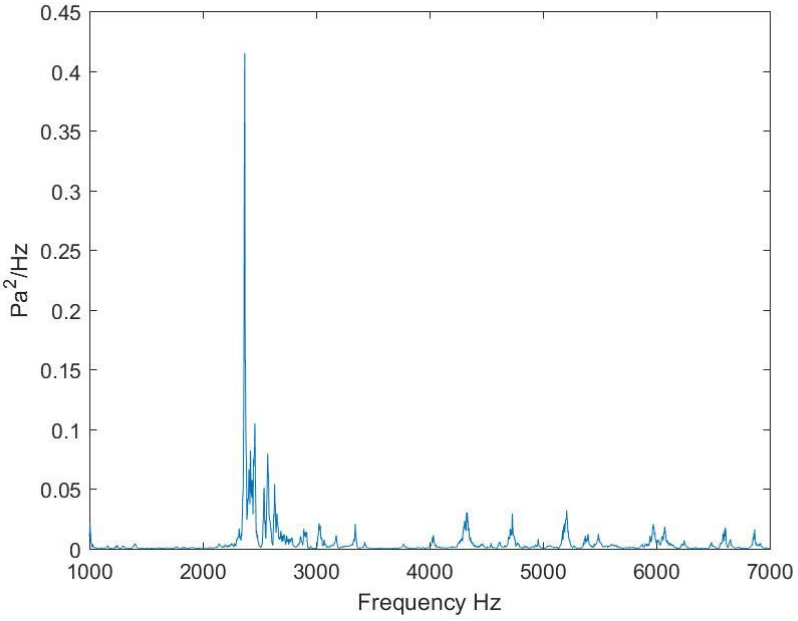

Figure 81:30/50 Mesh 90 PSIG

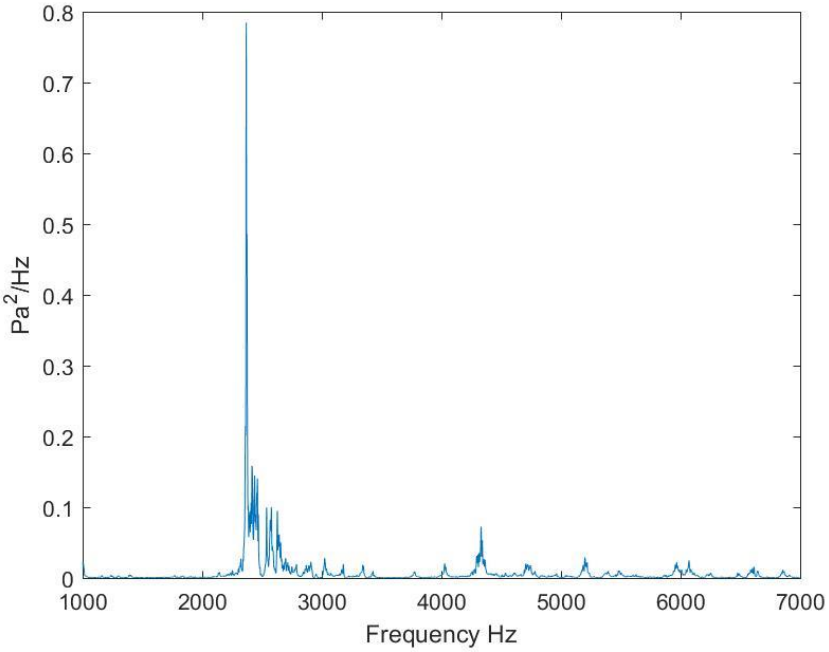

Figure 82: 30/50 Mesh 100 PSIG

16/30-30/50 Mixed

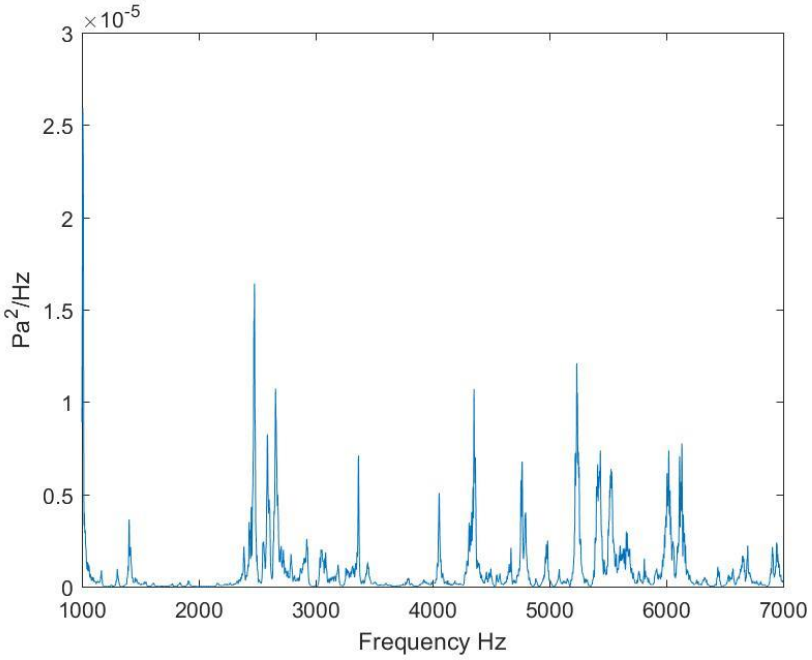

Figure 83: 16/30-30/50 Mixed 10 PSIG

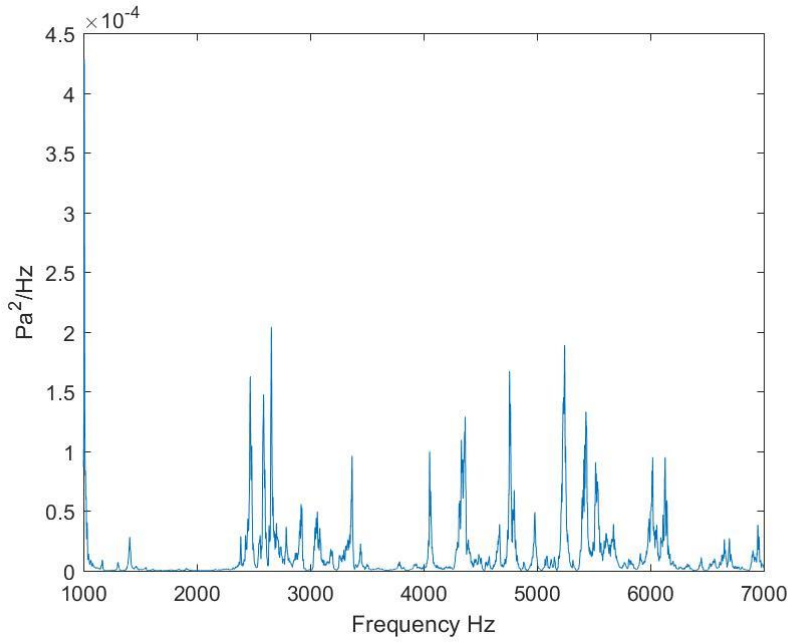

Figure 84: 16/30-30/50 Mixed 20 PSIG

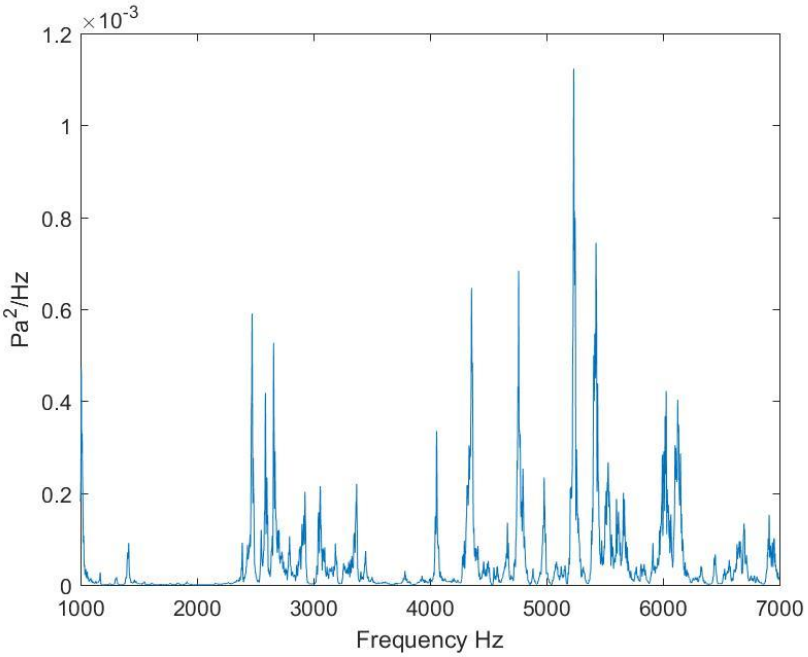

Figure 85: 16/30-30/50 Mixed 30 PSIG

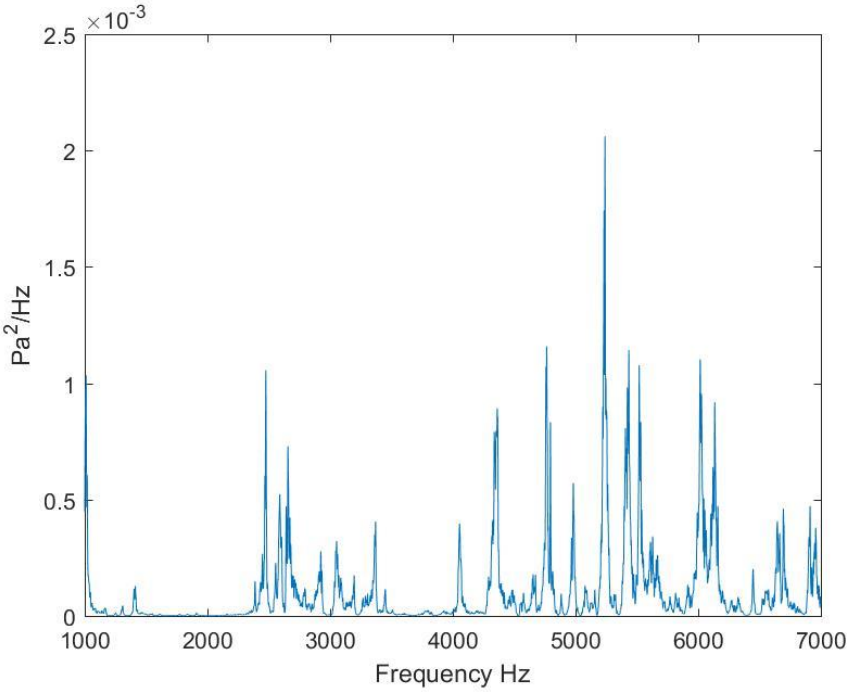

Figure 86: 16/30-30/50 Mixed 40 PSIG

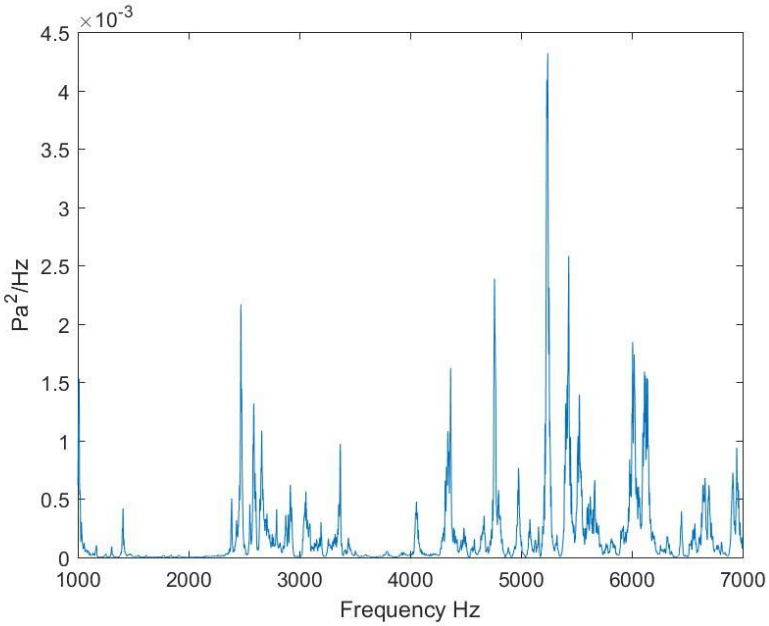

Figure 87: 16/30-30/50 Mixed 50 PSIG

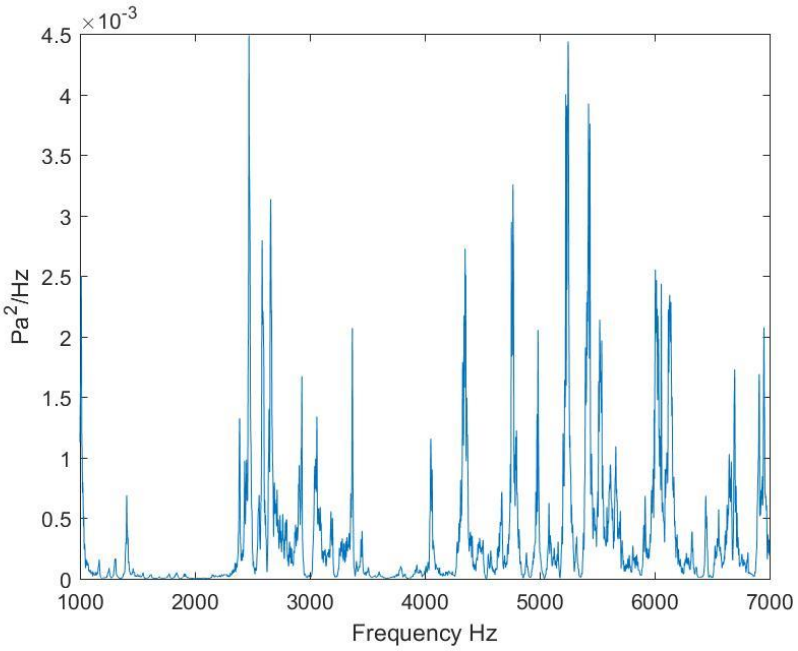

Figure 88: 16/30-30/50 Mixed 60 PSIG

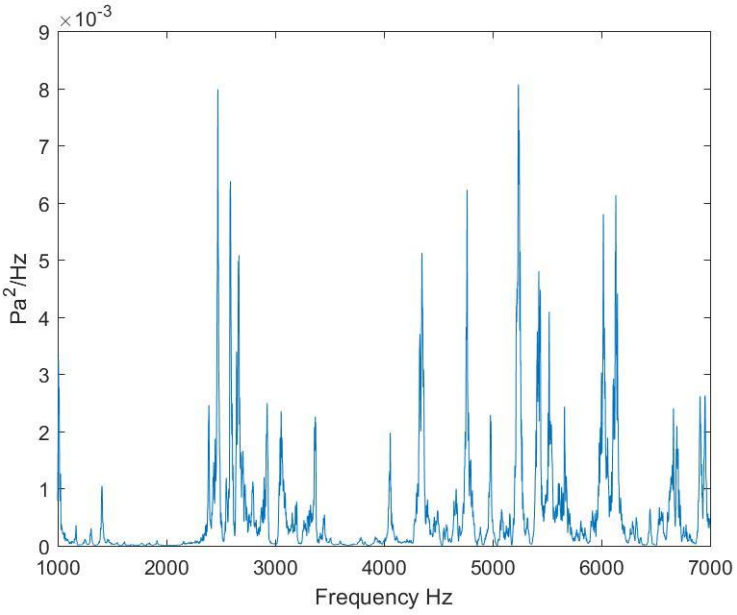

Figure 89: 16/30-30/50 Mixed 70 PSIG

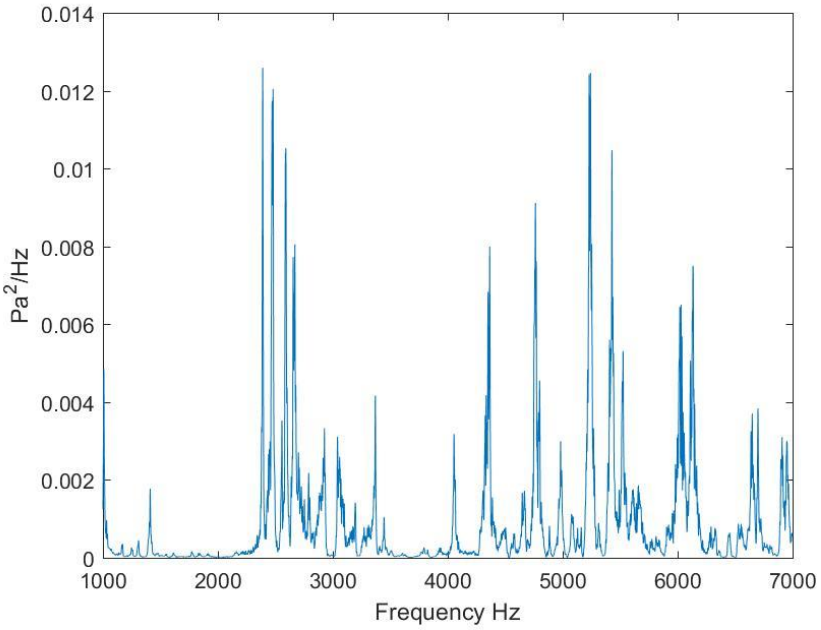

Figure 90: 16/30-30/50 Mixed 80 PSIG

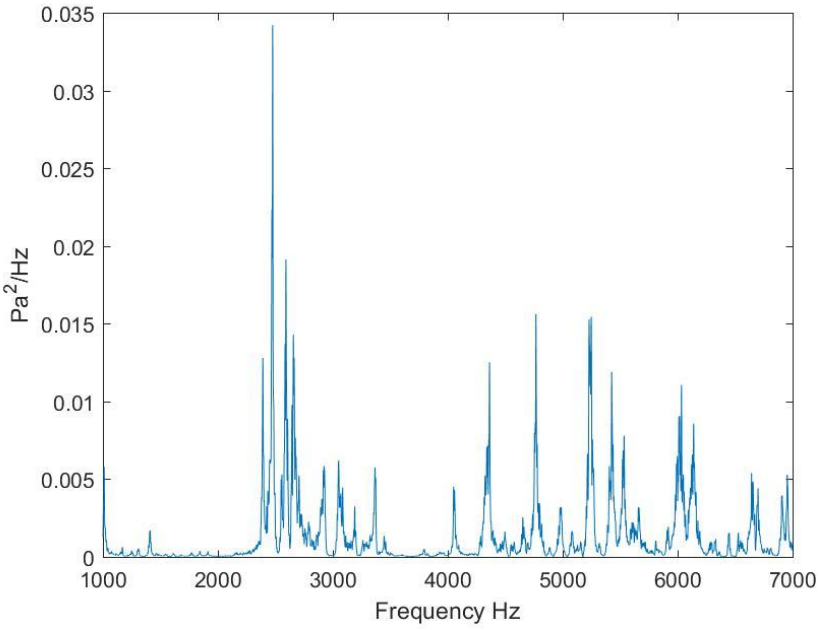

Figure 91: 16/30-30/50 Mixed 90 PSIG

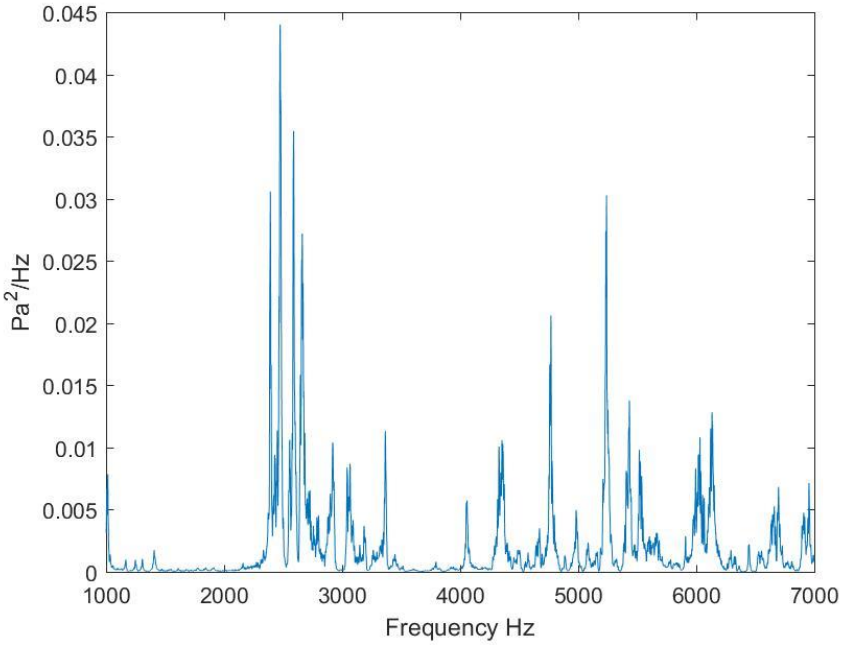

Figure 92: 16/30-30/50 Mixed 100 PSIG

20/40-30/50 Mixed

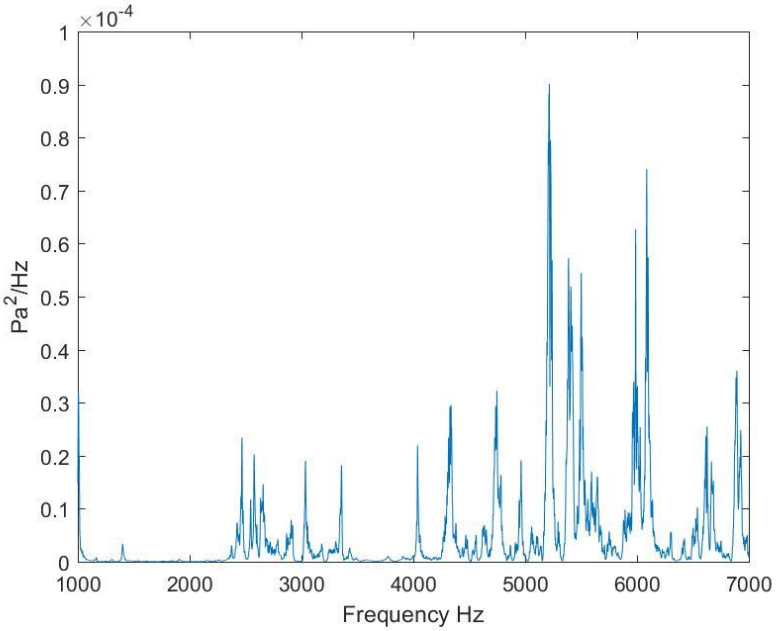

Figure 93: 20/40-30/50 Mixed 10 PSIG

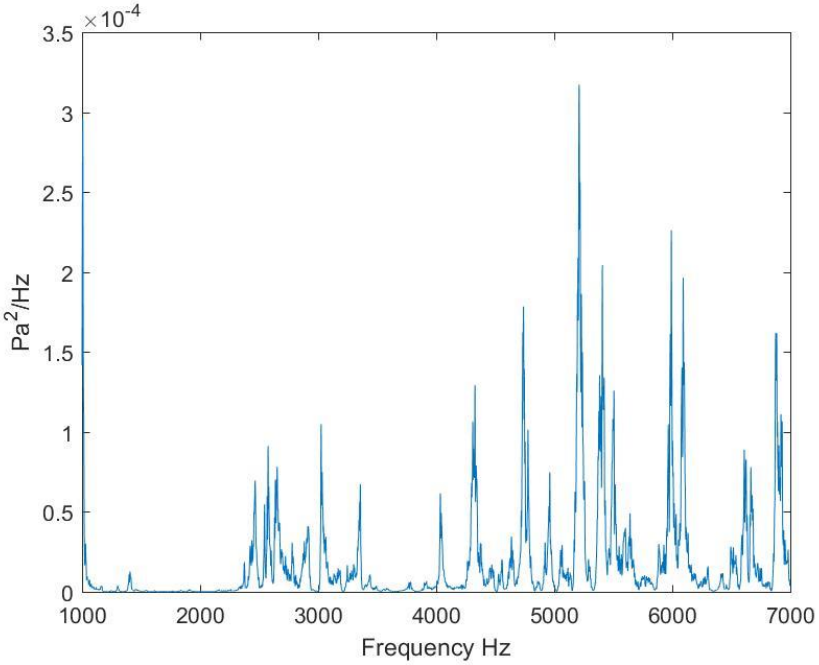

Figure 94: 20/40-30/50 Mixed 20 PSIG

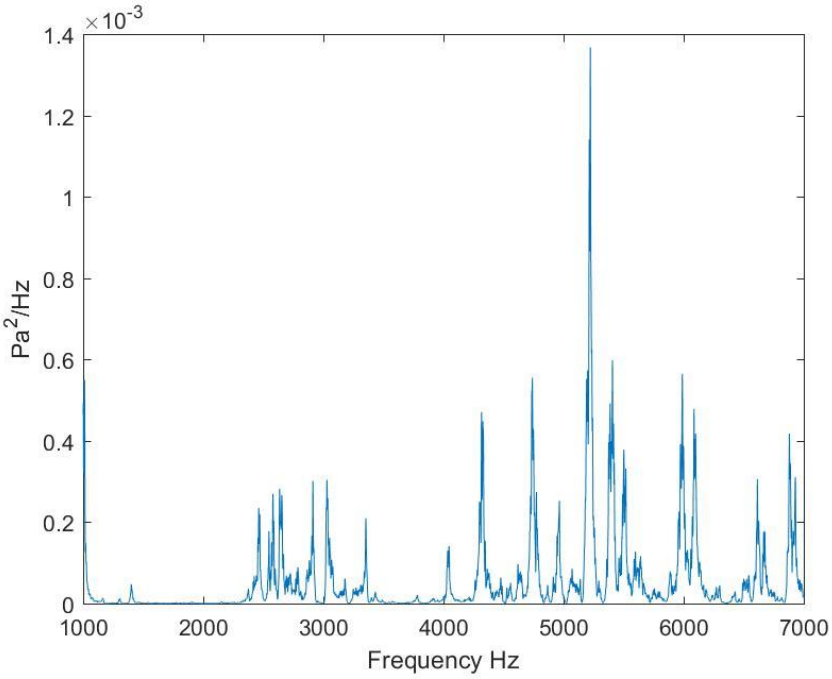

Figure 95: 20/40-30/50 Mixed 30 PSIG

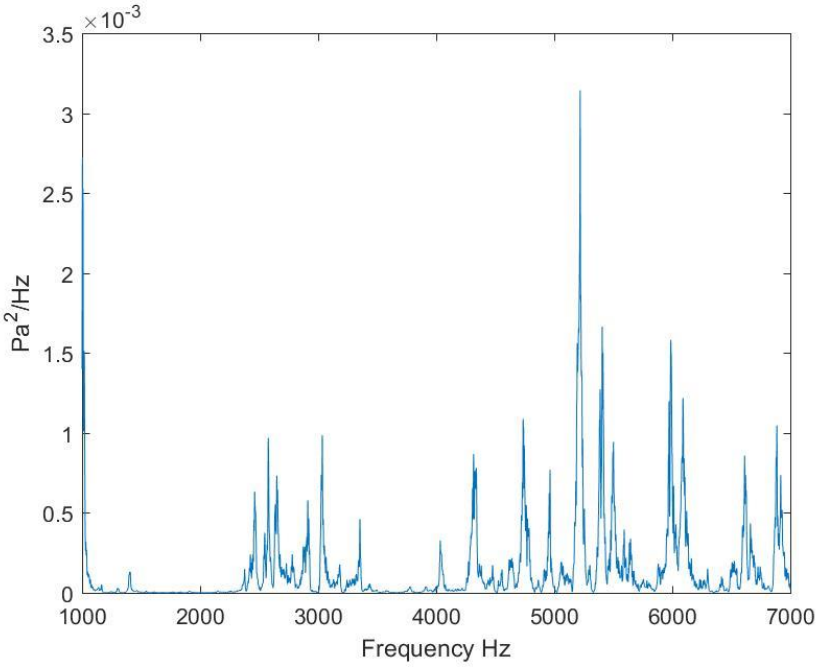

Figure 96: 20/40-30/50 Mixed 40 PSIG

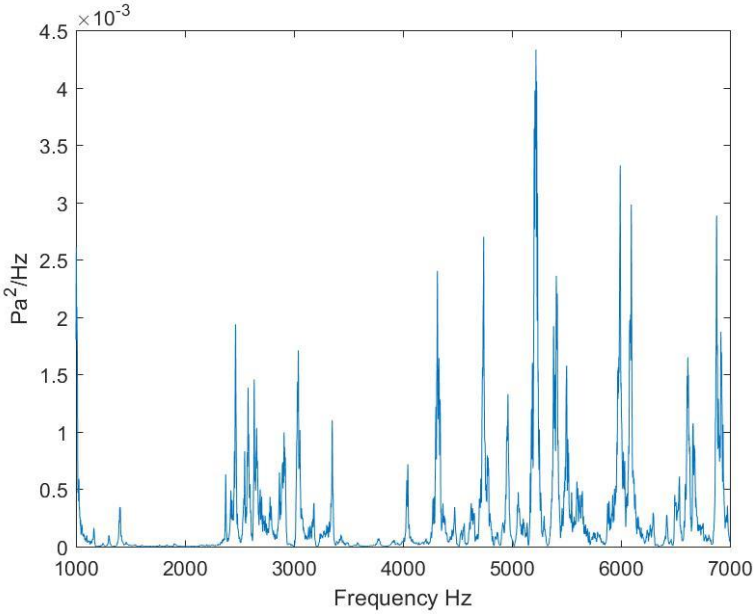

Figure 97: 20/40-30/50 Mixed 50 PSIG

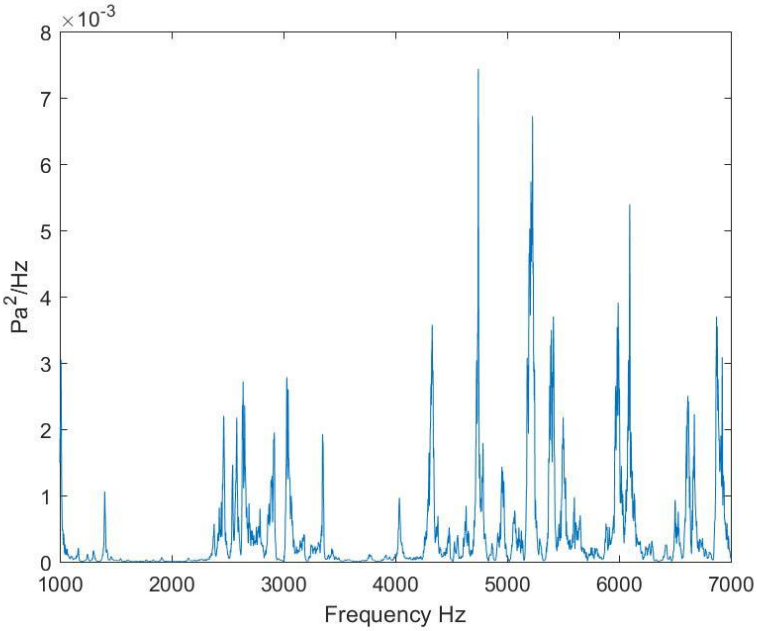

Figure 98: 20/40-30/50 Mixed 60 PSIG

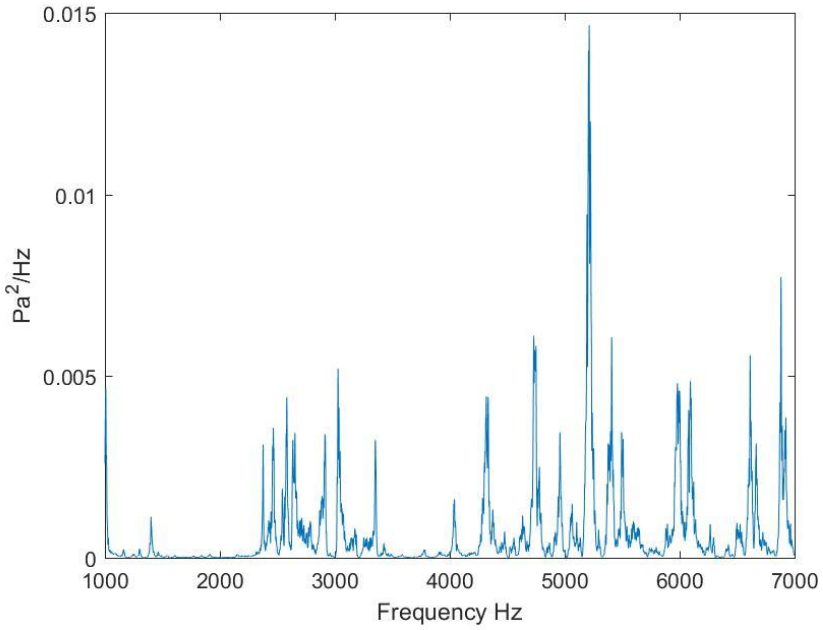

Figure 99: 20/40-30/50 Mixed 70 PSIG

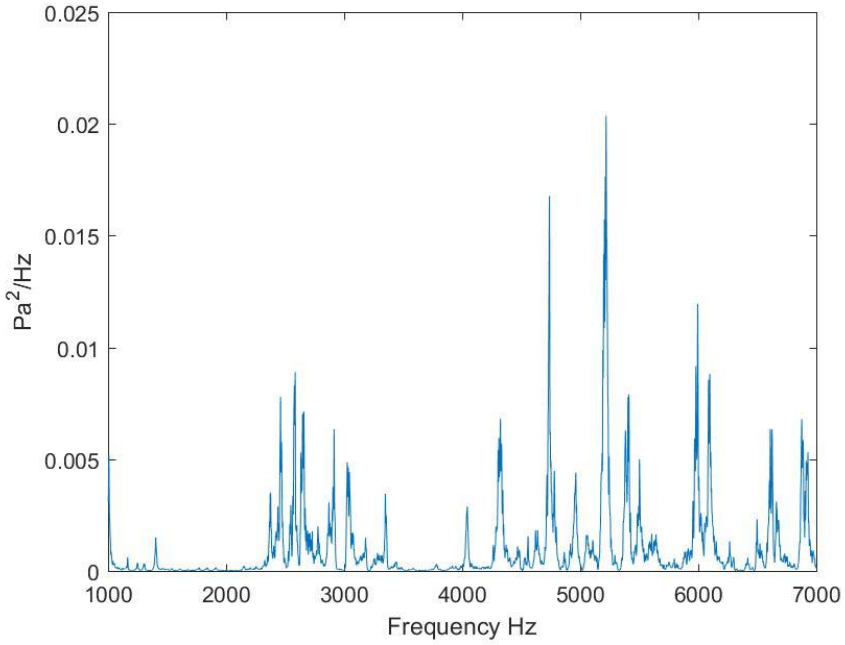

Figure 100: 20/40-30/50 Mixed 80 PSIG

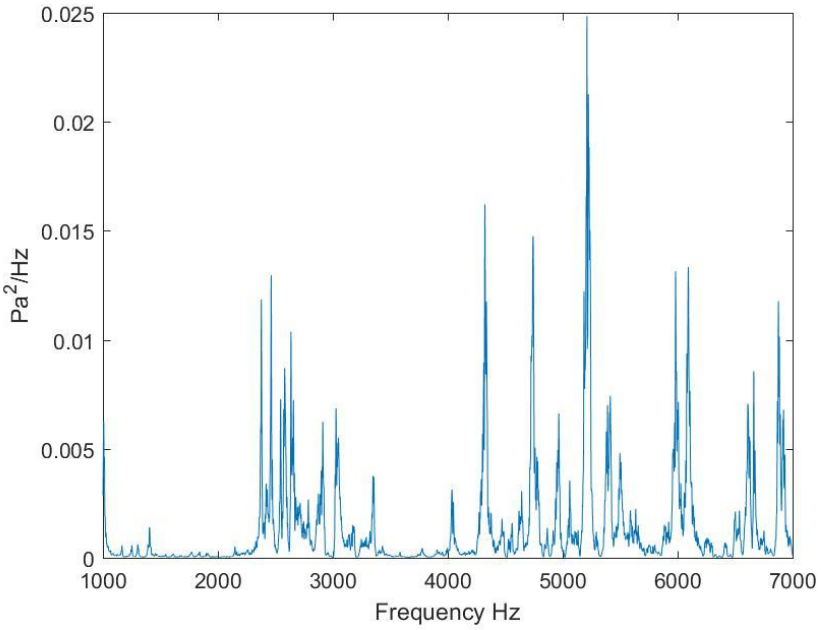

Figure 101: 20/40-30/50 Mixed 90 PSIG

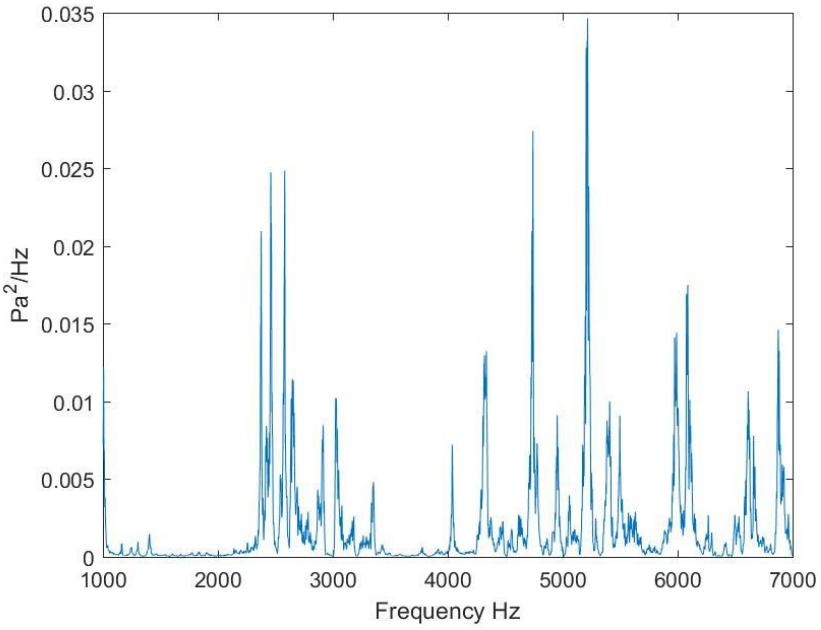

Figure 102: 20/40-30/50 Mixed 100 PSIG

100 Mesh

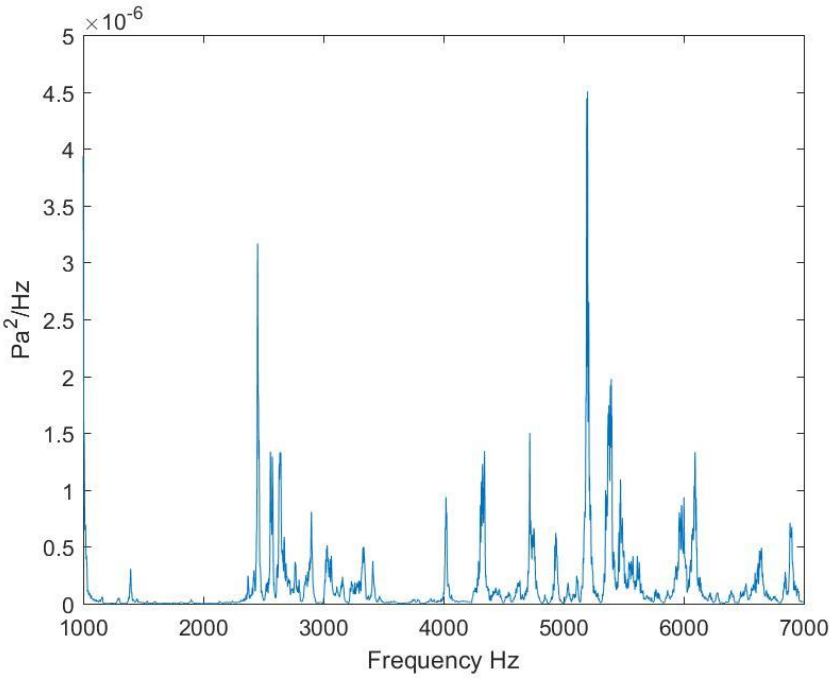

Figure 103: 100 Mesh 10 PSIG

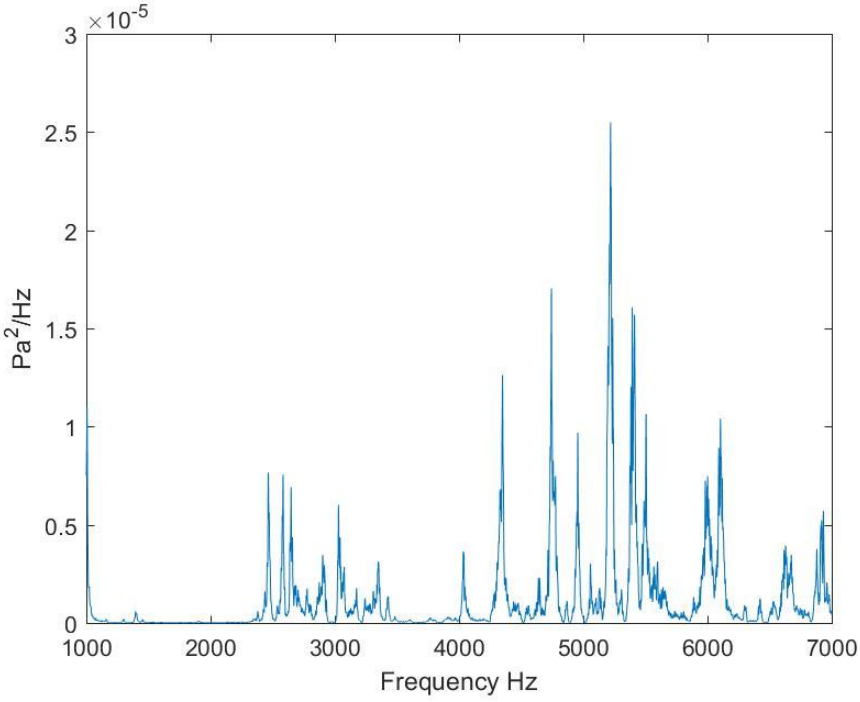

Figure 104: 100 Mesh 20 PSIG

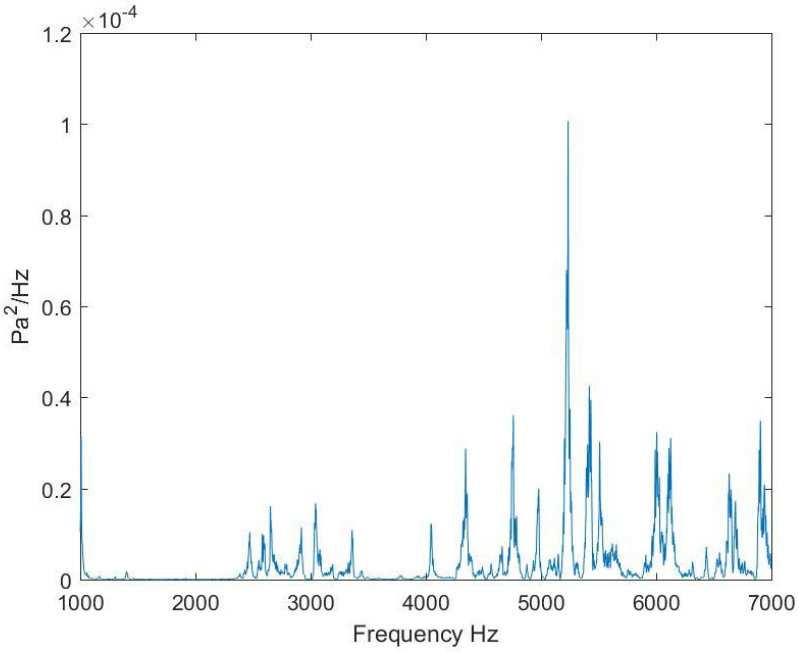

Figure 105: 100 Mesh 30 PSIG

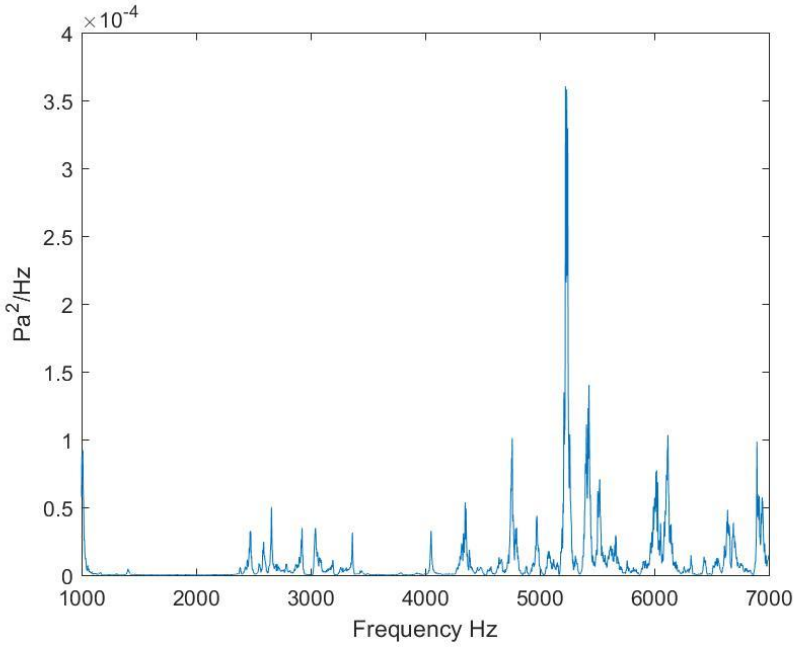

Figure 106: 100 Mesh 40 PSIG

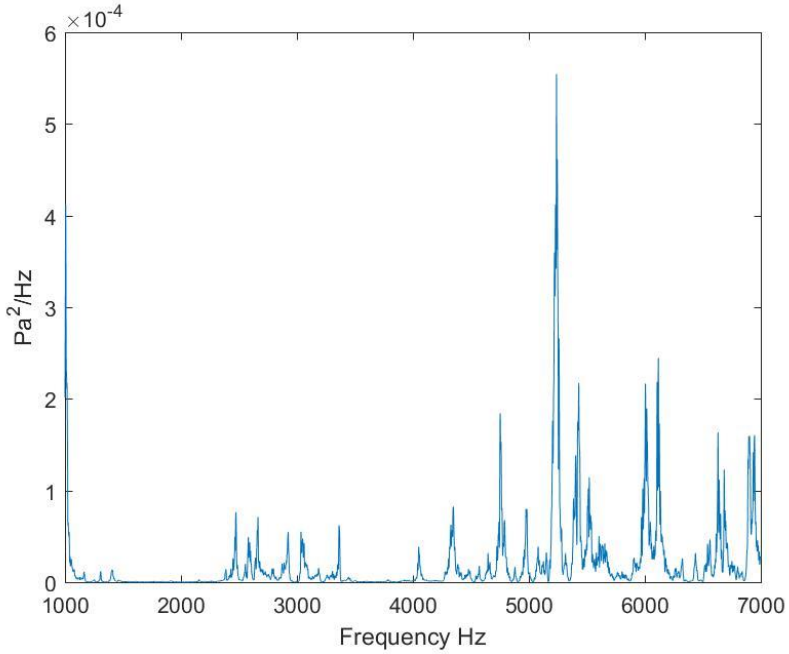

Figure 107: 100 Mesh 50 PSIG

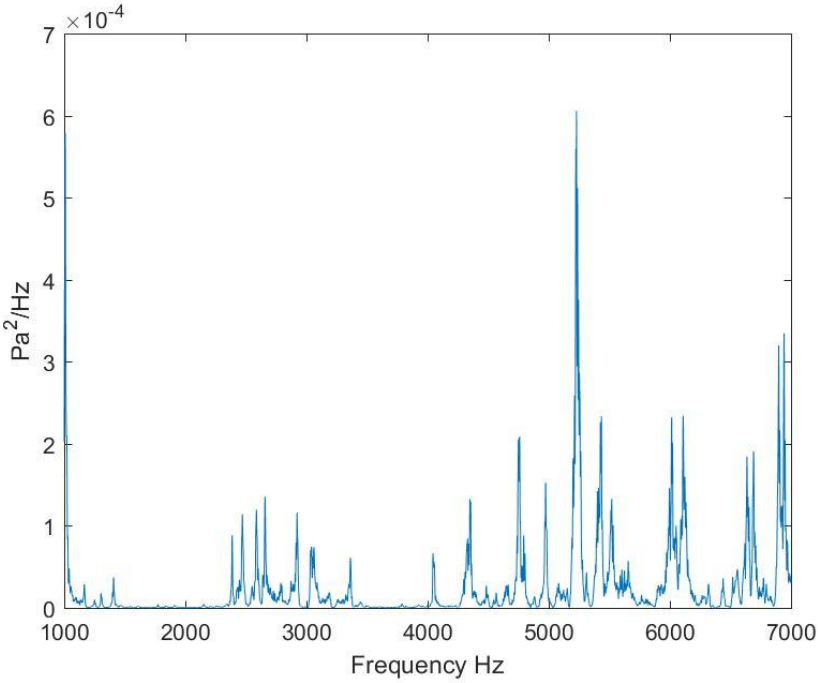

Figure 108: 100 Mesh 60 PSIG

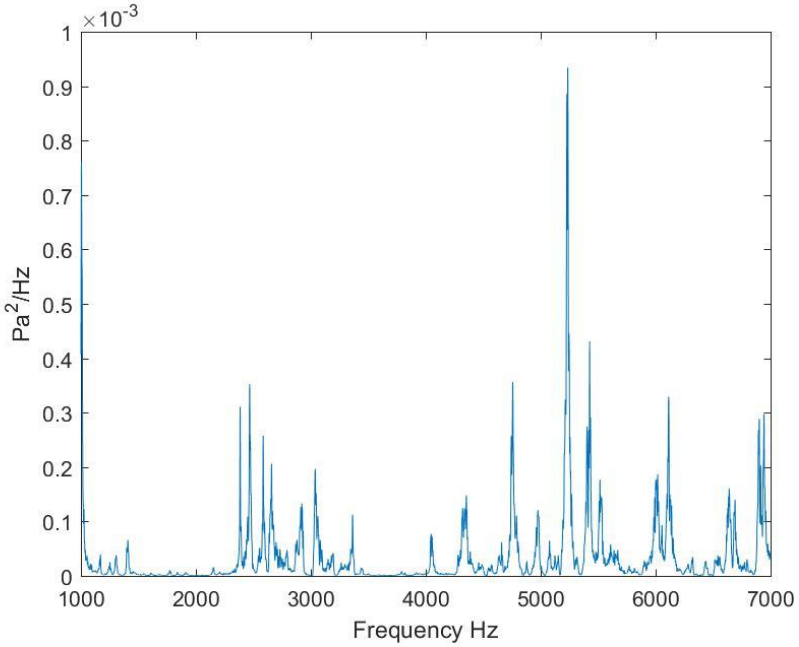

Figure 109: 100 Mesh 70 PSIG

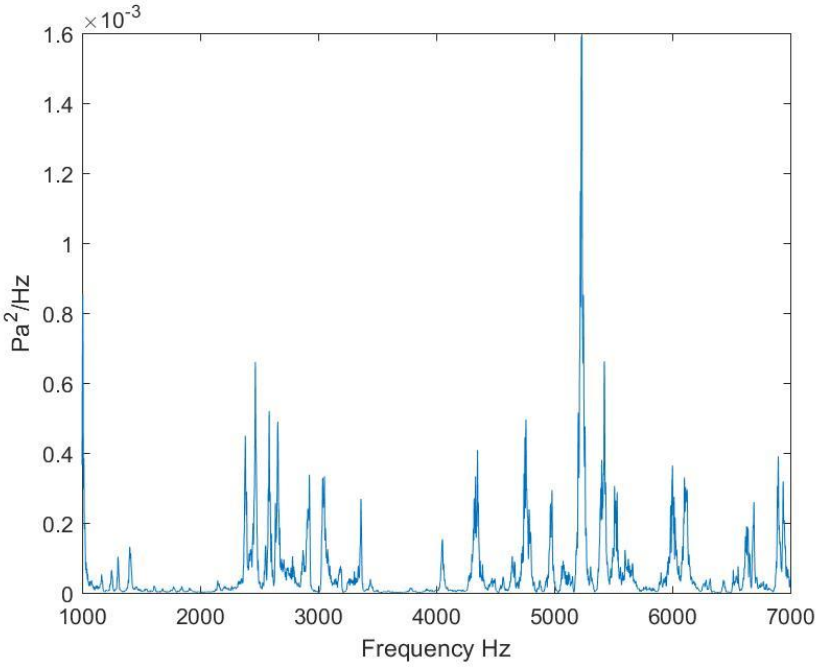

Figure 110: 100 Mesh 80 PSIG

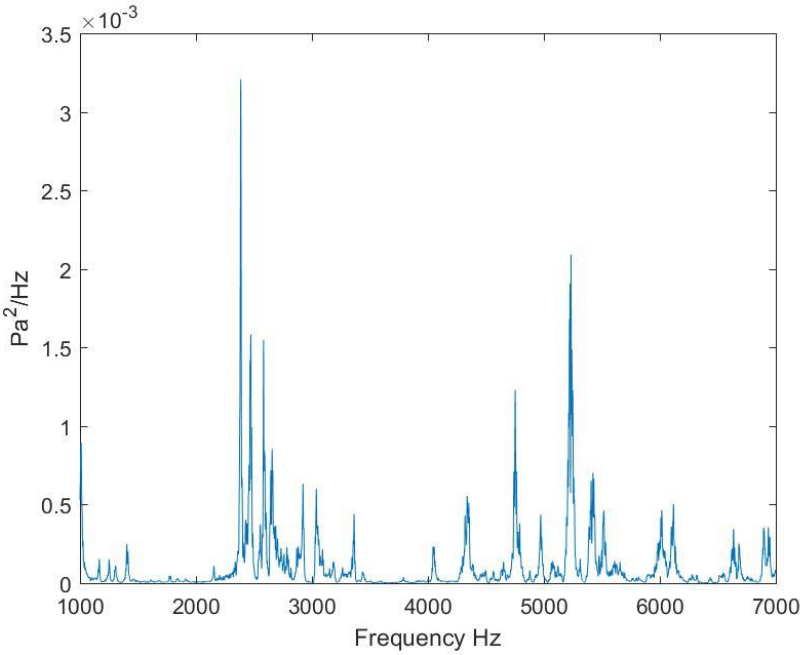

Figure 111: 100 Mesh 90 PSIG

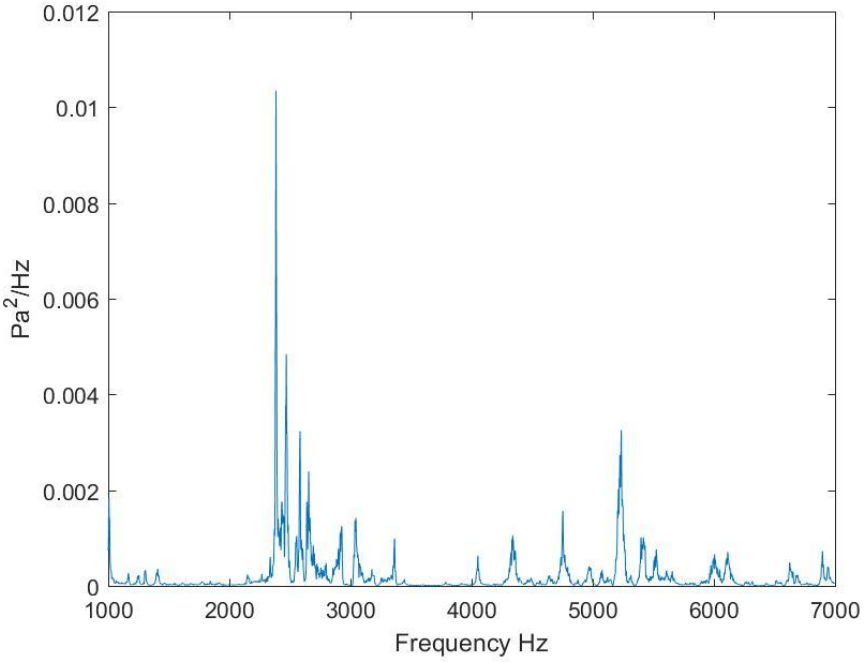

Figure 112: 100 Mesh 100 PSIG

40/70 Mesh

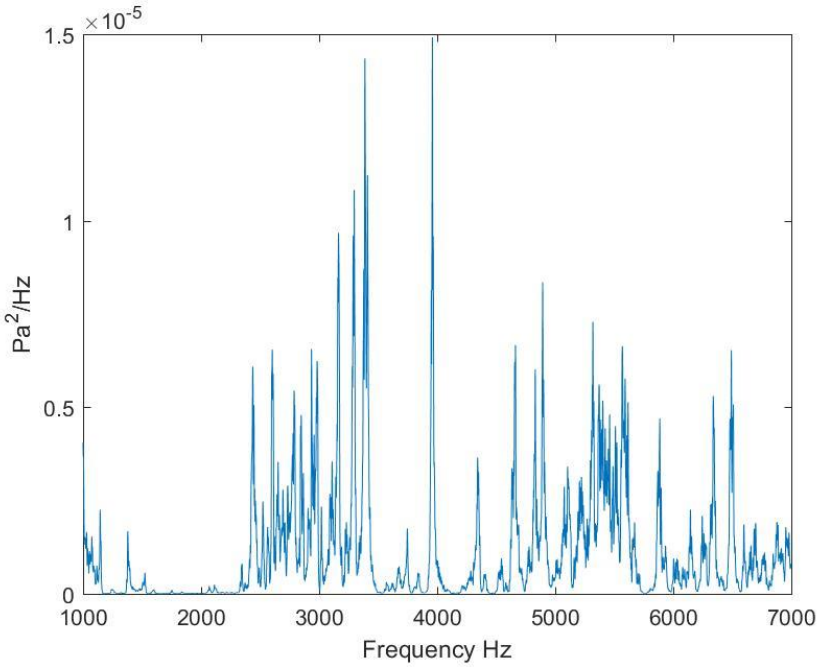

Figure 113: 40/70 Mesh 10 PSIG

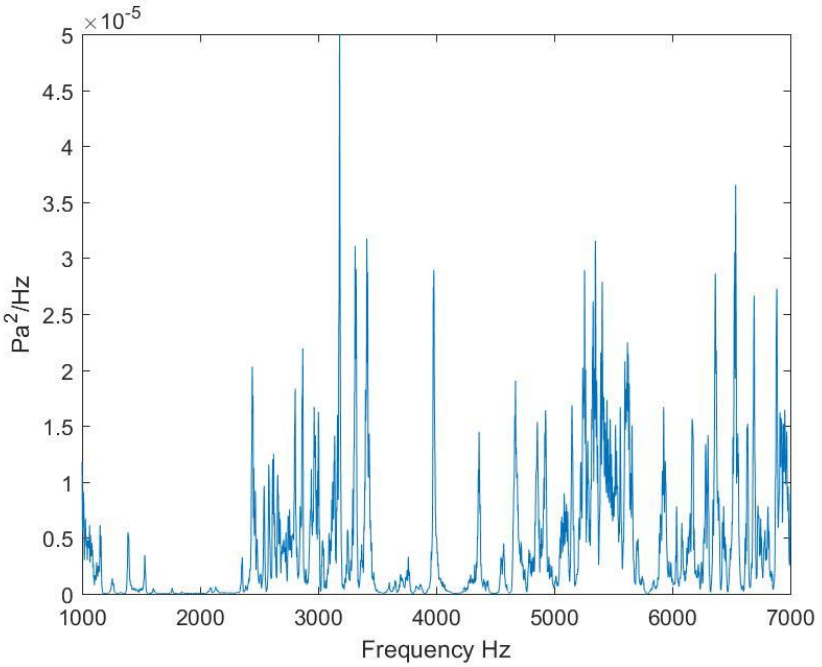

Figure 114: 40/70 Mesh 20 PSIG

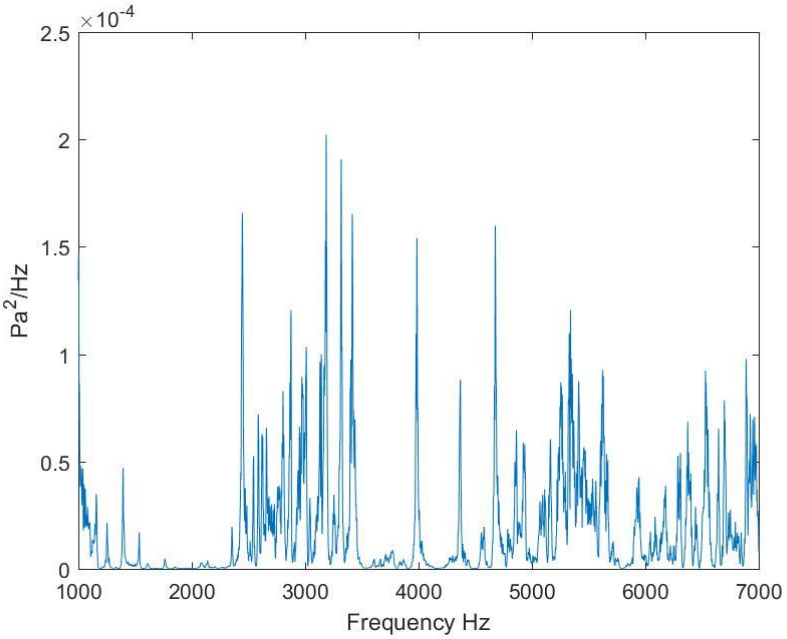

Figure 115: 40/70 Mesh 30 PSIG

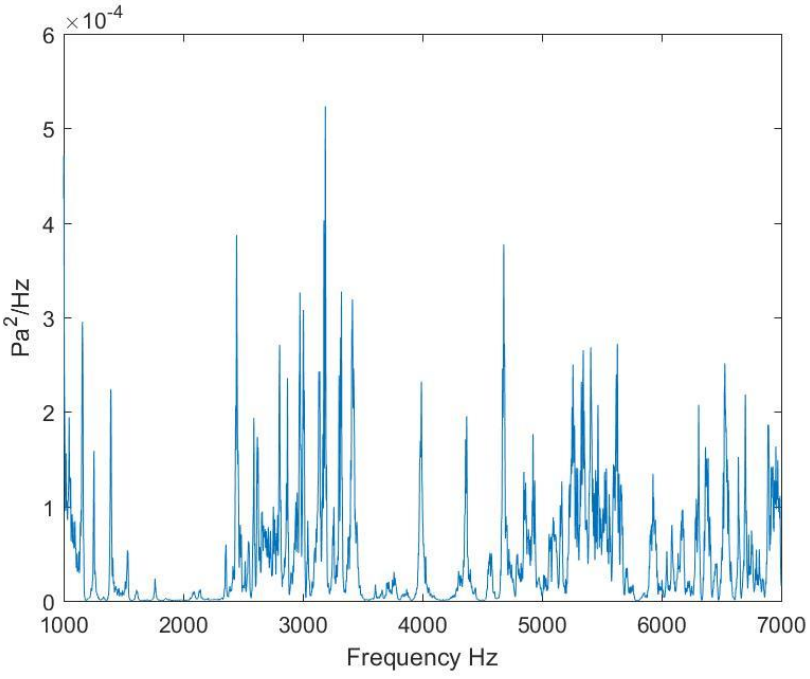

Figure 116: 40/70 Mesh 40 PSIG

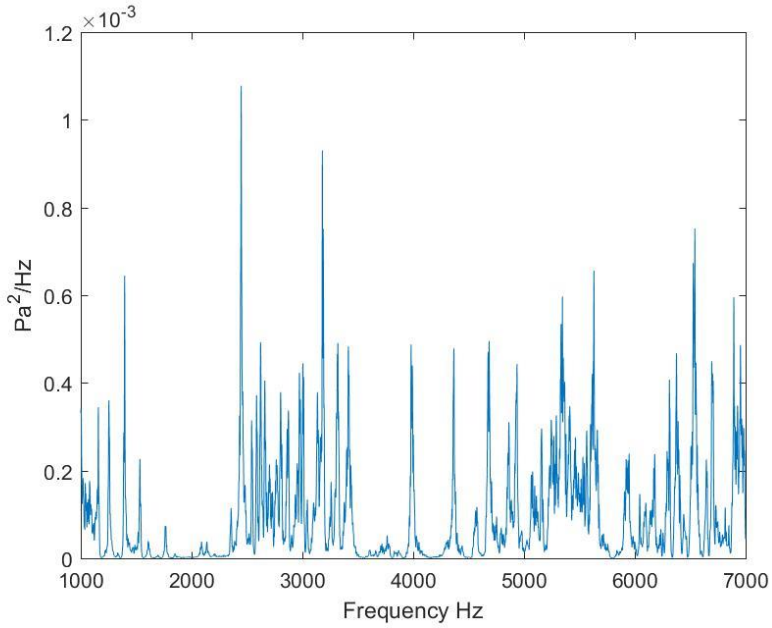

Figure 117: 40/70 Mesh 50 PSIG

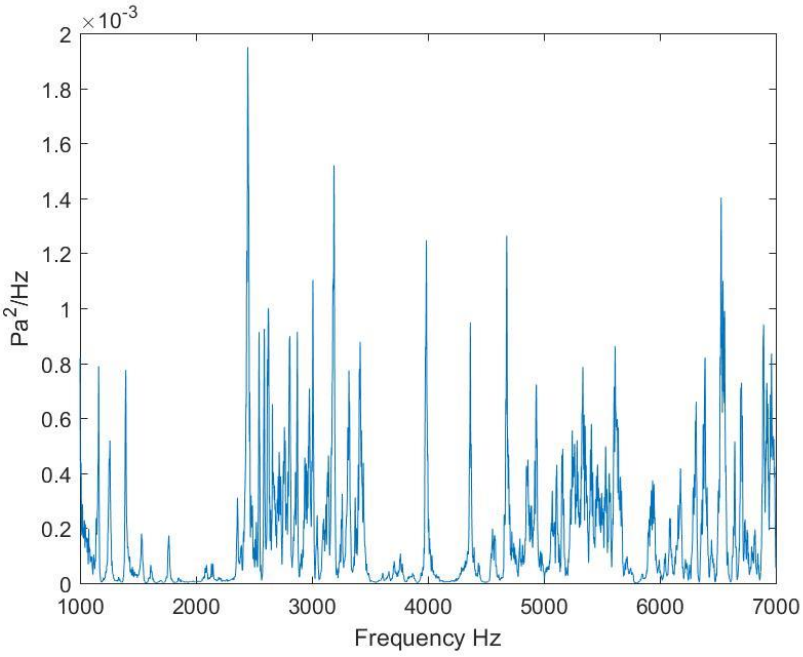

Figure 118: 40/70 Mesh 60 PSIG

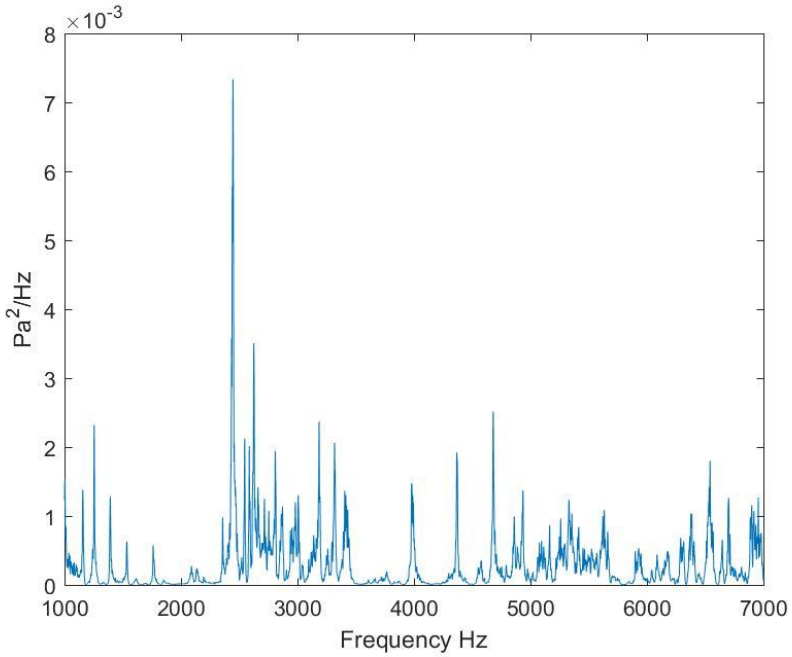

Figure 119: 40/70 Mesh 70 PSIG

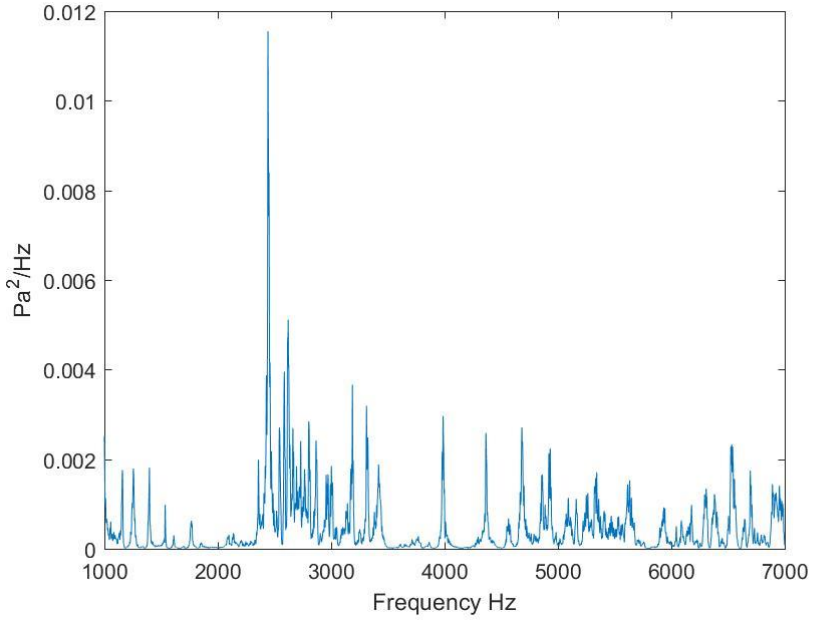

Figure 120: 40/70 Mesh 80 PSIG

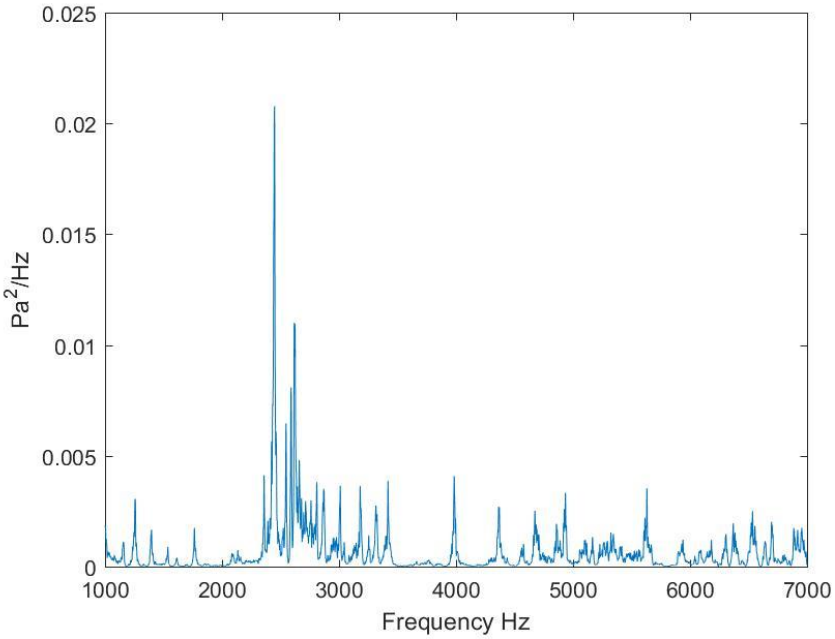

Figure 121: 40/70 Mesh 90 PSIG

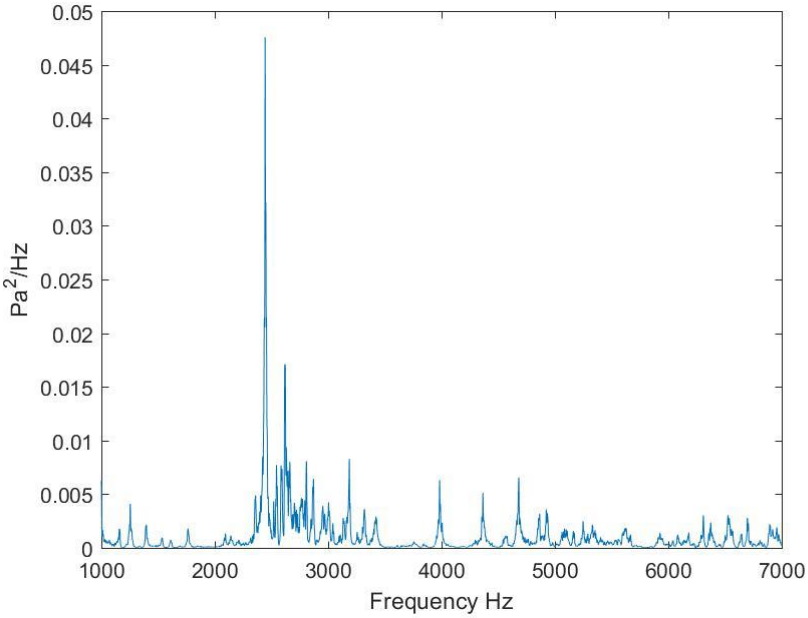

Figure 122: 40/70 Mesh 100 PSIG

APPENDIX C

LABVIEW DATA ACQUISITION APPLICATION BLOCK DIAGRAM

The Block Diagram for the LabVIEW application is provided in this appendix. The application consists of a DAQ assistant block to control the NIDAQ and set parameters for the data acquisition including sampling and bit rate, acquisition length, and calibration. Output of DAQ assistant block is then taken to display an amplitude vs. time plot, and put through a spectral measurements block to display the FFT amplitude and phase for the data. The data is also output to file saving block where a file name is taken from the application front page and channel name, and run information is appended and saved to the target folder pointed to in the front page of the application.

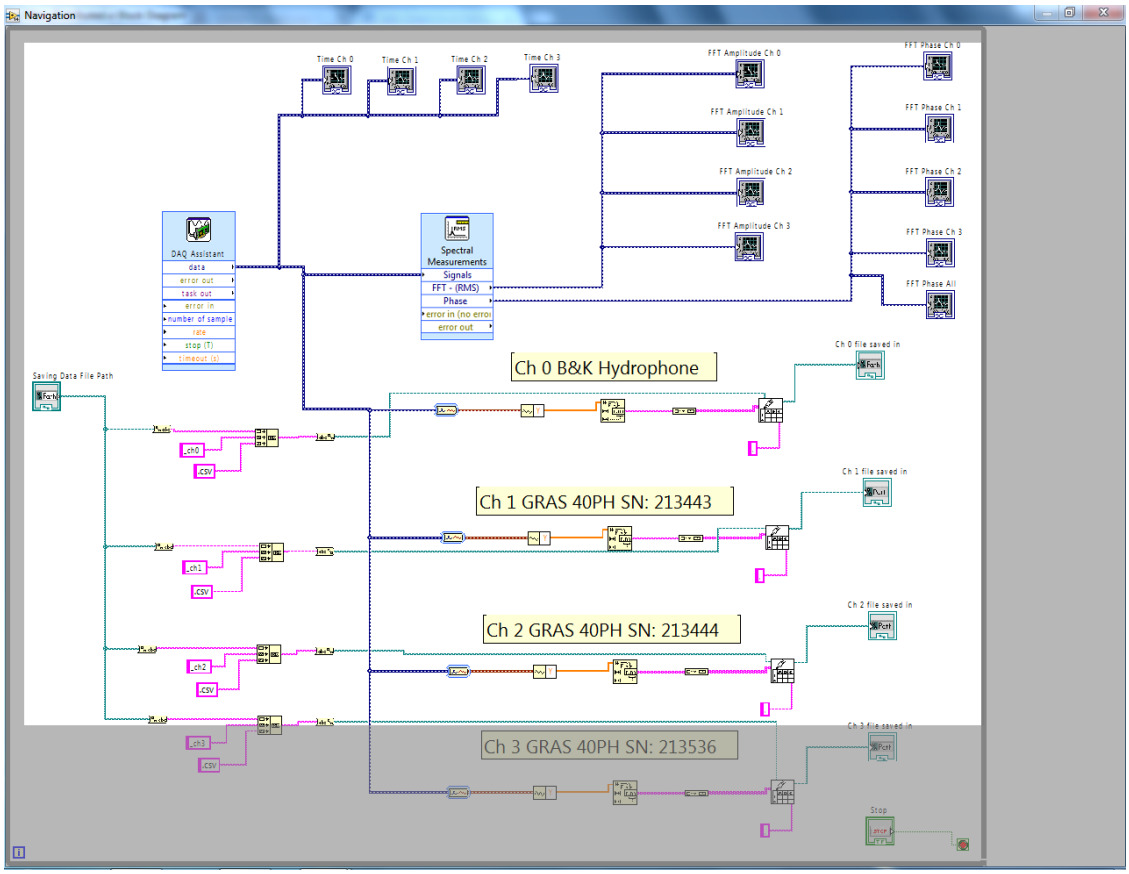

Figure 123: Block Diagram of LabVIEW Data Acquisition Application